

**Investigation of Interfacial Chemistry for High Energy Density
Triboelectric Nano-generators**

by

Priyesh Dhandharia

A thesis submitted in partial fulfillment of the requirements for the degree of

Doctor of Philosophy

in

Materials Engineering

Department of Chemical and Materials Engineering

University of Alberta

© Priyesh Dhandharia, 2017

Abstract

There are several ambient sources, available abundantly and naturally, that can create vibrations such as wind, water current, body movements, vehicles in motion, etc. from which energy can be harvested. There are several types of electrostatic generators proposed to harvest energy from these resources. Of these different generators, triboelectric nano-generators (TENG) have demonstrated outstanding performance in terms of efficiency and power density. Due to the low cost, lightweight and simple designs of these devices, there is a huge potential for them to be commercially viable in the future. The operation of a TENG device can be broadly categorized into two major processes: triboelectric charge generation and the device physics. Although both processes have been studied in great detail, there is still a lack of proper understanding of the triboelectric charge generation process. Therefore, we have taken the opportunity to explore different processes of triboelectric charge generation. The triboelectric charge generation is an interfacial phenomenon which can be influenced by various factors and might give rise to several uncertainties during the device operation. Thus, to understand the triboelectric charge generation process, multiple parameters were studied on PMMA (polymethyl methacrylate) with the help of Taguchi design. This method not only helped in reproducing the results but also quantified the contribution of different parameters to the generated triboelectric charge. Based on this study, it was concluded that the bond breaking during contact creates charges and the interfacial water plays an important role. It was found that dielectric relaxation of the ice-like stern layer is one of the controlling factors during triboelectric charge generation. The role of interfacial water during triboelectric charging was further explored. Using Scanning Probe Microscopy's Tapping mode, it was shown that interfacial water layer increases around the charged region and can alter tip-sample interaction. Apart from the charges, generation of mechano-radicals during the triboelectric process was also

investigated. Since radicals are paramagnetic in nature, with the help of Magnetic Force Microscopy (MFM), it was found that highly stable radicals are generated during the triboelectric charging. It was also noticed that when triboelectric charges combined they also created the radical. These radicals are shown to stabilize triboelectric charges. Therefore, we investigated whether more charges can be generated or stabilized if more radicals are present. It was concluded that instead of radicals, optimizing the molecular design of polymer around the reaction center and introducing nanostructures can drastically increase the energy density of TENG devices. The proposed study can help to fabricate TENG devices whose performance is predictable and is higher in efficiency.

Preface

The literature review, experimental results and analysis, and conclusion are my original work under the supervision of Dr. Thomas Thundat. This thesis has been organized in the paper-based format for easy publication purposes.

Chapter 1 discusses the broader context of the thesis. The literature review, data collection and analysis i.e., FFT of several vibration resources and discussion in the Chapter were done by me. Dr. Faheem Khan helped in selecting and collecting data from several vibrational resources. Dr. Thomas Thundat was involved in the discussion.

In Chapter 2, several parameters associated with triboelectric charge generation were studied. The literature review, design of experiments (DOE), experimental setup and measurements were conducted by me. I have also analyzed all the experimental data. Dr. Ravi Gaikwad trained me on the AFM. Dr. Behnam Khorisidi helped me with the DOE. As mentioned I conducted all the experiments/analysis and discussed my results with Dr. Ravi Gaikwad, Dr. Selvaraj Naicker, Dr. Ankur Goswami, , and Dr. Thomas Thundat.

In Chapter 3, we studied the role of interfacial water during triboelectric charging. Again literature review, experiments, measurement and analysis were done by me. Dr. Ravi Gaikwad Dr. Ankur Goswami, Dr. Selvaraj Naicker and Dr. Thomas Thundat were involved in the discussion.

The TENG setup is discussed in Chapter 4. The literature review, analytical model, experimental setup, measurement and analysis were done by me. The instrument interface, Arduino code and data acquisition and analysis from python were done by me. Dr. Faheem Khan helped in setting up the stepper motor based linear actuator. Dr. Manisha Gupta, Dr. Ankur Goswami, Dr. Selvaraj Naicker and Dr. Thomas Thundat were involved in the discussion of the results and analysis.

In Chapter 5, we discuss the role of radicals during triboelectric generation and explore the possibility to use them for higher triboelectric charge density generation. MFM, KPFM experiments, measurement, model and analysis was done by me. For the next part, I selected and synthesized the radical polymer (PTMA). Dr. Selvaraj Naicker provided technical assistance during the synthesis of polymer. EPR studies were performed by Mr. Mohammad Saifur, a student of Dr. Arno Siraki, from the Faculty of Pharmacy and Pharmaceutical Sciences at University of Alberta. Cyclic Voltammetry experiments were done by Dr. Zhi Li. DFT calculations were done

by Dr. Javix Thomas. GPC experiments were conducted by Dr. Yangjun Chen from Department of Chemical and Materials Engineering. TENG and all other characterizations together with the literature review and analysis was done by me. Dr. Manisha Gupta, Dr. Selvaraj Naicker, Dr. Ravi Gaikwad, Dr. Ankur Goswami, and Dr. Thomas Thundat were also involved in the discussion.

Acknowledgment

I would like to express my sincere gratitude to Dr. Thomas Thundat for his valuable guidance and support given to me during the project. I am thankful to him for the discussions, which helped me greatly in this project as I gained more insight into technical details.

I would like to acknowledge the Canada Excellence Research Chairs (CERC) Program and the Department of Chemical and Materials Engineering at the University of Alberta for giving me the opportunity to do research and for the financial support during my program. I would like to acknowledge nanoFAB and its staff, especially Dr. Peng Li, Dr. Shihong, Dr. Anqiang, Dr. Dimitry and OSCIEF, especially Dr. Ni Yang for their excellent input on several characterization techniques and analyses. I am grateful to all the Chemical and Materials Engineering Department office staff, machine shop staff, and IT personnel for their generous help at different stages of the research project. Also, the technical assistance from Keithley, Bruker is appreciated.

I would like to express my gratitude to Dr. Ravi Gaikwad, Dr. Selvaraj Naicker, Dr. Faheem Khan, Mr. Behnam Khorsidi, Dr. Ankur Goswami, Dr. Zhi Li, Dr. Prashanthi Kovur, Dr. Zeljcka Antic and Dr. Charles Van Neste for giving me their valuable time and constant input on various technical details.

I would like to express my sincere gratitude to my supervisory committee, Dr. Manisha Gupta and Dr. Weixing Chen, for their valuable input on the thesis and their support during tough times.

I acknowledge Dr. Arno Siraki and Dr. Saifur Rahman Khan for the EPR experiment and fruitful discussion.

I would like to thank Dr. Vinay Prasad for his support and guidance. I would also like to thank Dr. Dan Sameoto and Dr. Rambabu Karumudi for their extremely insightful guidance.

I would also like to thank Lily Laser and Josie Nebo for their ever-ready-to-help attitude and great support.

I am thankful to the members of NIME group, especially Dr. Tinu Abraham, Dr. Naresh Miriyala, Dr. Arindam Phani, Mr. Syed Asad Bukhari, Mr. Ryan McGee, and Mr. John Hawk for their constant support. I would also like to thank all other members of NIME group for their help and

support. I am also thankful to all my friends who were always there for me and cheered me up whenever I was not feeling well.

I would like to thank several Youtubers such as Khan Academy, sentdex, toptechboy, the contributors to StackOverflow, edx, nanohub for providing excellent technical materials that helped me a lot in my project.

Last but not least, I would also like to express my sincere thanks to my parents, sisters and family members for their unflagging support. Without their support, this work would not have been possible.

Table of Contents

Abstract	ii
Preface.....	iv
Acknowledgment	vi
Table of Contents	viii
List of Figures	xi
List of Tables	xv
1 Introduction.....	1
1.1 International Energy Policies and Future of Energy	1
1.2 Sources of ambient energy	1
1.3 Ambient Vibrational Energy Distribution.....	2
1.4 Mechanisms for Harvesting Ambient Vibrational Energy:.....	3
1.5 Triboelectric Nano-generators.....	6
1.6 Triboelectric Effect	7
1.7 Objective of the Thesis.....	8
1.8 Outline of the thesis:	8
2 Nano-scale study of triboelectric charge generation mechanism	10
2.1 Introduction	10
2.2 Taguchi Design and Selection of Factors:.....	13
2.2.1 Analysis of Variance (ANOVA Analysis):.....	15
2.3 Experimental Method:.....	18
2.4 Results and Discussion:.....	21
2.4.1 Effect of tips:.....	24
2.4.2 Effect of Bias:	27

2.4.3	Effect of Force:	30
2.4.4	Effect of number of contacts:.....	31
2.4.5	Effect of Relative Humidity (RH):	32
2.4.6	Effect of tapping frequency:	34
2.4.7	Effect of Tip Material:	39
2.5	Conclusion:.....	41
3	Role of Interfacial Water during Triboelectric Charging	44
3.1	Introduction	44
3.2	Experimental Detail.....	46
3.3	EFM study of Triboelectric charges.....	47
3.3.1	Theory.....	47
3.3.2	EFM Results and Discussions.....	49
3.4	Phase Imaging Study of Interfacial Water	52
3.4.1	Theory of Tapping Mode Imaging and Evolution of Phase	52
3.4.2	Phase Imaging Studies	55
3.4.3	Checking for Artifacts.....	57
3.4.4	Amplitude Phase Displacement analysis	58
3.5	Conclusion.....	63
4	Physics of Contact Mode Triboelectric Nano-generator	64
4.1	Introduction	64
4.1.1	Equivalent Circuit of a TENG device.....	65
4.1.2	Role of Parasitic Capacitance	68
4.1.3	Minimum Achievable Charge Reference State (MACRS).....	72
4.1.4	Performance Figure of Merits (FOMP).....	75
4.2	Conclusion.....	76

4.3	Experimental Setup	77
5	Radicals and Triboelectric Nano-generators.....	78
5.1	Introduction	78
5.2	Experimental details.....	81
5.2.1	MFM study of Mechano-radical:	81
5.2.2	Radical Polymer Synthesis	81
5.2.3	Characterization of Radical Polymer	83
5.3	Mechano-radicals and triboelectric charges.....	84
5.4	Radical Polymer and TENG characterization	90
5.4.1	Characterization of Radical Polymer	90
5.4.2	TENG Study.....	91
5.5	Conclusion.....	98
6	Summary and Future Work.....	99
6.1	Summary:	99
6.2	Future Work:	100
	Reference	103
	Appendix A.....	113
	Appendix B.....	115
	Appendix C.....	116

List of Figures

Fig. 1-1: Types of ambient energy and their power density ⁴	2
Fig. 1-2: Distribution of vibrational energy spectrum with different sources. Acceleration Spectral Density from (a) human walk, (b) car, (c) a bridge, (d) a tree.....	3
Fig. 2-1: An illustration of a factorial design for 3 factors at 2 levels and the selection of a set of experiments for Taguchi design. The four points in the cube show selection of experimental set for Taguchi design. The axis on the right shows the direction along which the level of each factor has been varied.	14
Fig. 2-2: Predictions from Taguchi Design for (a) bias, (b) applied force, (c) number of scans and (d) tapping frequency. The prediction for all three relative humidity level has been plotted.....	22
Fig.2-3: The above graphs show the confirmation experiment done to verify the predicted trend from Taguchi Analysis for (a) bias, (b) applied force, (c) number of scans and (d) tapping frequency. The results for all three different relative humidity levels have been plotted. For confirmation tests, the parameters for different experiments were chosen at random. The condition for each confirmation test is given with their respective plots.	24
Fig. 2-4: Adhesion force between Si tip and PMMA substrate (a) for Tip 1 at different RH, (b) at RH 80% for different tips and (c) the axial stress, contact radius, and tip radius of the three tips calculated for the applied force of 40 nN.....	28
Fig. 2-5: SEM images of (a) Unused Si cantilever, (b) Tip 1, (c) Tip 2.....	29
Fig. 2-6: Comparison of (a) the generated triboelectric charge density vs the potential contact difference between the tip and uncharged PMMA. The above values were obtained at a tapping frequency of 0.25 kHz, applied force of 40 nN; the number of scans was 15 and the bias applied was 0V. (b) Triboelectric charge density for different tip bias at RH 80% from Tip 2. These results were obtained by applying a force of 40 nN, 1 kHz tapping frequency and 10 scans.....	30
Fig. 2-7: Effect of (a) force, (b) axial stress, (c) deformation, (d) calculated energy dissipation on triboelectric charge density generated with both Tip 1 and 2. The triboelectric charge was generated by applying 0V bias, 15 scans, RH 80% and tapping frequency of 0.25 kHz. (e) Comparison of calculated energy dissipation and experimentally obtained energy dissipation for Tip 2.....	33

Fig. 2-8: Comparison of (a) F-Z approach, (b) retract curve for Tip 1 at different relative humidity. (c) Amount of surface charge generated as a function of relative humidity and (d) energy dissipation as a function of RH, calculated from the applied force of 7 nN..... 36

Fig. 2-9: Variation of contact time with different tapping frequency (a) 0.25 kHz, (b) 0.5 kHz, (c) 1 kHz, and (d) 2 kHz..... 37

Fig. 2-10: Comparison of the triboelectric surface charge density at different contact times (a) at different relative humidity and tips, (b) for different applied bias at RH 50%. (c) Comparison of the energy dissipated at each contact for different tapping frequency, (d) Simulated Debye relaxation of ice. The parameters for the simulations were obtained from von Hippel⁸⁴ and reconsidered by Artemov et al⁸³. 38

Fig. 2-11: (a) EFM study of triboelectric charge generated from the Pt-coated tip, applied force, in this case, was 1nN and cantilever resonance frequency was 147 kHz, (b) KPFM study done with Pt-coated tip, the resonance frequency of cantilever was 70 kHz. Both readings were taken at RH 13-20%. SEM images of (c) unused Pt-coated AFM tip and (d) AFM tip after imaging. 40

Fig. 3-1: (a) Frequency shift observed during the EFM study of the charged region at RH 80%, the dark brown region is the location where charges were generated (b). The histogram of the Frequency shift observed during EFM for (a) and Gaussian Fitting done for charged and uncharged region, (c) Frequency shift observed for the charged and uncharged region at different relative humidity wrt. to the potential difference between the tip and substrate. (d) The difference in the linear component of the charged and the uncharged region determined from the curve fitting and (e) The quadratic coefficient for different relative humidity at charged and uncharged region. .. 51

Fig. 3-2: (a)-(c) Topography of the area where charges were generated for different relative humidity, (d)-(f) Respective surface potential of the same area for the given RH's, (g)-(i) phase shift observed during tapping mode at an drive amplitude of 22 nm and amplitude setpoint of 14 nm, (j)-(l) phase shift observed during tapping mode imaging for drive amplitude of 110 nm and amplitude setpoint of 60 nm. 56

Fig. 3-3: Artifact which can be observed during tapping mode imaging. (a), (b) is the tapping mode image with a tip bias of -10 V, (c),(d) for 0V and (e), (f) for 10V. The artifact in the topography can be easily identified, whereas in the phase the shift between charged and uncharged region is not significant..... 58

Fig. 3-4: (a) Amplitude and (b) phase of the cantilever oscillation at 200 nm from the surface. (c), (e) is the amplitude vs z plot for the approach and the retract of the cantilever to the surface, (d), (f) is the phase shift of the cantilever as the cantilever approaches or retract from the surface. .. 60

Fig. 3-5: (a) The topography image captured during the charge generation, (b) a cross-section profile and x and y direction, (c) change in the surface potential before and after tapping mode imaging. 62

Fig. 4-1: (a) The schematic of a contact mode TENG device operation, (b) The electrical elements associated with (a), (c) Equivalent Circuit for a TENG device, (d) a TENG device with CP , (e) Equivalent circuit for a TENG device with CP 65

Fig. 4-2: (a) Charge and Capacitance, (b) Open circuit voltage of a TENG device as a function of displacement, (c) time-varying current and (d) voltage of a TENG device. (e) Charge and Voltage as a function of displacement..... 71

Fig. 4-3: (a) VOC as a function of different reference plane (x) and CP , (b) Computed and experimental VOC for $CP = 300 pF$ but different x_{max} . Experimental (c) Charge, (d) VOC as a function of different x . (e) Voltage as a function of CP for $x = 0$ and x_{max} and (f) energy density as a function of displacement for different CP 74

Fig. 5-1: Triboelectric study done on PMMA, (a) the topography of the region after the charges have been generated, AM-KPFM results (b) after generating charges and (c) after 29 days of charge generation. The MFM results of the charged area (d) without magnetic field and (e) with a magnetic field after generating charges. Both AM-KPFM and MFM images were captured at a lift height of 100 nm. 87

Fig. 5-2: (a) MFM signal as a function of different lift height in presence and absence of an external magnetic field, (b) Evolution of surface potential and MFM signal as a function of time. MFM results were taken in presence of magnetic field. 88

Fig. 5-3: Characterization of radical polymer (a) FTIR spectra of PTMA and PTMPM polymer, (b) Cyclic Voltammetry of radical polymer, (c) EPR spectra of TEMPOL, (D) EPR spectra of radical polymer, PTMA 91

Fig. 5-4: TENG characterization of PTMA, (a) Voltage, (b) current as a function of time for water and ethanol cleaned sample. The compiled result of (c) VOC , and (d) σ_{SC} for PTMA, PTMPM and PMMA for different cleaning procedure..... 93

Fig. 5-5: XPS spectra of N1s for (a) PTMA, (b) PTMPM cleaned with water. (c) PTMA, (d) PTMPM cleaned with ethanol. The peak fitting for different chemical bonds and the fitted results are given in the legend. 94

Fig. 5-6: CV of PTMA and PTMPM cleaned with water and ethanol. The blue color indicates the result obtained by water cleaning and orange color for ethanol cleaned samples. 95

Fig. 5-7: Topography of PTMA after cleaning with (a) water and (b) ethanol. Similarly, the topography of PTMPM after cleaning with (c) water and (d) ethanol. 96

Fig. 5-8: Electrostatic potential map of (a) TMPM and (c) TMA determined from DFT calculation. 97

Fig. 6-1: Vibrational Stark Spectroscopy (VSS) of Kapton film. The controlled experiment was done without creating charges in two different ways. In the 1st case, FTIR spectra of the uncharged film were taken at an interval of 15 mins. A very small change in Absorbance values was observed. In the 2nd case, FTIR spectra were collected before and after N₂ drying. Again, very small changes were observed in absorbance value. When the charges were deposited on Kapton by rubbing with Al and Teflon film, more change in absorbance was noticed. Also from single electrode TENG study (result not shown), it was found that Al produced fewer charges compared to Teflon. Therefore, the higher shift in absorbance of Kapton film after rubbing with Teflon suggest that space charge region can be probed by FTIR spectroscopy..... 102

List of Tables

Table 1-1: Mechanisms to convert vibrational energy into electrical energy ^{4,5}	4
Table 2-1: Parameters used during Peak Force Tapping Mode to create the surface charges.....	19
Table 2-2: Parameters used during AM-KPFM and EFM scanning.....	20
Table 2-3: Control factors and their levels for the study from uncoated Si tip.	21
Table 2-4: An example of an L9 set of Taguchi Design used in this study.....	23
Table 2-5: F-Ratio and contribution of each factor.	23
Table 2-6: Mechanical properties of PMMA and Si.....	27
Table 2-7: T-test to compare the significance level of surface potential generated at tapping frequency of 0.5 kHz and 1 kHz with 0.25 kHz.	37
Table 2-8: Control factors and their levels for Taguchi Design using a Pt-coated tip.....	41
Table 2-9: ANOVA analysis of the generated triboelectric charge using a Pt-coated tip.	41
Table 2-10: Scheme for a triboelectric charge generation process ^{9,10,34-36,53}	42
Table 3-1: Parameters used for generating triboelectric charges to study the role of interfacial water:.....	47
Table 4-1: Parameters used for the model.	70

1 Introduction

1.1 International Energy Policies and Future of Energy

With the signing of the Paris Climate Agreement, all the countries in the world have for the first time agreed to keep the temperature rise of the Earth below 2°C. To achieve this target, the amount of greenhouse gas (GHG) emission in the environment needs to be decreased. Hence, our present carbon-based technology energy policy needs to shift significantly to renewable energy¹. The International energy agency (IEA) has estimated that in order to keep the temperature rise of the Earth below 2°C, renewable energy production has to increase from 5% in 2013 to 44% by 2050. In the meantime, the demand for electricity will also increase as many other sectors will see technological advancements. One of the areas which are expected to witness a significant rise is IoT (Internet of Things)². The powering of IoT devices and sensor networks with conventional means such as batteries is not a viable solution as the numbers IoT devices are estimated to go up in billions³. Therefore, it is of utmost importance to develop reliable sources of renewable energy. The renewable energy needs to be harvested from the ambient condition. Therefore, it is important to understand different types of ambient energy sources available.

1.2 Sources of ambient energy

There is a growing demand for efficient, cheap, reliable and robust renewable energy. The type of energy available for harvesting will vary according to the ambient condition. Fig. 1-1 shows power density of various renewable energy forms categorized according to their sources⁴. Among the listed energy resources, solar, wind and thermal energy have already been well established and are being used in the market¹. Wind energy can be accounted for in the category of vibrational energy sources. In addition to wind, there are several other sources of vibration energy such as swaying of the tree branches due to air breeze, wave energy stored in river and oceans, vibration in bridges due to moving vehicles, human motion, etc., which exist in abundance. Some of these resources will be discussed in the next section. Renewable energy can be either harvested from these resources or can be used for other purposes such as IoT (for instance, monitoring the environment, health, etc.)⁴. Although power density from the Sun at the Earth's surface and vibration from ambient environment (Fig. 1-1) have a similar magnitude, relatively less attention has been paid

to exploring ways of harvesting vibration energy from those resources. Due to the diversity of the available resources, different methodology applies to harvesting energy from these resources. This has motivated us to look at different ways of harvesting vibrational energy.

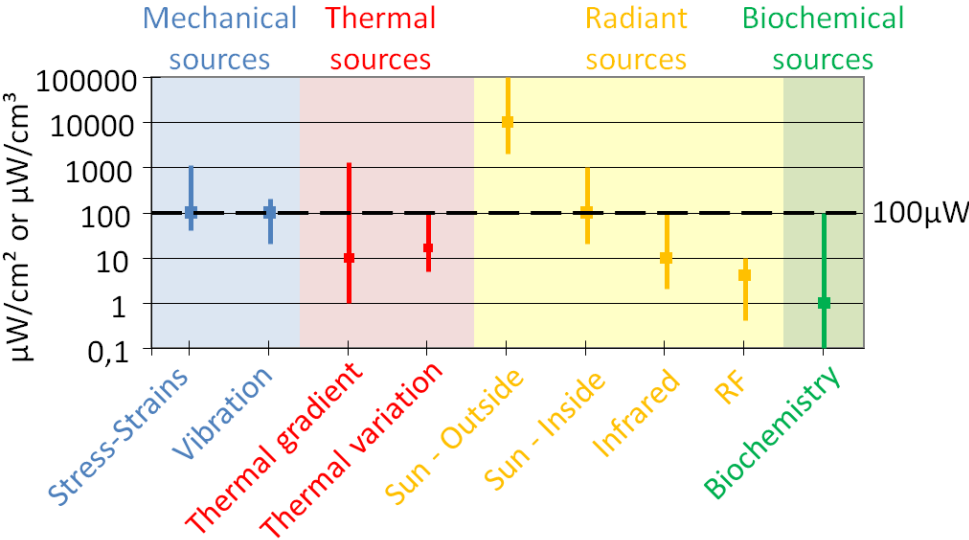


Fig. 1-1: Types of ambient energy and their power density⁴

1.3 Ambient Vibrational Energy Distribution

Harvesting energy from the ambient vibration sources requires understanding the type of sources and appropriate devices that will efficiently utilize the sources. In general, ambient vibration energy can range from broadband to low frequency and low amplitude sources. The broadband sources are the sources where available energies are distributed over a wide frequency range. To get a better insight into the distribution of this energy, the Acceleration Spectral Density (ASD) from a few sources (human walk, the swaying of a tree branch, bridge, and a car) are shown in Fig. 1-2. In Fig. 1-2, only a major component of vibration has been shown. Detailed descriptions of these ASDs are given in Appendix A. From Fig. 1-2, it is clear that different sources will have completely different energy distribution. For instance, the swaying of a tree branch can be categorized as low frequency, low amplitude, while a bridge vibration has slightly higher frequency but again low amplitude. Similarly, vibration in front of a car windshield can be categorized as broadband, and a human walk, as low frequency but high amplitude sources. Thus, harvesting energy from these different sources might require completely different strategies.

However, the basic principles for harvesting this type of energy can be similar. Hence, we looked at different principles of the ways this vibrational energy can be harvested.

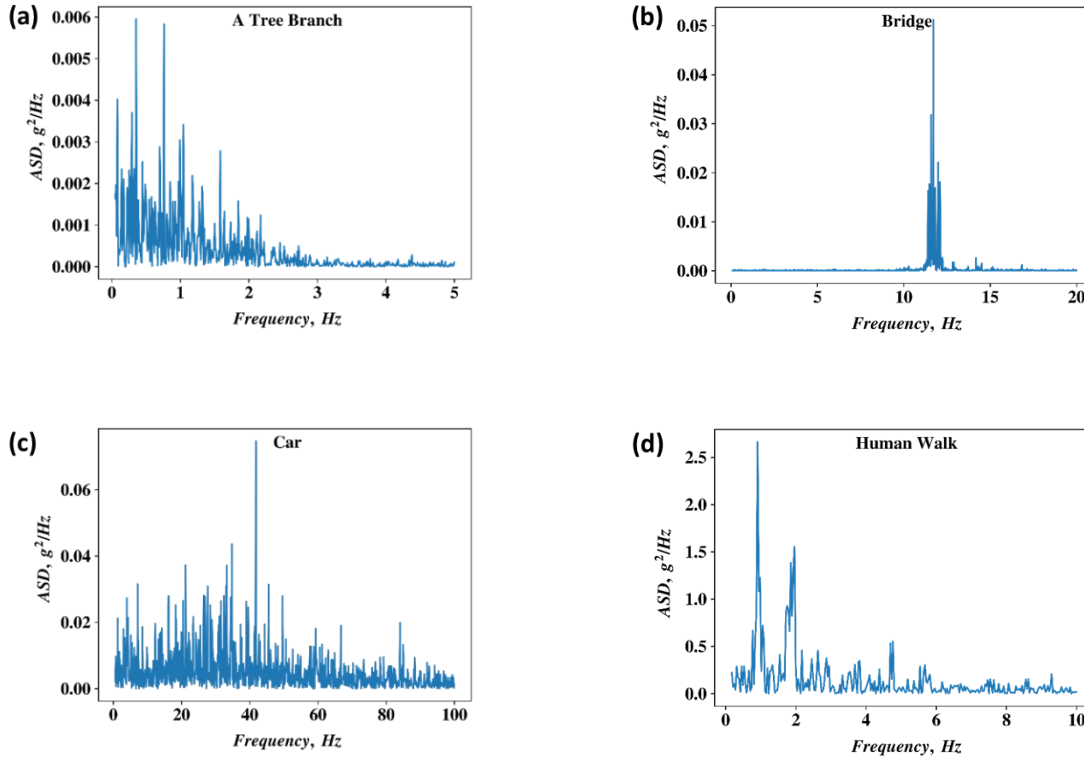


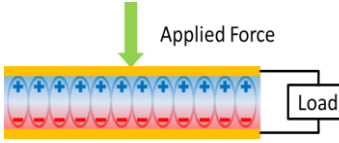
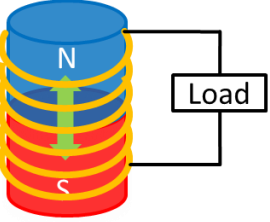
Fig. 1-2: Distribution of vibrational energy spectrum with different sources. Acceleration Spectral Density from (a) human walk, (b) car, (c) a bridge, (d) a tree.

1.4 Mechanisms for Harvesting Ambient Vibrational Energy:

There are three basic ways in which vibrational energy can be converted into electrical energy. A comparison between these three different ways is given in Table 1-1^{4,5}.

Piezoelectric generators are based on the special class of materials that under mechanical deformation induces an electric field. One of the key advantages of a piezoelectric generator is that it doesn't have any moving parts. Since the capacitance of these generators is very high, the output is also high. One of the key problems with piezoelectric generators, apart from those listed in Table 1-1, is that their performance degrades over time. Also, synthesis of piezoelectric materials could be very expensive^{4,5}.

Table 1-1: Mechanisms to convert vibrational energy into electrical energy^{4,5}

	Piezoelectric	Electrostatic	Electromagnetic
			
Working Principle	Piezoelectric Effect and electrostatic induction	Electrostatic Induction	Electromagnetic Induction (Lenz's Law)
Pros	<ul style="list-style-type: none"> • High Voltage • High Capacitance 	<ul style="list-style-type: none"> • High Voltage • Low Weight • Easy to scale 	<ul style="list-style-type: none"> • High output current • High Efficiency • Robust
Cons	<ul style="list-style-type: none"> • Pulsed Output • High Impedance matching 	<ul style="list-style-type: none"> • Low Capacitance • Pulsed Output • High Impedance matching • Parasitic capacitance can affect the performance significantly 	<ul style="list-style-type: none"> • Heavy • Poor Efficiency at lower frequency and small-scale devices

The next type of a generator that can be used for harvesting vibrational energy is an electromagnetic generator. These generators have very high energy density and that is why they are used in the current generation of electricity production. But due to magnetic field saturation and resistive losses, the efficiency of these generators decreases with a shrinking size of the generator. However, it is clear from the Scaling Law⁶ that the power density of these generators can decrease exponentially by a factor of 2 or increase by a factor of 1 as the size of the generator

decreases. However, the resistive losses could be so high that an increase in power density by a factor of 1 might not be achievable. Also, the output of these generators depends on the square of the frequency of operation⁷. Since the ambient vibrations are mostly low in frequency (Fig. 1-2), the performance of these generators might further degrade⁷. The inertial mass of electromagnetic generators is also very high; therefore, these generators may not be suitable for various ambient vibration sources.

The third type of generators is electrostatic generators. They are one of the oldest electrical machines invented⁸. Most of the earliest electrostatic generators worked on the principle of triboelectric effect. When two insulators make contact with one another, they develop surface charges due to friction. When these insulators separate, surface charges also separate, thereby creating a potential difference between them. This process of creating charges is referred to as triboelectric effect. This, together with the understanding of electrostatic induction, gave rise to several electrostatic generators. Some of the most notable electrostatic generators are a friction machine, Van de Graff generator, Wimhurst Machine, etc. Until the 19th century, most of the research on electricity was based on electrostatics generators but the energy they generated was small ($\sim 100 \text{ J/m}^3$ in air). The maximum electrostatic energy was limited by the dielectric breakdown of the ambient condition or the material⁸⁻¹¹. Also, there was unpredictability associated with the type and amount of surface charge generated during triboelectric process⁸. Thus, with the invention of Volta's wet cell and Faraday's electromagnetics, research in energy harvesting from electrostatic slowly declined and deviated to other areas such as electrostatic printing, precipitators, etc. However, with the miniaturization of devices, it was found that electrostatic forces at small scale are more prominent than magnetic forces. Again from the Scaling Law, it was shown that power density of these generators can increase from 1 to 2.5 order of magnitude⁶ as the device became smaller. However, as the devices become smaller the resonance frequency increases, making miniaturized devices unsuitable for harvesting ambient vibrational energy. In order to overcome this issue, Wang et al. proposed a unique solution that they termed "Triboelectric Nanogenerator(TENG)¹²". Instead of fabricating devices at the micro- or nano-scale, they proposed to fabricate macro-scale devices utilizing micro- or nano-structures for harvesting ambient energy¹³. Due to their micro- or nanostructure, these devices inherit the advantages of Scaling Law making it possible at the same time to harvest ambient vibrational energy. Moreover, the integration of TENG devices is quite simple and various device structures

(such as cylindrical, origami etc.) can be fabricated and assembled depending upon the type of energy sources available^{14,15}. Also, the low mass of the electrostatic generators makes it a more viable solution for this type of energy harvesting application. However, the parasitic capacitance can still significantly degrade the performance of these devices¹⁶.

Thus, from the above discussion, it is quite evident that electrostatic generators are a good option for harvesting ambient vibrational energy sources. And based on the technological advancements, TENG devices seem to be a good solution for harvesting this type of energy.

1.5 Triboelectric Nano-generators

Although TENGs study has been reported recently, this type of generators can be traced back to as early as the 17th century. Van de Graff generator, Wimhurst Machine, etc. are all examples of electrostatic generators that used triboelectric and induction effect for their operation^{8,13}. The power density of these devices was very small. However, with the development and fabrication of nanostructured patterns and materials, the efficiency and power density of TENG devices have significantly increased¹³. Many TENG designs have been proposed to harvest mechanical energy from different forms, such as physical movements (walking, running), sliding, rolling, wind, flowing liquid etc.¹⁴. The output power has been reported to increase from few mW/m² to 500 W/m² and the efficiency of 10 to 80% (depending on the design)³. Apart from energy harvesting, various self-powered applications such as chemical sensing, metal deposition, tactile sensing, photocatalytic activity, electronic circuitry etc. have also been demonstrated using TENGs^{3,13,14}. Easy assembly of the device structure, different types of devices, range of applications, high output power, and efficiency clearly demonstrate the versatility of TENG devices for harvesting energy from ambient conditions.

Even though the versatility of TENG devices has been proven, it has few limitations which arise from the triboelectric process itself. The triboelectric effect is not a well-understood process and, therefore, this device is associated with the unpredictability that can impede their progress for practical applications. Therefore, there is a need to understand triboelectric effect to ensure a reliable and efficient TENG device performance.

1.6 Triboelectric Effect

Triboelectricity is one of the oldest electrical phenomenon known to mankind^{8,9,13}. The first record of triboelectricity can be found in Greek literature dating back to 600 BC⁸. When two materials are brought into contact with each other, they develop static charges and become charged. This effect is known as the triboelectric effect or contact charging. To date, the cause of triboelectric charging has been a matter of debate. There are several factors such as surface chemistry, surface preparation technique, a method of contact charging, external environment, etc., which limit the understanding of the process and cause variability^{9,10}. The variability is evident from the several attempts made by researchers to create a triboelectric series^{9,10,17}. The triboelectric series is an empirical series in which several materials are arranged according to their polarity and amount of charge they can develop during contact electrification. Due to the empirical nature of the series, the phenomenon resulting in this arrangement of materials is not apparent¹⁷. This ambiguity has led to several hypotheses regarding the triboelectric effect.

However, at present, there are two leading conflicting theories to describe the effect. According to the first theory, triboelectric charges are produced due to the difference in the electronic band structure of the materials^{9,18,19}. The experimental evidence both supports^{20–24} as well as contradicts^{10,25–27} this mechanism. The second theory discusses the involvement of ions^{9,10,17,28–31}. But the kind of ions involved and the mechanism of ion generation itself during the contact electrification process is still being debated^{9,10,32,33}. Studies have reported that, together with ions, radicals are also generated during triboelectric charging^{34–36}. The stability of triboelectric charges has been proposed to be as a result of the generated radicals^{35–37}.

It should be noted that most of the processes pointed out above are associated with the atomic or molecular property of the materials. Nanoscopic studies of triboelectric effect can help understand the triboelectric charging mechanism and other associated processes. Scanning probe microscopy (SPM) has emerged as a powerful tool to characterize the origin of these charges at the nanoscale. The advances in SPM, especially Atomic Force Microscopy (AFM) and related techniques such as electrical (Kelvin Probe Force Microscopy (KPFM), Electrostatic Force Microscopy (EFM)), and magnetic (Magnetic Force Microscopy) characterization, are now being extensively employed to understand the surface charges and radicals relevant in understanding triboelectric charging mechanism^{32,34,35,38}.

1.7 Objective of the Thesis

The main goal of this thesis is to understand triboelectric charging mechanism. The objectives are divided into two parts. Firstly, our research looks into the charge generation mechanism between two interfaces. There are several reports on different aspects of the interfacial phenomenon during triboelectric charging^{10,24,31,39}. However, only limited studies have been devoted to the time required for charge generation^{35,40}. Previously, it was difficult to carry out this type of study as the two surfaces under contact were usually macroscopic in nature. But with the invention of Atomic Force Microscopy, it is now possible to probe the nanoscopic interaction between the two surfaces with control on parameters, such as contact force, time of contact, etc. By studying the time required for triboelectric charge generation, various processes happening at the interface and their implication on charge generation mechanism could be understood. This is particularly important while optimizing the device performance and related applications of TENG devices.

Second, our research explores the different aspects of radicals generated during contact electrification. Currently, all the TENG devices operate on heterolytic bond cleavage. The role of radicals in enhancing the performance of TENG devices has still to be explored. One of the key reasons for this is the limited understanding of the nature of the produced radicals, which restricts our ability to manipulate them. Therefore, the generation and stability of the radicals were investigated. Also, we investigated radical polymers for TENG devices. These studies shed light on the role of molecular design and nanostructure in high energy density TENG devices.

We investigate the nature of the charges and radicals on the surface by using AFM and the related techniques, such as KPFM, EFM, and MFM. We also studied the physics of contact mode TENG devices and radical polymer based TENG devices.

1.8 Outline of the thesis:

Chapter 1: This chapter provides an overall introduction to the thesis. We discuss a broad picture regarding the need and the available energy harvesting technology and different ways to harvest vibrational energy sources. Based on these discussions, it was emphasized that TENG devices have the potential for harvesting vibrational energy. Then, the chapter discusses the basic methodology and research approach.

Chapter 2: This chapter explores the role of time of contact during triboelectric charge generation process. To reduce the variability during triboelectric charge generation experiment, Taguchi Design was implemented. We study several factors, such as contact force, relative humidity, number of contacts, bias, and contact time. We propose that the dielectric relaxation in stern like ice layer was one of the factors controlling the charging process. We also noticed that the energy dissipated at the interface does not correspond to the amount of generated charge.

Chapter 3: The role of interfacial water during triboelectric charging was investigated. The presence of interfacial water could not be probed from EFM. However, with the help of Tapping mode, Phase imaging accumulation of interfacial water surrounding the charged region was observed. It was noticed that the phase shift during imaging was more than the one observed during Amplitude Phase Displacement (APD) curve. The increase in phase shift was proposed to be due to a combination of various factors such as a change in the imaging condition, the slope of the sample, etc.

Chapter 4: In this chapter, the basic physics of the contact mode TENG devices was discussed. The role of parasitic capacitance was examined. Utilizing the concept of minimum achievable charge reference state (MACRS), a simpler and easier way was proposed to evaluate the performance figure of merit of these devices. It was shown that parasitic capacitance can significantly influence the performance of TENG devices. Also, due to parasitic capacitance, the displacement of TENG devices needs to be optimized for higher performance.

Chapter 5: In this chapter, the role of radicals and the molecular design of materials on a TENG device performance was explored. At first, we explored, with the help of MFM, the generation of radicals during the triboelectric process. We found that both charges and radicals are generated at the same location and stay on the surface for an extremely long period of time. Also, it was noticed that charge dissipation led to the creation of more radicals while the role of pre-existing radicals in the polymer was examined with the help of radical polymer. We discovered that radicals, due to steric hindrance, do not participate in triboelectric charging. Also, we noticed that that the molecular design of polymer, together with nano-structure, has a significant influence on the performance of a TENG device.

2 Nano-scale study of triboelectric charge generation mechanism

2.1 Introduction

For efficient operation of triboelectric nanogenerator (TENG), two different materials which can yield a higher density of triboelectric charges are required^{3,41}. To achieve this goal, one often refers to triboelectric series, in which materials are arranged according to their charging tendency and the amount of charge they can develop on their surface^{9,17,42}. Materials which have a tendency to become positively charged are placed on top of the series, whereas materials which become negatively charged are placed at the bottom of the series. Based on the triboelectric series, materials at the two extreme ends are chosen to achieve higher performance with TENG devices. Although the problem of material selection for higher efficiency is solved using the triboelectric series, it, however, fails to address the origin of triboelectric charges and the reasoning behind the placement of different materials in tandem is not exactly clear^{9,10}. This introduces a lot of uncertainty during the device performance. In fact, this was one of the reasons why frictional electrification failed to become a commercially viable source for electricity production⁸. Therefore, it is very important to understand the mechanism involved in the charging process. This will not only help in controlling and manipulating the charge generation process that directly affects a TENG device performance but can also lead to some interesting scientific ideas that may result in the commercial availability of TENG devices.

There are many factors which contribute to triboelectric effect and most of them are associated with the interfaces. Contact electrification, being a surface phenomenon, is very susceptible to small changes, such as humidity, surface preparation technique, surface chemistry, contaminants on the surface, surface roughness etc^{17,25,42-49}. Most of these factors have already been reported and are well documented in the literature^{9,10}. For instance, it has been pointed out that the surface preparation technique might considerably change the amount of the generated triboelectric charges⁹. Similarly, the method of applying a force such as sliding might involve friction during triboelectric charge generation whereas rolling might not involve significant frictional force^{9,24,28,50}. To eliminate frictional force, charging with liquid has also been performed but it was found that material transfer might occur during the process^{9,51}. The study of triboelectric charge

generation process requires the above-mentioned parameters to be controlled and its implications need to be addressed.

Currently, there are two leading conflicting theories to describe the effect. According to the first theory, triboelectric charges are produced due to the difference in the electronic band structure of the materials^{9,18,19}. This theory correctly predicts electronic properties of metals and semiconductors. But since insulators have only bound electrons, it has been pointed out that electron transfer will be an endothermic process. The energy required for this endothermic process might range in the orders of several eV (the difference between HOMO and LUMO of two insulators). Therefore, electron transfer processes are unlikely to be involved during the charging process¹⁰. Another proposed mechanism is based on Lewis acid and base theory^{9,52}. The experimental evidence has supported^{20-23,53} as well as challenged^{10,25-27} these mechanisms.

The second theory discusses the involvement of ions^{9,10,17,28-31,36,37}. One of the most compelling proposed mechanisms is ion transfer across the interface at the point of contact. As the surfaces move away from each other due to asymmetry in the potential well, some of the charges get trapped on the surface, thus creating a net surface charge^{9,10}. Also, it is a well-accepted fact that almost every surface is covered with a layer of water depending on the relative humidity of the environment. The presence of water molecules was hypothesized to be the source of ions. The dependence of triboelectric charging on humidity further supports the hypothesis and role of ions in the process^{43,46}. However, it was reported that the presence of interfacial water is not necessary for the triboelectric charge generation⁵⁴. It was argued that bond cleavage of the substrate results in the charge transfer. Although it should be noted that in the same study with the presence of interfacial water, the amount of the produced charge increased significantly^{43,55-57}. All these theories were put to question with the observation that chemical reactions can be initiated by triboelectric processes⁵⁸. Several different oxidation-reduction reactions with a different electrochemical potential were presented. These reactions were interpreted as a result of the presence of electrons of unknown origin, i.e., crypto-electron⁵⁹⁻⁶¹. It was soon pointed out that during a triboelectric process, radicals are also generated along with ions^{34,35,62}. The presence of radicals might result in the observed electrochemical reaction. However, the kind of ions and the mechanism of ion generation during the contact electrification process are still being debated^{9,10,32,33}.

Another possible way of charge generation is the material transfer during the contact^{9,47,63}, which can lead to a reversal of charge polarity. The charge generation can take place from material transfer but the process might not be repeatable. It has been pointed out that both positive and negative charges reside on the surface^{32,64}. Therefore, the study of triboelectric effect should be done in such a way that material transfer is not a dominant factor.

Although the research on understanding triboelectric effect has been going on for more than a century, most of it was focused on macro-scale charge characterization^{9,30,34,42,43,46}. However, recent developments in the nanoscale characterization of the materials, specifically using Scanning Probe Microscopy (SPM), have contributed significantly to our understanding of triboelectric effect^{22–24,26,32,34,35,50,53,57}. Some of the key advances from the nanoscale study of triboelectric effect have already been pointed out above and in the earlier chapter. Therefore, in the present study, AFM is used to study the nanoscale charge generation mechanism. For this purpose, charges were generated from the AFM tip itself. Before discussing the experimental methodology and results, it should be noted that the definition of contact charging and triboelectric charging is slightly different. Triboelectric charging experiment can involve friction between two surfaces, whereas contact charging experiment does not include friction. In the case of AFM, the applied force may have a lateral component which can introduce the friction. The lateral component depends on the inclination of the AFM cantilever, the half angle of the tip, and the mounting angle of the substrate. Therefore, the charges created in this study are purely triboelectric as opposed to contact charging.

Most of the previous studies have considered only one factor at a time, i.e., focusing solely on force⁵⁰, bias^{20–22}, number of contacts^{23,32,35,54}, surface chemistry^{29,42}, humidity^{43,46,57}, etc. as a variable parameter. When these experiments were conducted, various other parameters were kept constant and a trend was observed for the polarity and amount of charge generated. However, as soon as any of the other parameters changes, the observed trend might change completely. Despite these detailed studies, relatively less consideration has been given to the time required for charge generation during the triboelectric effect. Contact time plays an important role in determining the rate of charge transfer across the interface. There are only a few reports^{44,49} which give the approximate time of contact (t_c). Most of these times are in the range of 100 ms to few seconds^{44,49}. The knowledge of t_c and the generated charge give us an idea about the type of mechanism involved during the process and can help in engineering a material with better electrical, chemical,

and mechanical properties for high energy density TENG devices. To study the role of t_c , we need to control other factors such as force, humidity, number of contacts, etc. However, as mentioned above, the observation can change as soon as control factors are changed. Hence, we used Taguchi Design where we studied multiple factors and determined the role of individual factors.

2.2 Taguchi Design and Selection of Factors:

In order to understand complex processes such as a triboelectric effect, it is better to design experiments in such a way that various parameters can be studied at a time. One way to study these complex processes is to employ orthogonal arrays (OA) matrix⁶⁵. There are various types of OAs that can be used to study this process, including full factorial design, fractional factorial design (Taguchi design), etc. In the present study, we employed Taguchi Design⁶⁶. The advantage of using Taguchi Design based OAs is that several factors can be studied in a relatively low number of experiments. There are other types of fractional factorial designs available as well, but Taguchi Design provides a standard way to analyze the results.

The working principle of Taguchi Design can be easily understood by an example. Let us consider we need to study 3 factors at two levels i.e., A (A_1, A_2), B (B_1, B_2) and C (C_1, C_2) where $A_1, A_2, B_1, B_2, C_1, C_2$ are the levels for each factor. From full factorial design, we need to conduct $2^3 = 8$ sets of experiments. These 8 sets of experiments can be easily visualized as 8 corners of the cubes as shown in Fig. 2-1. The condition for each corner is also mentioned with the figure. Among these 8 sets of experiments, we will get the effect of main factors (A, B and C) together with the interaction (AB, AC, BC, and ABC) between them. However, if we are interested in the effect of main factors only i.e., A, B and C, we can reduce the total number of experiments to 4 sets. Dr. Taguchi proposed that the selection of these 4 sets of experiments should be such that they should form an orthogonal array (OA) as shown by four dots in Fig. 2-1. It should be noted that the influence of all factors at each level are covered in this array. Similarly, experiments for a higher number of factors with more levels can be designed as has been done in the present study. Also, if some specific interactions are of interest then the modification of OA is also possible in a standard way. Hence the design and analysis are standardized. The analysis of Taguchi design will be discussed in the next section.

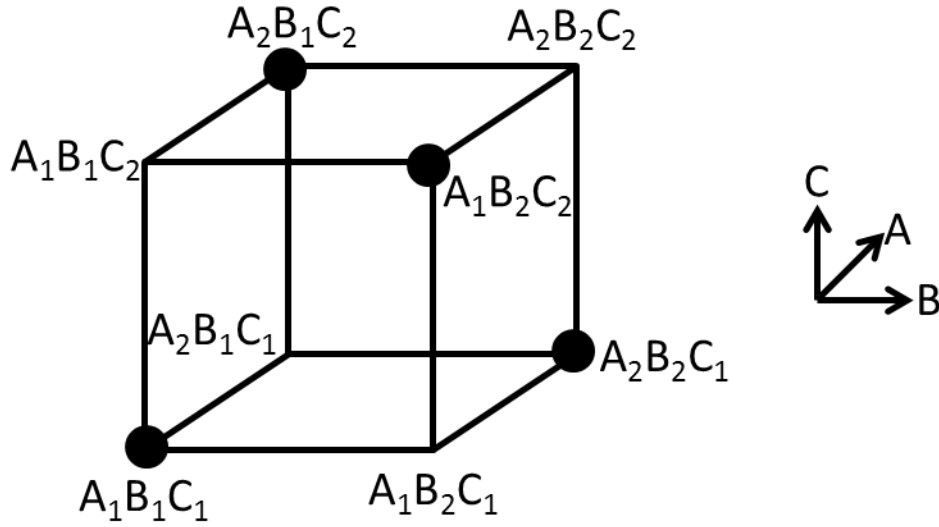


Fig. 2-1: An illustration of a factorial design for 3 factors at 2 levels and the selection of a set of experiments for Taguchi design. The four points in the cube show selection of experimental set for Taguchi design. The axis on the right shows the direction along which the level of each factor has been varied.

In the present study, we designed the experiments to focus only on the main effect of the factors (such as force, relative humidity, number of contacts, etc.), i.e., it was assumed that the factors do not interact among themselves. For instance, in the present study, we have considered four factors and each factor had 3 different levels. Unlike full factorial design requiring 64 different experiments, Taguchi Design only needs 9. This set of experiments is also referred as an L9 array. An example of how different factors and their levels are selected for Taguchi Design is given in Table 2-3 and Table 2-4 (the details of these tables are discussed later). Hence, Taguchi design can serve as a very good starting point to understand the role of various factors with relatively very less number of experiments.

As discussed above, there are several factors which play an important role during triboelectric charging mechanism. Among them, the following factors were considered in the present study:

- 1) Force: When the applied force increases, the amount of the produced charges will also increase. This is due to the fact that when the force increases, applied stress, and

deformation of the sample also increases. The dependence of force on triboelectric charge will indicate the involvement of bond breaking processes.

- 2) Tip Bias: The potential difference between two materials results in the transfer of charges and has been experimentally observed to influence the triboelectric charging process. In fact, this is one of the reasons which have compelled many researchers to conclude the involvement of electrons during the triboelectric charging process. The influence of tip bias on the triboelectric charging process will suggest whether the process is electronic or ionic.
- 3) Number of Contacts: The amount of charge produced will increase with the increasing number of contacts. However, after a certain number of contacts, charge generation will start to saturate. This will give an idea about the type of mechanisms (whether it is due to surface state or other processes) involved in the charging process.
- 4) Time of Contact (t_c): When two surfaces make contact, there is a finite amount of time during which they remain in contact before separating. There are several processes, such as charge generation, transport, and recombination for which time can be a crucial factor. Thus, the time required for triboelectric charges to occur might depend on t_c . An understanding of the t_c and the produced triboelectric charges can again give an idea about the various involved processes and their nature.
- 5) Relative Humidity (RH): As the RH increases, the amount of interfacial water also increases. The presence of water can influence charging in several ways. Firstly, it can act as a source of ions (H_3O^+ , OH^-). Secondly, it can provide a path for ion transfer from one interface to the other. Thirdly, mobile ions can dissipate the triboelectric charges as well. Therefore, based on the observations, the mechanism according to which relative humidity influences triboelectric charging can also be determined.

2.2.1 Analysis of Variance (ANOVA Analysis):

In case of Taguchi Design, several factors are varied simultaneously. Therefore, the analysis of the Taguchi Design is based on ANOVA⁶⁶. At first, “Marginal Mean” i.e., an average of each level associated with different factors are determined. For instance, in Table 2-4, for 5 number of scans, the contribution can be determined by taking the average of the experiment, E1, E2, and E3. This average is referred to as Marginal Mean of 5 scans. Thus, the potential generated by 5 scans is 24.8 mV. Similarly, other marginal means for each level of different factors are determined. The calculated means are then plotted to observe the trend with different factors as shown in Fig.

2-2(blue line). The observed trend is then compared to the confirmation experiment as shown in Fig.2-3 (blue line). This analysis only predicts the trend which might be observed but it does not indicate whether the given factor is statistically significant. In order to qualify the results obtained from Taguchi design, a confidence test needs to be performed on the obtained results. Apart from confidence interval test, this technique also helps in identifying the weighted contribution from different factors. To perform the analysis, at first the total sum of squares and factor sum of squares are calculated:

$$SS_T = \sum_{i=1}^N (Y_i - \bar{Y})^2 \quad \text{Eq. 2-1}$$

$$SS_A = \sum_{i=1}^{L_A} \left(\frac{A_i^2}{n_{A_i}} \right) - \frac{T^2}{N} \quad \text{Eq. 2-2}$$

where, SS_T is the total sum of squares, SS_A is the sum of square of factor A , Y_i is the i^{th} observation, \bar{Y} is the average of all observations, N is the total number of observations made (18 in the present case), A_i is the sum of all observations at i^{th} level for the factor A , L_A is the total number of level for factor A (3 in present case), n_{A_i} is the total number of observations involving factor A (6 in the present case), and T is the total sum of factor given as, $T = \sum_{i=1}^n Y_i$. $\frac{T^2}{N}$ is the correction factor.

After calculating SS_T and factor sum of squares, error sum of squares (SS_e) is calculated which is given by Eq. 2-3. The error terms include effect of various factors that have not been taken into account in the present study (such as chemical heterogeneity, variation in thickness of insulator, etc.)

$$SS_e = SS_T - (SS_A + SS_B + \dots) \quad \text{Eq. 2-3}$$

Next degree of freedom associated with each factor was determined. The total degree of freedom (f_T) is given as, $N - 1$, degree of freedom for each factor is given as $f_A = L_A - 1$, and degree of freedom of error is given as $f_e = f_T - (f_A + f_B + \dots)$. Thus, in the present study, there are four

different factors and each of them is divided into 3 different levels. Hence, the total degree of freedom for each factor is 2. If only one set of experiments is conducted, then $N = 9$, $f_T = 8$ and $f_e = 0$. Thus, for ANOVA analysis of Taguchi Design, a repeatability of each set of experiments is required. For two repetitions, $f_e = 9$. After determining the degree of freedom, variance of each factor and error is calculated and is given as:

$$V_A = \frac{SS_A}{f_A} \quad \text{Eq. 2-4}$$

and

$$V_e = \frac{SS_e}{f_e} \quad \text{Eq. 2-5}$$

$$F_{f_A, f_e} = \frac{V_A}{V_e} \quad \text{Eq. 2-6}$$

The ratio of the variance of a factor to the variance of the error gives F-ratio (Eq. 2-6). This ratio determines the statistical significance of each factor at a predetermined risk level (α). The α in this study was 0.05. In the present case, this F-ratio ($F_{2,9}$) was determined to be 4.26. The subscript 2 is the degree of freedom of each factor and 9 is f_e . If the value of F-ratio is lower than 4.26, it is considered to be statistically insignificant. This is the case for the number of scans for experiments at three different RH conditions (Table 2-5)

The percentage contribution is calculated as:

$$\% \text{ Contribution} = \frac{SS_A}{SS_T} * 100\% \quad \text{Eq. 2-7}$$

The F-ratio and the percentage contribution of different factors for Table 2-5 are calculated and is given in Table 2-3.

2.3 Experimental Method:

For the present study, we used a thin film of Poly(methyl methacrylate) (PMMA) as a substrate material. PMMA was procured from Sigma Aldrich and the average M_w as 120,000. PMMA was spin-coated on Pt (100 nm) on the thermally grown SiO_2 substrate. PMMA substrate was chosen as it is an important polymer for microelectronic⁶⁷ industry and has been substantially used as one of the dielectric materials for TENG devices^{68,69}. For spin coating, 10 wt% of PMMA in toluene was prepared and stirred overnight. Spin coating was done by a home-made spinner. The thickness of spin-coated PMMA was 500 ± 50 nm. Before starting the experiment, PMMA substrate was cleaned with DI water and ethanol and stored in vacuum overnight to make sure that no solvent or external charges were present.

To generate and detect charges on PMMA, Pt-coated Si cantilever and bare Si cantilever (MPP-21100-10) were used. 100 nm Pt/10 nm Ti coating was done on Si tip by sputtering to prepare Pt-coated tip. All the studies were done on Bruker MultiMode 8 AFM system with Nanoscope V controller. Before starting the experiment, the AFM tip was calibrated on the rigid SiO_2 substrate to determine its sensitivity. The thermal spectrum of the cantilever was acquired and fitted with the in-built Bruker Nanoscope program to estimate the resonance frequency and the spring constant of the cantilever. In this study, the charges were generated using Peak Force Tapping Mode®. The surface potential readings were taken from Amplitude Modulated- Kelvin Probe Force Microscopy (AM-KPFM) at a lift height of 100 nm. Additionally, Electrostatic Force Microscopy (EFM) data were also collected.

To control the humidity, fluid AFM head was used. Electrical connection between the tip and the fluid head was established by soldering a wire (Appendix B). Humidity was controlled by purging a mixture of dry and humid nitrogen. The total flow rate was kept constant at 100 sccm. RH was controlled within $\pm 5\%$. The schematic of the setup is given in Appendix B.

For Taguchi design, once the factors are fixed, there are various other AFM related parameters which need to be adjusted to achieve their respective levels and reduce the variability during the experiments. To generate charges on the surface, the total time for each scan was kept constant irrespective of the tapping frequency. Also, the scan length and the total number of taps per line (samples/line) were kept constant. Therefore, the aspect ratio and the scan rates were varied to

maintain the same number of taps for each scan. The details of how these parameters were adjusted are given in Table 2-1.

The Force-displacement curves were acquired after each charging study. This was done to check the changes in the tip radius since adhesion force is directly proportional to tip radius (details will be discussed later). The F-Z curve analysis was performed by SPIP software. For the F-Z curve analysis, it was assumed that the interaction between tip and substrate is governed by DMT (Derjaguin, Muller, and Toporov) contact mechanics model. The sensitivity and the spring constant of the cantilever were provided from the initial calibration of the AFM tip.

Table 2-1: Parameters used during Peak Force Tapping Mode to create the surface charges.

Peak Force Tapping Mode Parameters	Value
Scan Length	Fixed (10 μ m)
Aspect Ratio	Varied (=2000/Tapping Frequency)
Samples/line	Fixed (256)
Scan Rate	Varied (=Tapping Frequency/2000)
Scan Time	Fixed (=Scan Rate* Aspect Ratio*Pixels)

The electrical properties of the surface were accessed using AM-KPFM or EFM. Both AM-KPFM and EFM are a double pass technique. In the first pass, the topography of the sample is acquired using Tapping Mode. In the 2nd pass, tip lifts to a certain height (100 nm in the present case) and follows the path traced by topography. For AM-KPFM, during 2nd pass, an ac bias is applied either to the tip or the sample that interacts with long-range electrostatic forces. Electrostatic interaction will be discussed in detail in Chapter 3. With the help of KPFM feedback loop, tip bias (in the present case) is varied and amplitude is monitored. When the oscillation amplitude drops to zero, the feedback bias is recorded as the potential of the surface. It should be noted that during topographic imaging, there is a possibility that the tip might interact with the substrate and create charges which will depend on drive amplitude and amplitude setpoint⁵⁰. Therefore, the drive amplitude and amplitude setpoint were selected in such a way that during mapping of surface potential, no extra surface charge should be produced during the topography imaging. This fact

was also verified by the experiment. The parameters used during the AM-KPFM or EFM scanning are given in Table 2-2.

Table 2-2: Parameters used during AM-KPFM and EFM scanning.

Fixed-Parameter	Comment
Scan Size	15 μm
Scan Rate (Hz)	1 Hz
Tapping Mode Free Amplitude (A_0)	The free amplitude was kept small and constant ($\sim 25\text{-}30\text{ nm}$). When the tip approaches the surface, due to Van der Waals interaction, the free amplitude decreases. This amplitude will be referred as A_1 .
Tapping Mode Amplitude Setpoint	Amplitude set-point for each scan was kept closer to A_1 , so that the force between tip and sample during AM-KPFM should be small and the scan should not produce any extra charge $(0.8\text{-}0.9)* A_1$.
Samples/Line	Fixed (256)
Lift Height	100 nm (unless or until specified otherwise).

The analysis for the surface potential data was done using Nanoscope Analysis software (V.1.40). For the analysis, the surface potential image was at first flattened by zero order. This was done to offset the background surface potential from some arbitrary value to close to zero potential. The histograms of the region of interest (the region where surface charges have generated) were then collected. The histograms were analyzed by fitting a Gaussian curve using Origin Software. After the Gaussian fitting, the mean (x_c) and sigma (σ_c) were noted as the mean and the standard deviation of the surface potential generated. In some cases due to the poor resolution of AM-KPFM^{70,71}, a tail was observed in the histogram. For those cases, two Gaussian curves were fitted. The Gaussian fit farther from the zero potential was considered as the true surface potential generated due to surface charges and the mean and standard deviation were noted. For EFM, the frequency shift of the cantilever was recorded at several different lift heights or tip bias. The EFM results were analyzed by the same procedure used for surface potential analysis. To determine the tip radius of AFM tip, SEM images were acquired from Zeiss Sigma FESEM. The tip radius was determined using ImageJ software.

2.4 Results and Discussion:

We conducted the first set of experiments using uncoated Si tip. For L9 array bias, force, tapping frequency, and a number of scans were taken as control factors. We then study these control factors for three different RH (20, 50 and 80%). The level of each control factor is given in

Table 2-3. It should be noted that at RH 20%, the positive bias has a value of 2V whereas 1V was used for RH 50 and 80%. An example of L9 experiment for RH 50% together with the results are given in Table 2-4. The experiments were conducted in a random sequence. It should be noted that the standard deviation calculated in Table 2-4 is the mean value of R_1 and R_2 . In general, AM-KPFM has a poor lateral resolution and accuracy (~ 10 mV)^{70,71}. Therefore, the standard deviation in Table 2-4 is significantly lower than the actual resolution of AM-KPFM, which suggests a good reproducibility in the observations.

Table 2-3: Control factors and their levels for the study from uncoated Si tip.

Control Factors	Levels
Number of Scan (-)	5, 10, 15
Tapping Frequency (kHz)	0.25, 1, 2
Applied Force (nN)	10, 25, 40
Bias (V)	-2, 0, 1 2*
* was used only for RH 20%	

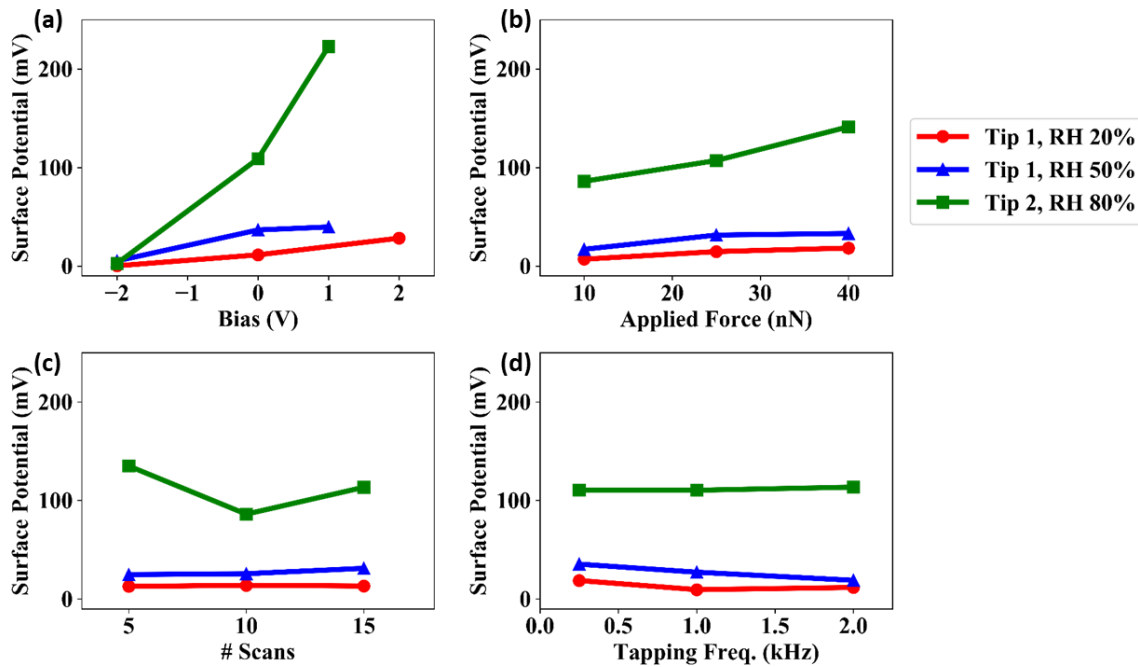


Fig. 2-2: Predictions from Taguchi Design for (a) bias, (b) applied force, (c) number of scans and (d) tapping frequency. The prediction for all three relative humidity level has been plotted.

As discussed in the ANOVA analysis section, the “Marginal mean” for each control factors at different levels was determined (Fig. 2-2). We also carried out the experiments to confirm that the observed trend (Fig.2-3). It should be noted that for the confirmation experiments, the parameters used for all three RH conditions were random. This prevents the analysis from any kind of skewness due to some unknown sources. From Fig. 2-2 and Fig.2-3, it can be noticed that the prediction from Taguchi design for tip bias and applied force are similar to the confirmation experiments. However, for the number of scans and tapping frequency, Taguchi prediction deviates from the confirmation experiments. The details of these observations will be discussed in the later section. The contribution of different factors and their respective significance level is given in Table 2-5.

Table 2-4: An example of an L9 set of Taguchi Design used in this study.

Exp	#Scans	Scan Freq	Applied Force	Bias	Surface Potential (mV)		Average (mV)	Std. Deviation
					R ₁	R ₂		
E1	5	0.25	10	-2	-1.2	2.9	0.9	2.9
E2	5	1	25	0	40.5	36.5	38.5	2.8
E3	5	2	40	1	38.1	31.8	35.0	4.5
E4	10	0.25	25	1	47.4	53.8	50.6	4.5
E5	10	1	40	-2	14.7	4.5	9.6	7.2
E6	10	2	10	0	19.7	13.8	16.8	4.2
E7	15	0.25	40	0	55.2	54.1	54.7	0.8
E8	15	1	10	1	37.3	29.6	33.5	5.4
E9	15	2	25	-2	8.6	1.9	5.3	4.7

Table 2-5: F-Ratio and contribution of each factor.

Factors	DOF	Tip 1, RH 20%		Tip 1, RH 50%		Tip 2, RH 80%	
		F-ratio	% Contribution	F-ratio	% Contribution	F-ratio	% Contribution
# Of Scans	2	0.14	0.10	3.58	2.22	3.93	4.23
Tapping Freq. (kHz)	2	11.64	8.79	20.29	12.56	0.02	0.02
Applied Force (nN)	2	16.53	12.49	23.53	14.57	5.11	5.49
Bias (V)	2	99.56	75.21	109.61	67.87	79.44	85.42
Error	9		3.40		2.79		4.84

It should be noted that two different tips were used for the study. Tip 1 was used for experiments at RH 20 and 50%. Also, a few sets of experiments were conducted at RH 80%. Due to repeated scanning, Tip 1 suddenly became blunt and the adhesion force increased drastically (Fig. 2-4e). Due to a higher adhesion force, AM-KPFM imaging could not be performed. Hence, a new tip, Tip 2, was used to complete the RH 80% experiments. The effect of tip geometry on the triboelectric charge generation will be discussed in the next section.

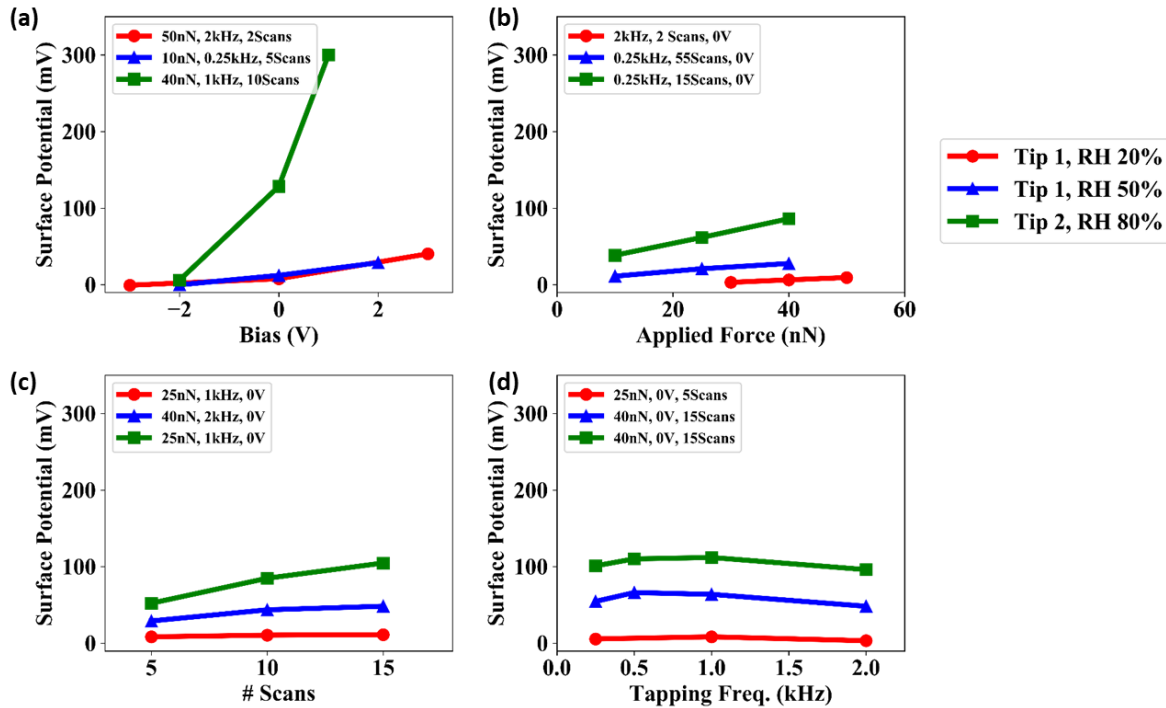


Fig.2-3: The above graphs show the confirmation experiment done to verify the predicted trend from Taguchi Analysis for (a) bias, (b) applied force, (c) number of scans and (d) tapping frequency. The results for all three different relative humidity levels have been plotted. For confirmation tests, the parameters for different experiments were chosen at random. The condition for each confirmation test is given with their respective plots.

2.4.1 Effect of tips:

To interpret the results obtained from Taguchi Design, it is important to understand how the AFM tip might affect the triboelectric charge generation process. An understanding of tip geometry will

give a clear idea about contact area, contact stress, energy dissipation, etc. between the tip and the substrate during triboelectric¹⁰ charging since every AFM tip has a different tip geometry. The difference in tip geometry can be easily identified from force vs separation curve i.e., from the approach (Fig. 2-4a) and retract curve (Fig. 2-4b). It is quite evident that the two tips have completely different tip geometry. The variation in tip geometry might result in the variation in triboelectric charge generation. This variation in tip geometry can be identified from the adhesion force^{72,73} (using the DMT model) between the tip and the substrate as shown in Fig. 2-4c. It is given as:

$$F_{ad} = 4\pi\gamma R_{eff} \quad \text{Eq. 2-8}$$

where γ is the interfacial surface tension and R_{eff} is the effective radius given as:

$$R_{eff} = \left(\frac{1}{R_{Tip}} + \frac{1}{R_{substrate}} \right)^{-1} \quad \text{Eq. 2-9}$$

The upper green triangle is the mean value of the adhesion force (Fig. 2-4c). In general, it is expected that as the RH increases, the adhesion force will increase due to capillary condensation. Hence, an increase in the adhesion force with increasing relative humidity, for the Tip 1, is expected. When the Tip 1 became blunt at RH 80%, the adhesion force increased to 60 nN (Fig. 2-4e). To further verify whether the tip geometry was different, SEM images of both tips, along with an unused Si tip, were taken (Fig. 2-5). From Fig. 2-5b, one can see that Tip 1 got blunt. Also, it appears that the tip might have fractured. For both tips, a certain amount of foreign material, i.e., PMMA, is observed. Therefore, the material transfer may play a role during triboelectric charging. Also, the interaction between tip and substrate might be of chemical nature.

As already mentioned before, it is assumed that the interaction between tip and substrate follows DMT model. According to the DMT model⁷³, the contact radius (a), deformation (δ), and axial stress ($\sigma_z(0)$) between the tip and substrate are given as:

$$a = \left(\frac{3F_{total}R_{eff}}{4E^*} \right)^{1/3} \quad \text{Eq. 2-10}$$

$$\delta = \frac{a^2}{R_{eff}} \quad \text{Eq. 2-11}$$

$$\sigma_z(0)|_{r=0} = - \left(\frac{6F_{total}E^{*2}}{\pi^3 R_{eff}^2} \right)^{1/3} \quad \text{Eq. 2-12}$$

where, F_{total} is the total force by Eq. 2-13, E^* is the effective modulus given by Eq. 2-14. $F_{applied}$ is the applied force and F_{ad} is the adhesion force. The mechanical properties of both tip and substrate are given in Table 2-6.

$$F_{total} = F_{applied} + F_{ad} \quad \text{Eq. 2-13}$$

$$E^* = \left(\frac{1 - \nu_{tip}^2}{E_{tip}} + \frac{1 - \nu_{substrate}^2}{E_{substrate}} \right)^{-1} \quad \text{Eq. 2-14}$$

The tip radius of Tip 2 was determined to be around 55 nm from Fig. 2-5:c. But the tip radius of Tip 1 was not determined as the tip was fractured during imaging. Since the mean adhesion force from both tips was known (Fig. 2-4c) and it changes slightly with RH (for Tip 1), the contribution from capillary condensation can be ignored. Using Eq. 2-8 the γ between tip and substrate was determined, which gave us the effective radius of Tip 1. Here it was assumed that the interaction between tip and substrate is similar and the tip radius is smooth (no surface roughness). Once the tip radius was known, the contact radius and axial stress for an applied force of 40 nN were determined. It is given in Fig. 2-4d. In order for the DMT model to be valid, the contact radius should be less than 10% of the tip radius. Although this condition is satisfied for Tip 1, this value is slightly higher (~15%) for Tip 2, however, the contact radius and axial stress are likely to be in the same range. Therefore, a variation in tip geometry might result in a variation in triboelectric charge generation. It should also be noted that the estimated axial stress (Fig. 2-4d) is significantly greater than the flexural strength of PMMA.

Table 2-6: Mechanical properties of PMMA and Si.

Property	Value
E_{PMMA}^{74}	2.5 GPa
ν_{PMMA}^{74}	0.37
$\sigma_{\text{TS, PMMA}}^{74}$	70 MPa
E_{Si}^{75}	110 GPa
ν_{Si}^{75}	0.24

2.4.2 Effect of Bias:

According to the Taguchi Design, as the tip bias increases, the surface potential increases (Fig. 2-2a). When a positive bias is applied, positive surface charges were produced, whereas with a negative bias, nearly none or slightly negative surface charges were produced. The confirmation experiments (Fig.2-3a) also verified the trend predicted by Taguchi Analysis. Thus, bias has a distinct effect on the generation of the triboelectric charge. It is important to note that as the RH increases, the slope of surface potential with respect to the bias also increases. This effect might occur due to two different reasons. First, the ions could be generated due to the electric field produced by the contact potential difference (CPD)¹⁰. It has been reported that water molecules can be dissociated at an electric field of 0.2-0.5 V/Å⁷⁶. Now, if we consider CPD (from Fig. 2-6a) of 0.7 V and tip-sample distance of 0.280 nm⁷⁷ (diameter of a water molecule), the generated electric field is 0.25 V/Å, which is in the range of the field required for water dissociation. Therefore, the dissociation of water molecule due to the field generated from CPD could be possible. Also, as the RH increases, the amount of interfacial water also increases and, therefore, hydronium (H₃O⁺) and hydroxyl (OH⁻) ions generation can also increase. It should be noted that for RH 80%, the CPD of Tip 1 and Tip 2 were different. This variation might have occurred due to the difference in the surface chemistry of the tip. The surface charge density was determined by assuming a parallel plate capacitor²²:

$$\sigma = \frac{\epsilon_0 * V}{d} \quad \text{Eq. 2-15}$$

where σ is the surface charge density, ϵ_0 is the permittivity of free space, V is the potential difference between tip and substrate, and d is the thickness of PMMA.

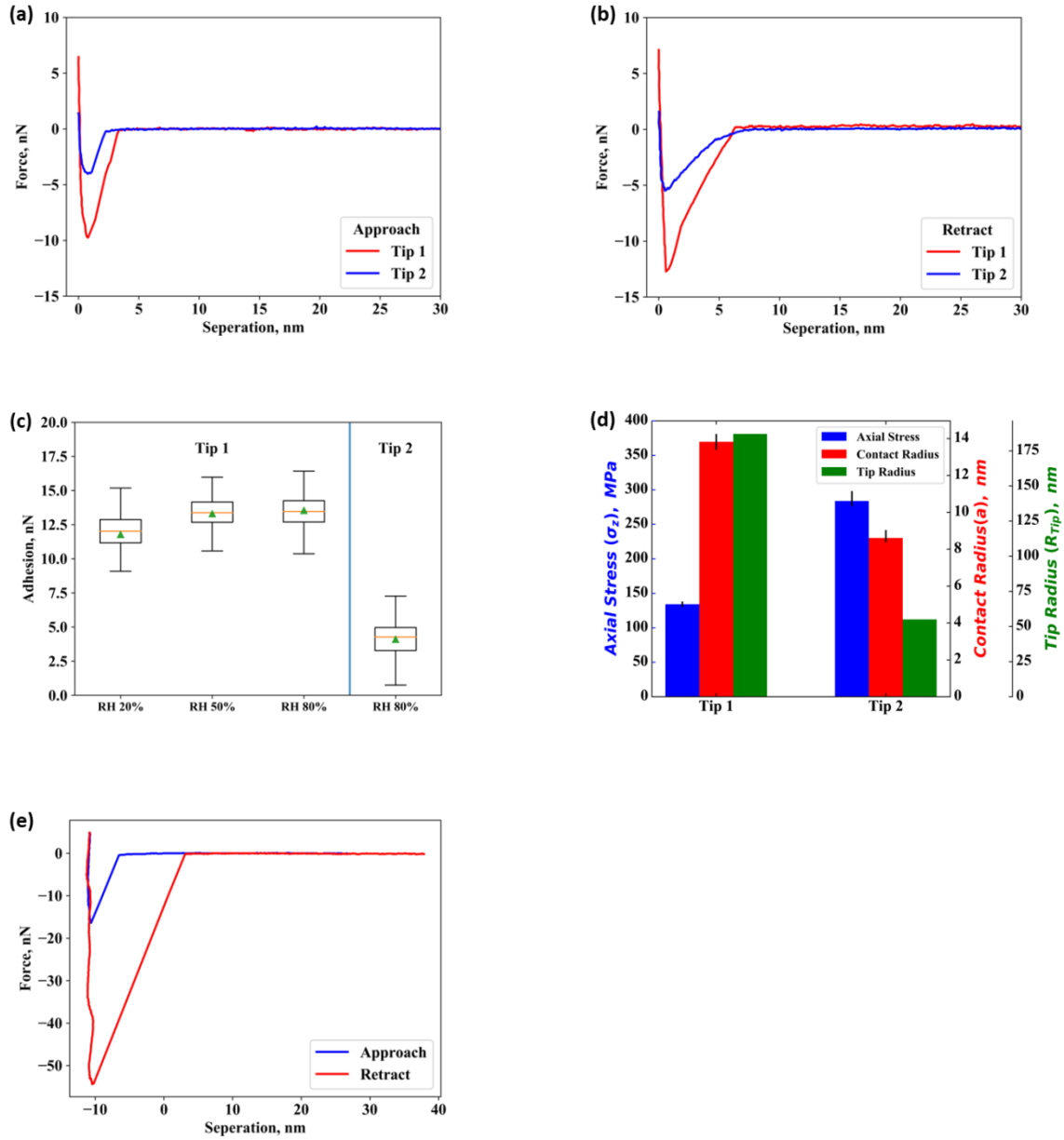


Fig. 2-4: Adhesion force between Si tip and PMMA substrate (a) for Tip 1 at different RH, (b) at RH 80% for different tips and (c) the axial stress, contact radius, and tip radius of the three tips calculated for the applied force of 40 nN.

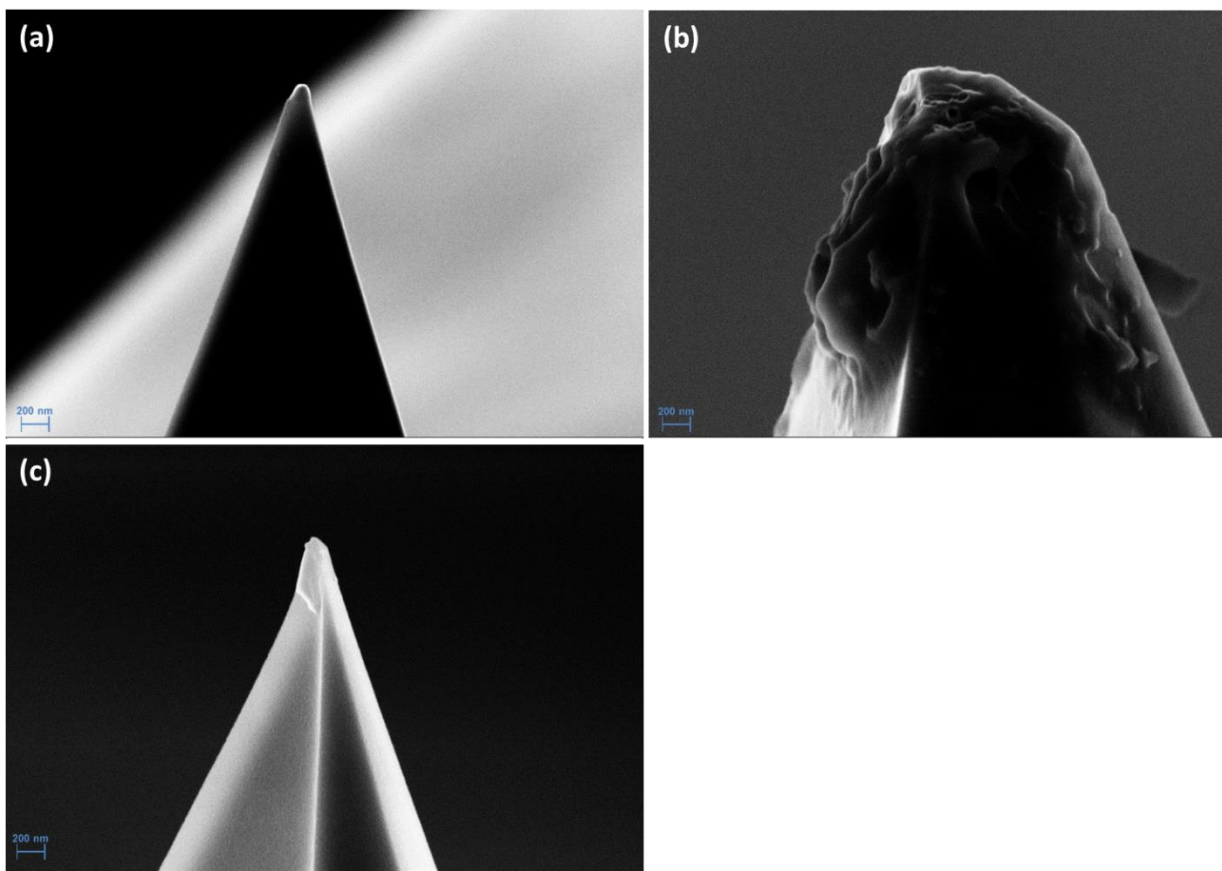


Fig. 2-5: SEM images of (a) Unused Si cantilever, (b) Tip 1, (c) Tip 2.

The other reason could be the change in HOMO and LUMO levels of the two materials. By varying the tip bias, the energy levels between tip and substrate can vary, influencing the amount of the generated charge. This manipulation of CPD is reported to alter the surface states^{18,22}. It was observed that as the RH increases, the CPD between the tip and uncharged PMMA also increases. Therefore, the generated surface charge was compared to the CPD between the tip and uncharged PMMA (Fig. 2-6b). Therefore, based on these observations, we cannot state conclusively whether the charge was generated by the surface state manipulation or dissociation of a water molecule.

However, among the four factors considered for the Taguchi Analysis, tip bias was found to be the most statistically significant factor influencing the triboelectric charge generation process. In fact, from Table 2-5, it is clear that tip bias contributes more than 75% to the charge generation.

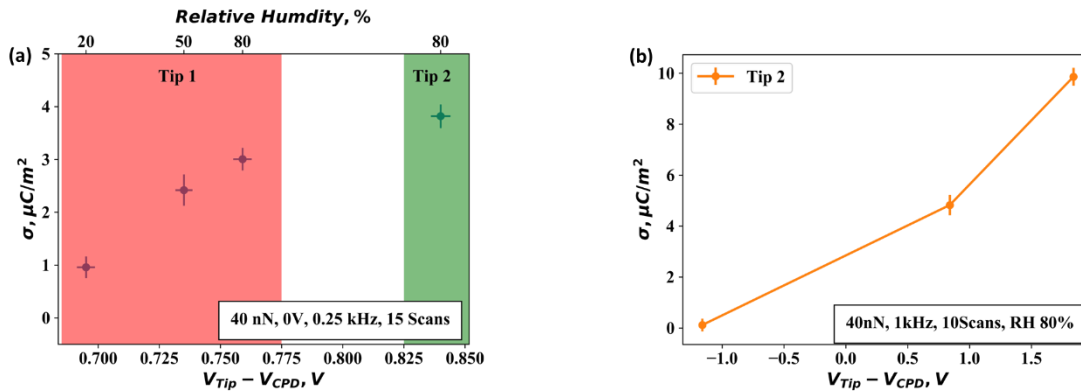


Fig. 2-6: Comparison of (a) the generated triboelectric charge density vs the potential contact difference between the tip and uncharged PMMA. The above values were obtained at a tapping frequency of 0.25 kHz, applied force of 40 nN; the number of scans was 15 and the bias applied was 0V. (b) Triboelectric charge density for different tip bias at RH 80% from Tip 2. These results were obtained by applying a force of 40 nN, 1 kHz tapping frequency and 10 scans.

2.4.3 Effect of Force:

It is known that as the applied force increases, the amount of the produced triboelectric charge also increases, which is evident from the marginal mean plot (Fig. 2-2b). Confirmation experiments also predict the similar trend (Fig.2-3b). These results are quite intuitive as an increased force means more sample deformation, which leads to more breaking of bonds. It should be noted that for both the tips, the amount of axial stress between the tip and substrate is higher than the flexural strength of the PMMA (Table 2-6). Hence, the produced triboelectric charges are independent of the axial stress and depend only on the deformation during the contact that is predominantly plastic in nature (Fig. 2-7a, b, and c).

During plastic deformation, few bonds will break either homolytically or heterolytically^{32,34,35}. In case of homolytic bond cleavage, when a bond breaks, the shared electrons are divided equally between two sides ($\text{R-R} \rightarrow \text{R}\cdot + \text{R}\cdot$), which leads to the formation of radicals but does not create any charges. While in heterolytic bond cleavage, the shared electrons go only to one side ($\text{R-R} \rightarrow \text{R}^+ + \text{R}^-$), which results in the separation of the charges³⁵. It is being hypothesized that both charges exist during the triboelectric charging process but generally, one type of a charge dominates over

the other^{9,32,63,64}. This can happen due to the presence of functional groups or specific adsorption of certain molecules at the interface. In the present case, the map of surface potential arises only due to the heterolytic bond cleavage processes.

The ANOVA analysis (see Table 2-5) also suggests that the applied force has a significant contribution to the triboelectric charge generation process. It should be noted that the bond cleavage process discussed above is generally endothermic in nature¹⁰ and since the deformation is plastic in nature, most of the energy will be dissipated during the contact. According to the DMT model⁷³, the contact stiffness is given as:

$$k = 2aE^* \quad \text{Eq. 2-16}$$

Also, since we know the total deformation during the contact, the total energy dissipated during the contact can be calculated as:

$$E_{dissipation} = \frac{1}{2}k\delta^2 = \frac{a^5E^*}{R_{eff}^2} \quad \text{Eq. 2-17}$$

The energy dissipation for different applied forces is shown in Fig. 2-7c, d. The energy recovered due to elastic deformation is significantly lower than the plastic deformation. A clear correlation can be seen between the calculated dissipated energy and the triboelectric charge density generated from the two tips. The calculated energy dissipation was found to be lower than the experimentally obtained energy dissipation for Tip 2. The reason behind this could be that the calculated axial stress was higher than the flexural strength of PMMA. The contact mechanics between the tip and sample will change as the applied stress cannot be higher than the flexural strength of PMMA and thus more deformation can occur in PMMA compared with the calculated deformation.

2.4.4 Effect of number of contacts:

The scan size for creating triboelectric charges in the present study was 10 μm and the total number of samples per line was 256. This suggests that during the charging process the distance between each tap was around 39 nm (=10 μm /256), which is greater than the contact diameter for both tips (Fig. 2-4d). Hence, the number of scans and the number of contacts between the tip and substrate

at each individual pixel can be considered equal. In general, as the number of scans increases, the triboelectric charges should increase and should saturate after a certain number of scans. However, the marginal mean plot suggests that as the number of scans increases, the amount of produced charges increases at first and then gradually decreases. From the ANOVA analysis, it is quite clear that number of scans does not have a significant impact, and the F- ratio for a number of scans is well below the 90% confidence interval. The observed trend cannot be considered as the actual response of the process. However, according to the confirmation tests, at all three RH levels with increasing number of scans, more charges were produced.

An important conclusion can be drawn from the effect of a number of contacts: the charge transfer due to material transfer across the interface might not be significant. If the charge generation was due to material transfer, the rate of charge generation would have been higher. Also, the variation in the surface potential would have increased⁴⁷ and the contribution from a number of contacts would have been significant.

2.4.5 Effect of Relative Humidity (RH):

To study the effect of RH, we conducted experiments at RH of 20, 50 and 80% with Tip 1. The results are given in Fig. 2-8. Before discussing the role of humidity, a few points must be noted:

- 1) As the RH increases, the amount of interfacial water on the surface also increases⁷⁸.
- 2) Water is a dipolar molecule, therefore, if charges are present on the surface, there should be a force of attraction between the water molecule and the charge⁷⁹.
- 3) Water contains mobile ions such as hydronium, hydroxyl, etc⁷⁸.
- 4) Interfacial water has significantly different properties compared to bulk water, such as dielectric permittivity, the presence of ions, molecule orientation, ion mobility⁷⁷ etc.

The increase in interfacial water can be observed by the adhesion force in the Force-separation curve (Fig. 2-8a, b). From Fig. 2-8b and Fig. 2-4c, the adhesion force between the tip and substrate changes slightly, suggesting only a slight increase in interfacial water. Since PMMA is a hydrophobic polymer, the water on the surface of PMMA can be assumed to be ice-like⁷⁹.

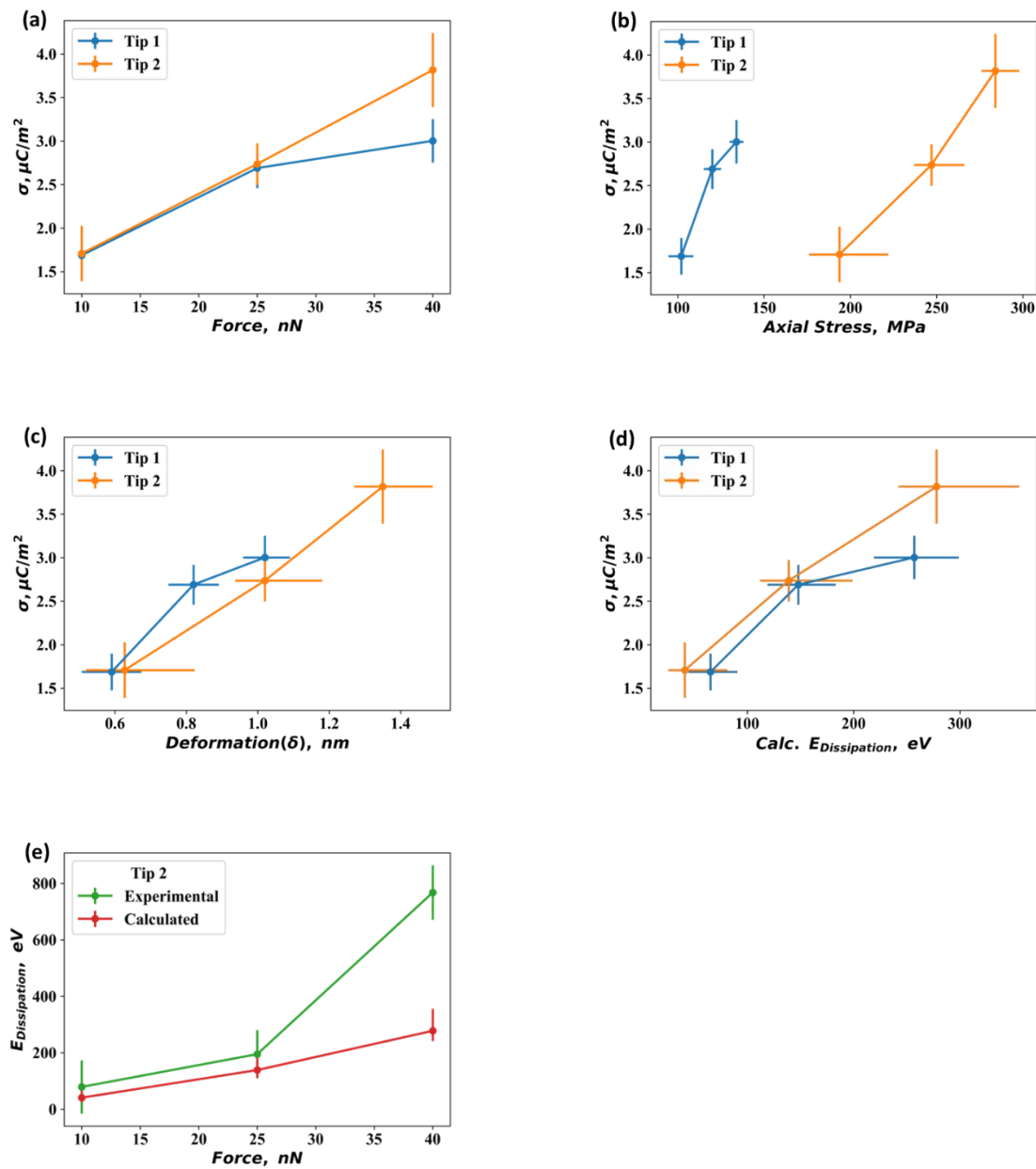


Fig. 2-7: Effect of (a) force, (b) axial stress, (c) deformation, (d) calculated energy dissipation on triboelectric charge density generated with both Tip 1 and 2. The triboelectric charge was generated by applying 0V bias, 15 scans, RH 80% and tapping frequency of 0.25 kHz. (e) Comparison of calculated energy dissipation and experimentally obtained energy dissipation for Tip 2.

In Fig. 2-6a, it was shown that CPD between the tip and substrate was negative and decreased as the relative humidity increased. Also, the electric field due to CPD will assist in diffusion of ions. It has been reported that the diffusion of H_3O^+ and OH^- depends on the scale⁸⁰, i.e., in a narrow channel (like CNTs) diffusion of OH^- is greater than H_3O^+ whereas in bulk water H_3O^+ has higher diffusivity than OH^- . It has been reported that the neutral surface of the water is negatively charged^{79,81,82} and, therefore, a decrease in CPD suggests the presence of OH^- ions, i.e., an increase in ion density. From Fig. 2-8c, it is clear that the triboelectric charge density increases as the relative humidity increases. Also, from the discussion in Section 2.4.2, we noticed that the ions can be generated due to the electric field between the tip and PMMA. The energy dissipated at the contact was calculated for three different RH and is shown in Fig. 2-8d. It should be noted that the dissipated energy has been obtained for an applied force of 7 nN and a scan rate of 1 Hz. The trend for an applied force of 40 nN and tapping frequency of 0.25 kHz is assumed to be similar. The change in CPD for RH 20% to RH 80% was found to be around 60 mV. Thus, the energy dissipation was found to change slightly with RH (Fig. 2-8d). However, the charge density increased drastically. This suggests that the availability of H_3O^+ and OH^- plays an important role during triboelectric charging. Similar observations for PMMA and influence of RH on triboelectric charge generation have been reported⁶³. Also, most of the energy dissipation might not be getting utilized in triboelectric charge generation process.

2.4.6 Effect of tapping frequency:

The Taguchi method predicts that at RH of 20% and 50%, the generated triboelectric charge decreases with the increasing frequency (Fig. 2-2d). At RH 80%, the generated charge is independent of the tapping frequency. In contrast, the confirmation experiments at all RH suggest that the maximum charge was generated between 0.5 and 1 kHz (Fig.2-3d). The F-Ratio from ANOVA analysis (Table 2-5) for RH 20 and 50% also suggests that a tapping frequency has a significant influence on the produced triboelectric charge. The apparent discrepancy between Taguchi prediction and the confirmation experiments can be understood from the contribution of other factors. When compared to the bias and applied force, the contribution from tapping frequency is small. In fact, the contribution from bias is so significant that the effect of other factors can easily be masked.

The force vs time plot for different frequency is given in Fig. 2-9. It can clearly be seen that t_c between the tip and sample decreases as the tapping frequency increases and is calculated from F-t curve (as shown in Fig. 2-9a) for different scan frequencies. It should be noted that as the tapping frequency increases, for snap-in, the contact mechanics transition from DMT to Hertz model.

Due to the discrepancy between the Taguchi prediction and confirmation experiments, it is important to understand how significant is the observed trend in the confirmation experiment. Therefore, one-sided two samples T-test was performed for 0.5 kHz and 1 kHz against 0.25 kHz and is given in

Table 2-7. The p-value from the test suggests that there is a significant influence of t_c on the charge generation process. It is important to note that the observed trend was found to be independent of the relative humidity, the tip bias, or different tips (Fig. 2-10). The observed trend can be an indication of a peak around 100-250 μ s which could be due to the Debye relaxation peak (τ_{ice}) for ice (Fig. 2-10d)^{83,84}. The Debye relaxation peak presented in Fig. 2-10d is a simulated result. The presence of Debye peak has been proposed due to the recombination of H_3O^+ and OH^- ions which is a diffusion controlled process. This dielectric property of ice might explain the observed trend for t_c :

- $t_c < \tau_{ice}$: When t_c is less than τ_{ice} , the mobile ions do not have enough time to diffuse across the interface, which results in a lower surface charge density. Due to the difference in the diffusion coefficient of H_3O^+ and OH^- ions and presence of electric field, most of the mobile ions (present at the interface) might transfer across the interface. As t_c approaches τ_{ice} , the separation of ions is maximum and, thereby, the number of the generated charge increases.
- $t_c > \tau_{ice}$: When t_c is greater than τ_{ice} , the electric field due to CPD is shielded by the diffusion of ions. Once the electric field is shielded, counter ions can start to diffuse in the opposite direction and the probability of recombination rate increases. Hence, when t_c increases, the amount of the generated charge decreases.

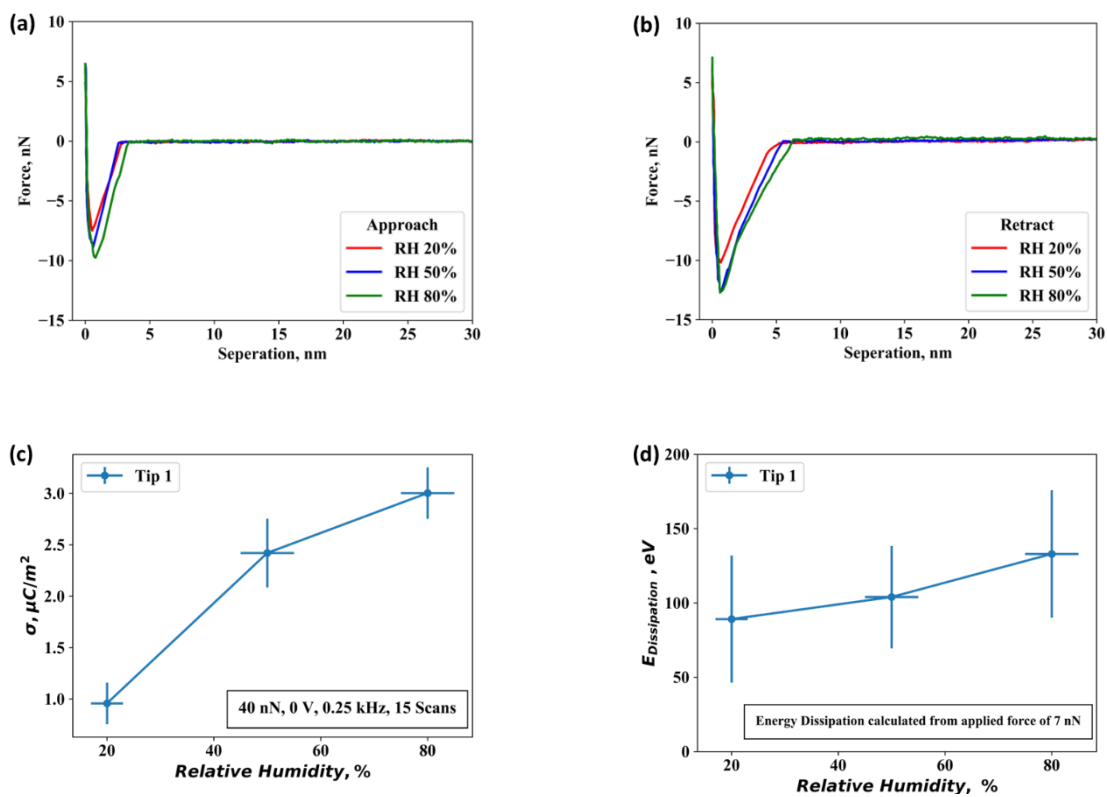


Fig. 2-8: Comparison of (a) F-Z approach, (b) retract curve for Tip 1 at different relative humidity. (c) Amount of surface charge generated as a function of relative humidity and (d) energy dissipation as a function of RH, calculated from the applied force of 7 nN.

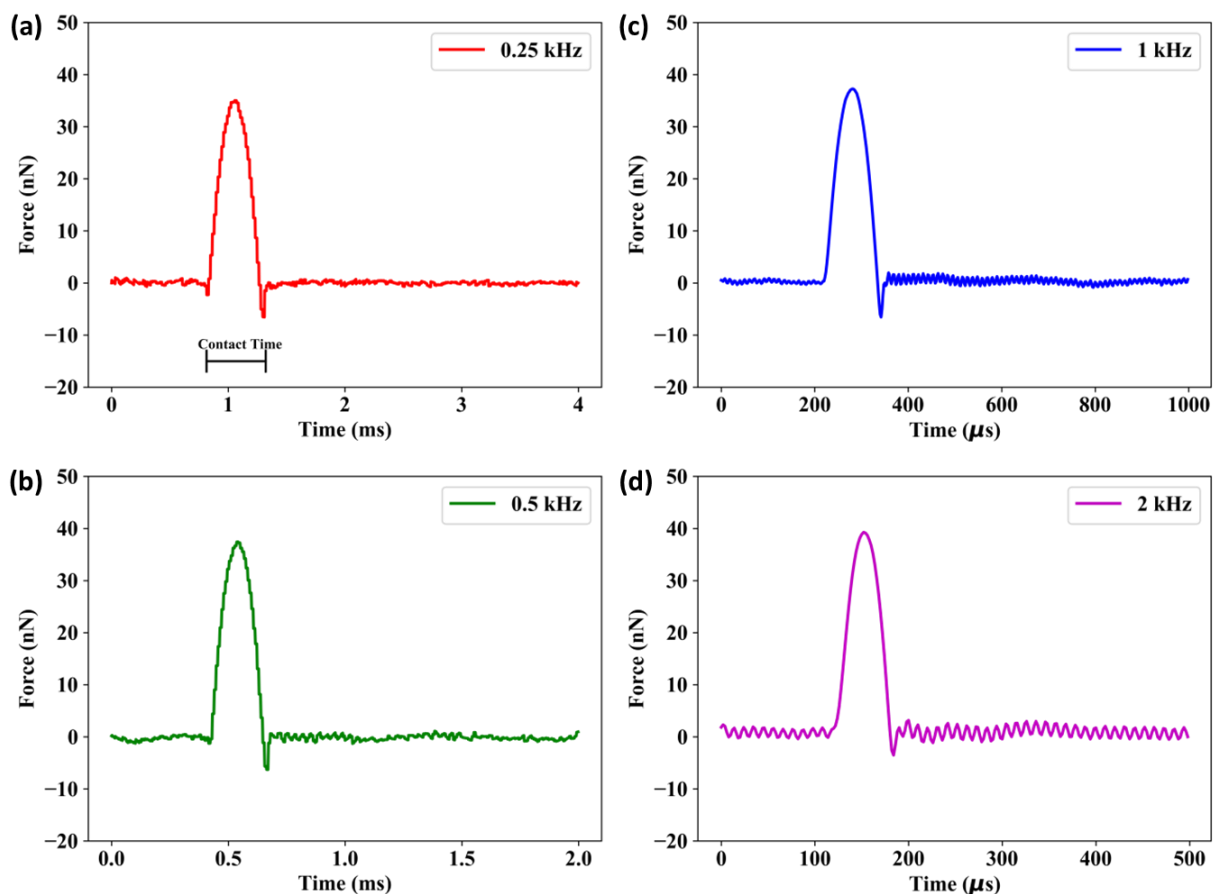


Fig. 2-9: Variation of contact time with different tapping frequency (a) 0.25 kHz, (b) 0.5 kHz, (c) 1 kHz, and (d) 2 kHz.

Table 2-7: T-test to compare the significance level of surface potential generated at tapping frequency of 0.5 kHz and 1 kHz with 0.25 kHz.

Tip	Applied Force (nN)	Bias (V)	# of Scans	RH %	0.5 kHz		1 kHz	
					DOF	p-value	DOF	p-value
Tip 1	40	0	15	50	2	0.12	2	0.17
Tip 1	40	1	15	50	2	0.03	2	0.04
Tip 1	40	0	15	80	4	0.02	4	0.01
Tip 2	40	0	15	80	2	0.18	2	0.15

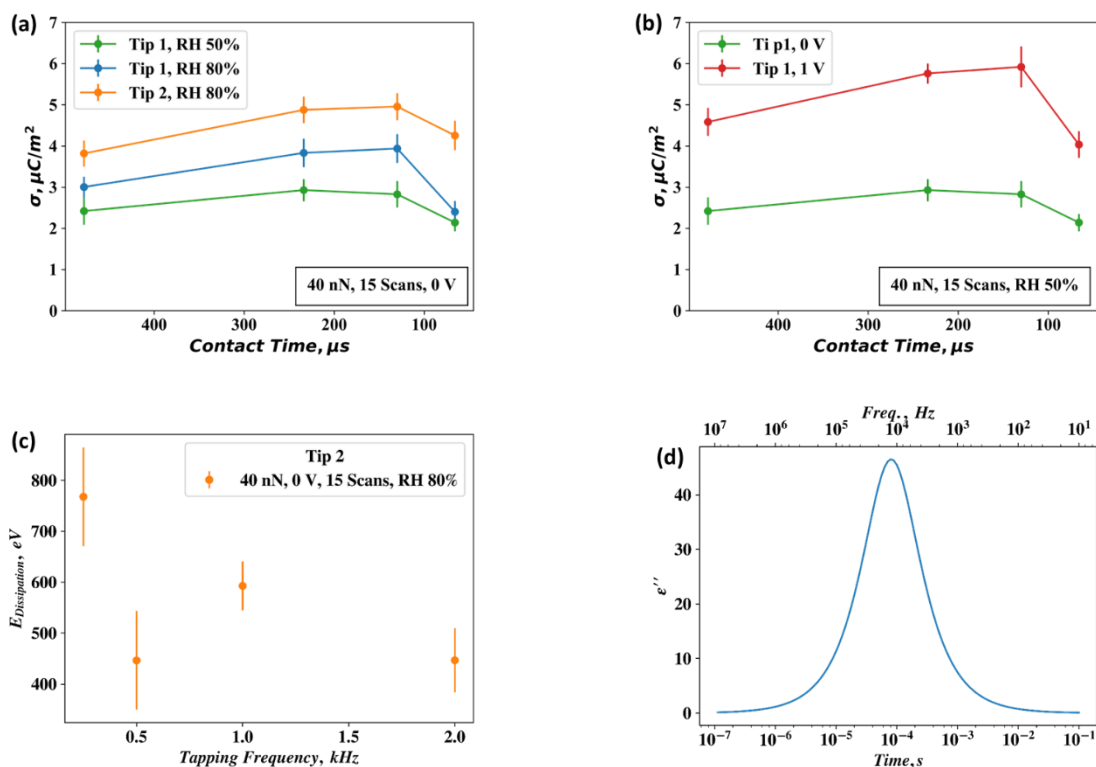


Fig. 2-10: Comparison of the triboelectric surface charge density at different contact times (a) at different relative humidity and tips, (b) for different applied bias at RH 50%. (c) Comparison of the energy dissipated at each contact for different tapping frequency, (d) Simulated Debye relaxation of ice. The parameters for the simulations were obtained from von Hippel⁸⁴ and reconsidered by Artemov et al⁸³.

From Fig. 2-10c, it can be seen that, except for 0.25 kHz, the dissipated energy for different scan frequencies does not change significantly. This suggests that no energy has been dissipated in the generation of the H_3O^+ and OH^- ions. It is well known that the hydrogen and hydroxide recombination is an exothermic reaction. Therefore, apart from recombination of charges, there are other processes which might get activated with a higher contact time.

It should be noted that the atmospheric discharge processes are being neglected in the present study^{9,10}. This is because the decrease in the surface potential does not seem to occur due to the

dielectric breakdown. This is due to the fact that when the bias is applied, the much higher surface potential was generated. This suggests that the dielectric breakdown may not be involved in the present case.

2.4.7 Effect of Tip Material:

All the results discussed above were obtained between PMMA and Si tip. As discussed earlier, the amount of the generated triboelectric charges depends on the position of two materials as determined from the triboelectric series. Therefore, we changed the tip material to a Pt-coated tip instead of Si tips. The first set of experiments was performed by keeping the applied force and relative humidity constant. For this set of experiments, EFM was used to measure the amount of the produced charges. The variable parameters were a number of scans and tapping frequency. It was observed that the triboelectric charge produced an increase in both the number of scans and tapping frequency (Fig. 2-11a). Based on these results, another study was performed in which the total number of contacts between the tip and sample was kept constant but the force was varied. It was observed that as the force increased, the amount of the produced charge also increased but no specific trend was observed in terms of the effect of tapping frequency (Fig. 2-11b). These results suggested that, although one factor at a time (OFAT) might set a particular trend, the overall conclusion might not reflect the true picture.

To get a better insight into how the triboelectric charges are influenced by different factors, Taguchi Design was once again used for these experiments. For this set of experiments, bias was not considered as a variable parameter and all the scans were performed at a ground potential of the tip. The parameters used for this study are given in Table 2-8. All the experiments were repeated three times. Therefore, for $\alpha = 0.05$, F-ratio was determined to be 3.55 and from the ANOVA analysis (Table 2-9), only the force was found to be the significant factor with a very high error.

The F-Z curve analysis suggested that the tip behavior changed during the study, indicating that the AFM tip material could be one of the reasons for such a high variability. SEM of one of the tips used for the scanning was done (Fig. 2-11d). A clear bluntness of the tip was observed due to continuous scanning. Also, a lot of foreign material (PMMA) can be seen to have deposited on the tip. All these observations contribute to the observed increased variability in the experimental observations. Therefore, using the Pt-coated tip for triboelectric charging experiment might

introduce an unknown variability. Changing the tip radius can also cause variability in the produced charge. Another reason for the variability could be the material transfer. As already discussed, the material transfer can reverse the polarity of the generated charge and introduces lots of variabilities.

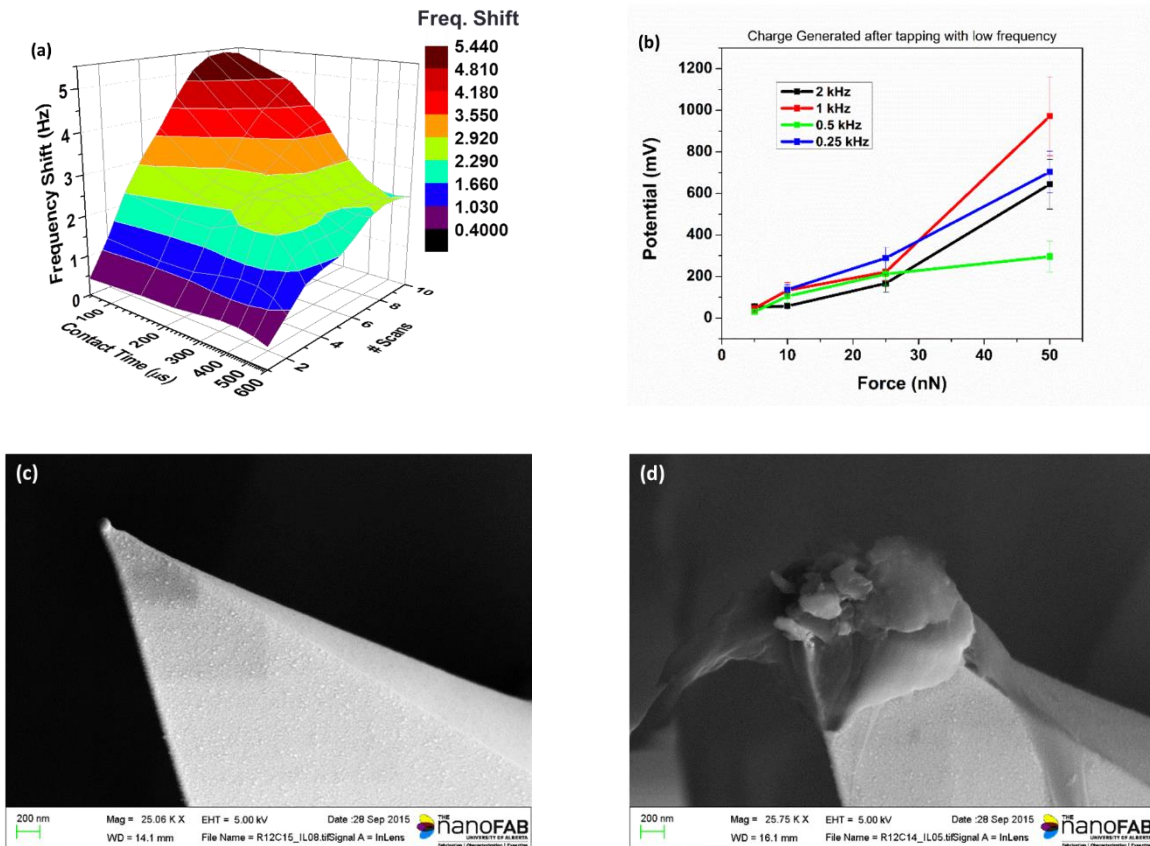


Fig. 2-11: (a) EFM study of triboelectric charge generated from the Pt-coated tip, applied force, in this case, was 1nN and cantilever resonance frequency was 147 kHz, (b) KPFM study done with Pt-coated tip, the resonance frequency of cantilever was 70 kHz. Both readings were taken at RH 13-20%. SEM images of (c) unused Pt-coated AFM tip and (d) AFM tip after imaging.

Table 2-8: Control factors and their levels for Taguchi Design using a Pt-coated tip.

Control Factors	Levels
Number of Scans (#)	5, 10, 15
Tapping Frequency (kHz)	0.25, 1, 2
Applied Force (nN)	5, 15, 30
RH (%)	20, 50, 80

Table 2-9: ANOVA analysis of the generated triboelectric charge using a Pt-coated tip.

Factors	DOF	F-ratio	% Contribution
# of Scans	2	1.43	6.47
Scan Freq. (kHz)	2	0.57	2.57
Applied Force (nN)	2	10.21	46.04
RH (%)	2	0.96	4.33
Error	18		40.59

2.5 Conclusion:

We conducted a detailed study of a triboelectric charge generation process. Based on the literature, we realized that the process has electrical, mechanical, and chemical aspects. Therefore, we used Taguchi analysis to choose the following factors – bias for electrical, force for mechanical, relative humidity for chemical –for experimental design to study all of them simultaneously and systematically. Although the percentage contribution of relative humidity could not be established, it is clear from the above discussion that all these factors had a significant influence on the produced triboelectric charge. It was observed that the tip bias had a significant influence compared to the applied force. The CPD changed with the relative humidity, suggesting the increase in ions was due to an increase in interfacial water. The applied stress was significantly greater than the flexural strength of PMMA; therefore, most of the produced charges could have occurred due to the plastic deformation of the substrate. It was also noted that the energy dissipation due to plastic deformation and the generated charge correlated linearly. The SEM image shows PMMA was attached on the AFM tip but, according to the error in the ANOVA

analysis and the number of contacts, the role of material transfer in the charge generation can be easily neglected. An important finding from these experiments was that the amount of the produced charge depends on the t_c . The observed trend in t_c was found to correlate with dielectric relaxation time constant (τ_{ice}) of ice due to diffusion controlled recombination rate of H_3O^+ and OH^- ions. Therefore, a general scheme for triboelectric charge generation is given in Table 2-10.

Table 2-10: Scheme for a triboelectric charge generation process^{9,10,34-36,53}.

Charge generation (rate controlling factor).	$R-R \rightarrow R^+ + R^- + R\cdot$	The reaction dependent on the applied force and in case of functional groups might also depend on the electric field. These reactions are generally endothermic.
	$H_2O \rightarrow H_3O^+ + OH^- + H\cdot + OH\cdot$	A small amount already present due to self-ionization of a water molecule. But also can be generated by applying electric field or force. The generation process is endothermic.
Charge stabilization ^{35,36} (will be partially discussed in Chapter 5).	$R^+ + R\cdot \rightarrow R-R^+$ $R^- + R\cdot \rightarrow R-R^-$ $R^+ + H\cdot \rightarrow RH^+$ $R^- + H\cdot \rightarrow RH^-$ $R^+ + OH\cdot \rightarrow ROH^+$ $R^- + OH\cdot \rightarrow ROH^-$	These processes could be endothermic or exothermic and are generally influenced by the electric field.
Charge recombination	$R^+ + R^- \rightarrow R-R$ $R^+ + R^- \rightarrow R\cdot + R\cdot$ $R^+ + OH^- \rightarrow ROH$ $R^- + H_3O^+ \rightarrow RH + H_2O$ $H_3O^+ + OH^- \rightarrow H_2O$	These processes are usually exothermic and can be influenced by the electric field.

It should be noted that most of the discussion in the present chapter is based on charge generation and recombination. The role of charge stabilization will be discussed in Chapter 5.

An important aspect that has not been highlighted from Table 2-10 is the interaction between the tip and substrate. It is quite clear that the tip geometry plays an important role in the triboelectric charge generation and the tip material can also influence the charge generation. From the studies done on Pt-coated AFM tip, it is clear that the changing tip radius and material transfer could easily influence the type and amount of the generated triboelectric charge. The implementation of Taguchi Design helped in identifying all these factors and reduce uncertainties which can influence the triboelectric charge generation process.

3 Role of Interfacial Water during Triboelectric Charging

3.1 Introduction

It is well established that relative humidity affects triboelectric charging^{9,10,42,53,63,85}. There are several factors associated with relative humidity that affects triboelectric charging. Some of these factors have been pointed out and discussed in Chapter 2. With an increasing relative humidity, the amount of interfacial water on the surface also increases¹⁰. Water being a dipolar molecule will interact with surface charges if they are present. It has been reported that the contact angle decreases during electro-wetting of the surfaces^{86,87}. Therefore, during triboelectric charging, an accumulation of water molecules near the charged area can also be expected and manipulated by relative humidity. The understanding of water accumulation at the charged interface will not only help in engineering the materials for better TENG performance but can also provide insight into surface chemistry, which can be used for sensing and other purposes^{68,88-92}.

In the present study, AFM and related techniques, such as tapping mode, EFM, KPFM etc. have been used for studying the role of interfacial water during triboelectric charging. There are several reports on interfacial water⁹³⁻⁹⁸ imaging and some of these reports are based on either direct imaging of the surface⁹⁶ or indirect technique, such as electrical, mechanical, etc. For the water surface imaging, one of the key issues is the interaction of the tip with the sample results in the perturbation of the water layer. Hence, dynamic mode AFM is preferred for imaging the water layer which is based on a different type of the tip interaction (attractive or repulsive), and may or may not make contact with the substrate. Santos et. al⁹⁶, have shown that the true height of the water can be significantly different and the exact determination of the water height could be challenging⁹⁹. It depends on whether water molecules are present at the interfaces and the type of substrate (hydrophilic and hydrophobic substrate). Another approach to image the interfacial water is based on a cantilever phase shift during approach and retract from the sample surface^{100,101}. The AFM tip interacts differently in the presence or absence of interfacial water. This interaction can also differ depending upon the amount of interfacial water present on the surface and the number of asperities on the tip¹⁰¹.

It should be noted that most of these reports are based on a crystalline atomically smooth substrate such as mica, BaF₂. But spin-coated samples typically have a roughness of around 0.5-1 nm that is significantly greater than the diameter of a water molecule (2.75 Å). Hence, direct imaging of the surface may not reveal the presence of interfacial water on the amorphous substrate but the phase imaging might reveal the presence of interfacial water¹⁰². Phase imaging has been used to differentiate between the hydrophilic and hydrophobic nature of polymers^{103,104}. Apart from the nature of the substrate, phase shift can arise due to other materials' property, such as elastic modulus, viscoelasticity, etc.^{105,106}, leading to a challenging interpretation of phase imaging.

The indirect methods are based on either studying electrical properties (such as Scanning Polarization Force Microscopy^{98,107,108}) or viscoelastic property (acoustic AFM¹⁰⁹ technique) or encapsulating the water molecule on the surface (coating the surface with graphene⁹⁷), etc. For this study, the characterization of electrical properties of the material using AFM was the most suitable technique. Since water is a dipolar molecule, the polarization properties of water have been used to image the presence of interfacial water on an insulating surface^{107,108}. It has been demonstrated that the capacitive force is parabolic with respect to the tip bias and depending upon the dielectric permittivity (ϵ) of the substrate, the curvature of parabola changes¹¹⁰. The determination of the dielectric constant of thin¹¹¹ and thick¹¹² dielectric materials have been reported. In fact, a frequency dependent nano-scale dielectric spectroscopy has been recently proposed¹¹³. One of the assumptions in this technique is that there is no surface charge present and is illustrated through symmetric parabolic peak for the force measured against the tip bias¹¹⁰. In the present study, however, triboelectric charges are generated and, as a result, the parabola might be asymmetric. Therefore, the model used in the above study needs to be modified so as to take into account the presence of surface charges. There have been several studies conducted to understand the presence of surface charges but the suggested model does not consider the change in the dielectric property of the substrate^{114,115}. The dielectric constant of water ($\epsilon_{Water} = 4 - 80$, depending upon the thickness of interfacial water¹¹⁶) can be significantly different from the dielectric property of the substrate ($\epsilon_{PMMA} = 2.6^{74}$). Therefore, determination of dielectric properties might indicate change in the amount of interfacial water. This can easily be understood by considering a parallel plate capacitor between the tip and the substrate. The overall electrical connection between the tip and the substrate can be put together as 3 capacitors in series. Hence, the equivalent capacitance between the tip and the substrate is given as:

$$\frac{1}{C}(z_0) = \frac{1}{C_{PMMA}} + \frac{1}{C_{IW}} + \frac{1}{C_{Air}}(z_0) \quad \text{Eq. 3-1}$$

where C_{PMMA} is capacitance of PMMA substrate, C_{IW} is due to interfacial water and C_{Air} is due to the air. The capacitance is given as $C = \frac{\epsilon_0 \epsilon_r A}{d}$. z_0 is the lift height of the cantilever. Therefore, if the amount of interfacial water between charged and uncharged region is different, C_{IW} due to interfacial water will be different and can be identified by determining the dielectric properties between the two regions.

To understand the role of interfacial water during triboelectric charge generation, we conducted EFM (Electrostatic Force Microscopy) and tapping mode experiments.

3.2 Experimental Detail

For the present study, Pt/Ti coated Si tip was used. The details of the Pt coating, PMMA substrate, experimental setup, charging process, EFM, KPFM study, and analysis etc. have already been discussed in the experimental section of Chapter 2. The experiments were conducted at RH 80, 50 and 20% in descending order. The charges were created from the parameters given in Table 3-1.

During the tapping mode study, amplitude(A_0), amplitude set-point(A_{sp}), frequency (f) etc. were changed. The details of tapping mode imaging will be discussed later. In order to preserve the tip conditions, only few experiments were conducted at RH 80 and 50% but the tip condition still changed during the experiment, as noted in Chapter 2. A detailed study was done only at RH 20%. At RH 20%, the phase shift for the low phase area was between -75° to -50° and -20° to 10° for the high phase area. The definitions of the high and low phases will be discussed in Section 3.4.2. The peak force was calculated applying VEDA tool¹¹⁷, using the mechanical property of tip and substrate as given in Chapter 2. The adhesion force (F_{AD}) from F-Z curve was determined to be 25.3 nN and the tip radius (R_{eff}) was assumed to be 100 nm. Q was determined to be 325 and k to be 6.64 N/m.

Table 3-1: Parameters used for generating triboelectric charges to study the role of interfacial water:

Factor	Value
Applied Force	5 nN
Applied Bias	0 V
Tapping Frequency	0.5 kHz
# Scans	5
Scan Length	10 μm
Aspect Ratio	4
Scan Rate	0.25 Hz

3.3 EFM study of Triboelectric charges

3.3.1 Theory

To understand the role of interfacial water, we conducted electrostatic force microscopy (EFM) studies. EFM is an electrical characterization technique and is based on the electrostatic force gradient between the tip and the sample. When a tip oscillates at a distance of z from the surface, an electrostatic force $F_{elec}(z)$ acts on the tip, which can be described by first order approximation as¹¹⁸:

$$F_{elec}(z) = F_{elec}(z_0) + \frac{\partial F(z_0)}{\partial z} \cdot (z - z_0) \quad \text{Eq. 3-2}$$

where z is the instantaneous position of the cantilever and z_0 is the equilibrium position of the cantilever. Due to the oscillation of AFM tip, $\frac{\partial F(z_0)}{\partial z}$ acts like a force gradient on the tip, which is equivalent to the change in spring constant (Δk) of the tip. Therefore, to detect the force gradient acting on the tip, the tip is oscillated near its resonance frequency. As the spring constant, k ,

changes, the resonance frequency of the cantilever also changes ($\frac{\Delta f}{f_0} \approx -\frac{\Delta k}{2k}$). Thus, electrostatic force gradient acting on the cantilever can be expressed as:

$$\frac{\Delta f}{f_0} = -\frac{1}{2k} \frac{\partial F_{elec}}{\partial z}(z_0) \quad \text{Eq. 3-3}$$

where Δf = change in the frequency of the cantilever,

f_0 = the resonance frequency of the cantilever,

The electrostatic force between the tip and substrate is given as^{114,115}:

$$F_{elec} = \frac{1}{2} \frac{\partial C}{\partial z} (V_{tip} - V_S)^2 + E_S q_{tip} \quad \text{Eq. 3-4}$$

where C is capacitance between tip and substrate, V_{tip} is the tip bias applied during EFM imaging, V_S is the substrate potential. E_S is the electric field between the tip and the substrate that arises due to the presence of static charges and multipoles, q_{tip} is the effective charge on the cantilever tip and is given as $C(V_{tip} - V_S)$. If we assume that the distance between the tip and substrate is very small (~ 10 - 100 nm, which in case of EFM is partially true), then the electric field, due to static charges, can be modelled as $g_t \sigma_s / \epsilon_0$, where g_t is the geometric parameter due to tip geometry, σ_s is the surface charge density. Thus, electrostatic force acting on the cantilever at a given lift height is given as¹¹⁵:

$$\frac{\partial F_{elec}}{\partial z}(z_0) = \frac{1}{2} \frac{\partial^2 C}{\partial z^2} (V_{tip} - V_S)^2 + \frac{\partial C}{\partial z} \frac{\sigma_s}{\epsilon_0} g_t (V_{tip} - V_S) \quad \text{Eq. 3-5}$$

Comparing Eq. 3-3 and Eq. 3-5, we get:

$$\Delta f \propto \left(\frac{\partial^2 C}{\partial z^2} (V_{tip} - V_S)^2 + \frac{\partial C}{\partial z} \frac{\sigma_s}{\epsilon_0} g_t (V_{tip} - V_S) \right) \quad \text{Eq. 3-6}$$

From Eq. 3-6, it is clear that the change in the cantilever resonance frequency with respect to the applied tip bias will be parabolic and asymmetric as discussed above. In Eq. 3-6, it has been assumed that the reference plane is at a given z_0 . If the reference plane is assumed to be at infinity, then a constant term needs to be added to Eq. 3-6. It should be noted that the 1st part of the Eq. 3-6 is representative of the capacitance between the tip and substrate, and is equivalent to Poisson's equation. The 2nd part carries the information about the presence of surface charge, provided the capacitance gradient, $(\partial C / \partial z)$, is known.

3.3.2 EFM Results and Discussions

EFM experiments were conducted at different RH for different tip bias. Fig. 3-1a, shows the frequency shift for the triboelectric charge generated at RH 80% and tip bias at 0V. For the EFM measurements, charges were generated on the PMMA sample in the region which is $10\mu\text{m} \times 2.5\mu\text{m}$ (aspect ratio of 4), while the other parameters are given in Table 3-1. The charges generated in this region resulted in a higher frequency shift of the tip-cantilever and is the essence of the EFM. The histogram of the frequency shift, together with the Gaussian fitted peak, is shown in Fig. 3-1b. The peak around 63.4 Hz was found to be from the uncharged region. Similarly, the frequency shifts for different tip bias were determined. From Fig. 3-1a and b, it is clear that the EFM results were obtained for the reference plane at infinity. To change the reference plane from infinity to the lift height of 100 nm, the shift in frequency at $V_{tip} = V_S$ should be made equal to 0. Therefore, the substrate potential was determined by AM-KPFM imaging and is shown in Fig. 3-2d-f. The substrate potential for both the uncharged and charged regions were subtracted from the tip bias for the parabolic fitting that should be equivalent to Eq. 3-6. The constant part of the fitted equation was subtracted from both the experimental and fitted results to shift the reference plane at $z_0 = 100 \text{ nm}$. The obtained experimental result is shown in Fig. 3-1c. The fitted equation for the charged and uncharged region at different RH is now similar to Eq. 3-6. Therefore, the co-efficient of the fitted equation can be compared to Eq. 3-6 and the dielectric property and surface charge density on the substrate can be estimated.

From the coefficient of the linear component, the surface charge density can be determined, if $(\partial C/\partial z)$ is known. Ideally, the uncharged region should not have any linear component. However, due to the presence of interfacial water (OH^- ions), there might be a small amount of stray surface charges always present. Hence, a linear component with small slope for uncharged region was observed for all the three RH conditions. The slope of the charged region was found to be significantly greater than the uncharged region and by determining the angle between the linear component of the charged and uncharged region, the surface charge density can be estimated (Fig. 3-1d). From Fig. 3-1d, it is clear that the surface charge density generated for RH 50% is lower than RH 20 and 80% and is verified from Fig. 3-5b. Although we attempted to preserve the tip shape during the experiments, it was noted from the adhesion force that the tip radius changed during the scanning. Hence, an accurate estimation of $\partial C/\partial z$ cannot be done as C is a function of the tip radius, cone angle, and cone height. Since the frequency shift for charged and uncharged region has been acquired simultaneously, the change in the tip geometry for the given RH should not be considered

Since water is a dipolar molecule, the presence of charges might induce an electric field to the interfacial water molecule. Also, from Chapter 2, it was noted that if the tip geometry does not change significantly, the amount of triboelectric charge produced increases with the relative humidity. Hence, an increase in the amount of interfacial water can be expected in and around the charged region, which will change the effective capacitance between the two regions. Therefore, the comparison of the quadratic component of charged and uncharged region can provide evidence of the contribution of charges due to the amount of interfacial water between the two regions (Fig. 3-1e). Although a slight increase of $\partial^2 C/\partial z^2$ in the charged region compared to the uncharged region was observed, the error in estimating the coefficient is much bigger and, therefore, is statistically insignificant. At RH 50%, a decrease in $\partial^2 C/\partial z^2$ is observed suggesting that the tip radius might have changed between the experiments.

It should be noted that the amount of the present interfacial water might be 1 or 2 monolayers. From Eq. 3-1, it can be clearly seen that the presence or change in the amount of interfacial water between the charged and uncharged region may not contribute significantly to $\partial^2 C/\partial z^2$. The adhesion force between the tip and the substrate was also compared (data not shown) but no

significant difference was observed between the two regions. Hence, the change in interfacial water between the charged and uncharged region from EFM was found to be insignificant.

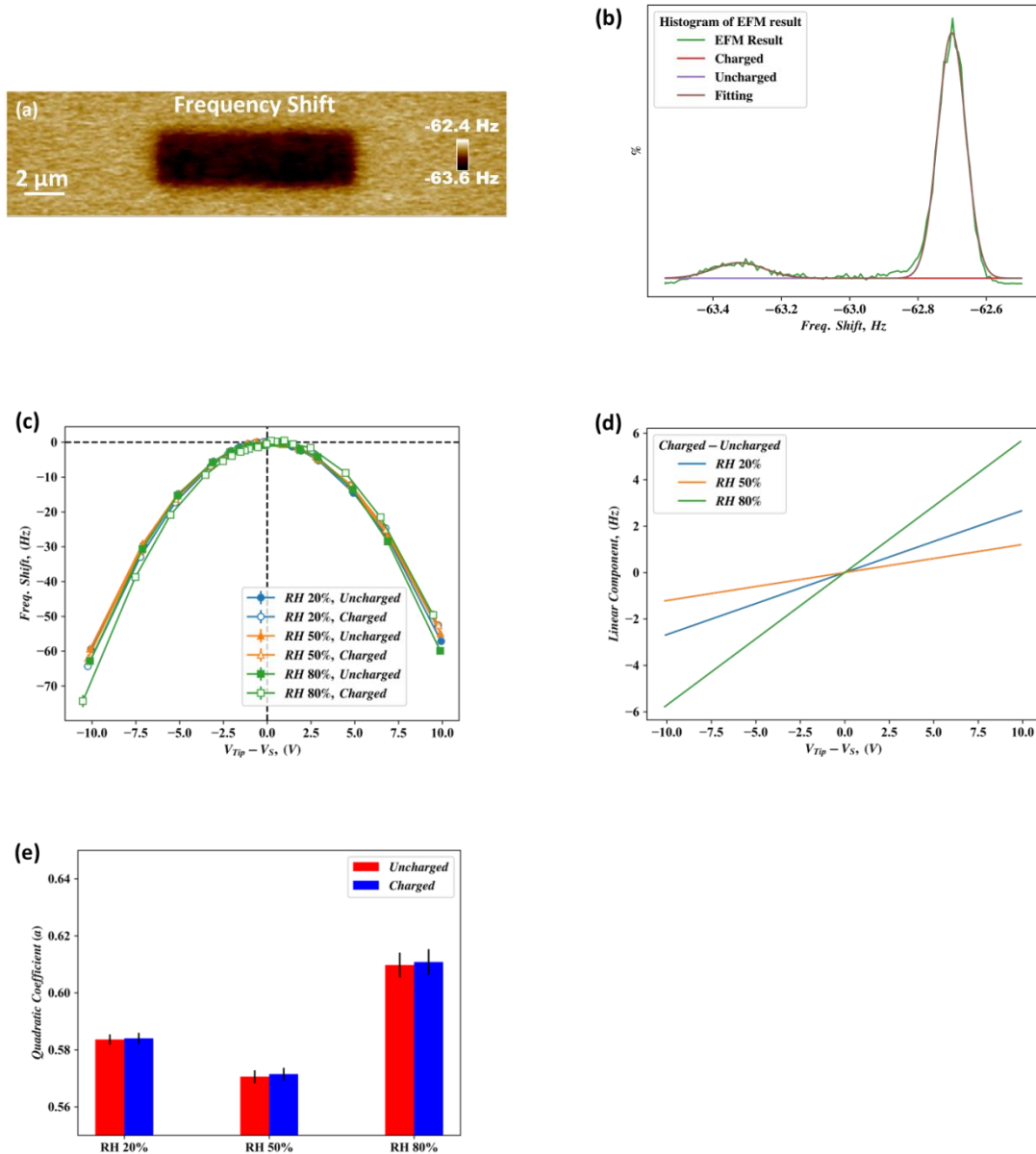


Fig. 3-1: (a) Frequency shift observed during the EFM study of the charged region at RH 80%, the dark brown region is the location where charges were generated (b). The histogram of the Frequency shift observed during EFM for (a) and Gaussian Fitting done for charged and uncharged region, (c) Frequency shift observed for the charged and uncharged region at different relative humidity wrt. to the potential difference between the tip and substrate. (d) The difference in the

linear component of the charged and the uncharged region determined from the curve fitting and
(e) The quadratic coefficient for different relative humidity at charged and uncharged region.

3.4 Phase Imaging Study of Interfacial Water

3.4.1 Theory of Tapping Mode Imaging and Evolution of Phase

In tapping mode imaging, the tip oscillates near its resonance frequency. As vibrating cantilever approaches the sample and due to the tip-sample interaction, the amplitude of the oscillation changes. The overall dynamics of the system can be written as¹⁰⁵:

$$m\ddot{z} + \frac{2\pi m f_0}{Q} \dot{z} + kz = F_{ts} + F_0 \cos 2\pi f t \quad \text{Eq. 3-7}$$

where m is the effective mass of the cantilever, z is the instantaneous position of the cantilever measured from the equilibrium position z_C of the cantilever, f is the drive frequency of the cantilever, F_0 is the drive force applied from the piezoelectric transducer, F_{ts} is the force between tip and sample, and is given as:

$$F_{ts} = F_{AD}(d) + F_{CAP}(d) + F_{DMT}(d) \quad \text{Eq. 3-8}$$

where, $F_{AD}(d)$ is the adhesion force given as^{101,105}:

$$\begin{aligned} F_{AD}(d) &= -\frac{HR_{eff}}{6d^2} & d > a_0 \\ &= -\frac{HR_{eff}}{6a_0^2} & d \leq a_0 \end{aligned} \quad \text{Eq. 3-9}$$

$F_{CAP}(d)$, is the capillary force between the tip and sample and when tip approach the sample $F_{CAP}(d)$, is given as⁷⁸:

$$F_{CAP} = 2\pi R_{eff}\gamma(\cos\theta_1 + \cos\theta_2) \quad \text{Eq. 3-10}$$

During retraction, the water layer may extend out with the tip making $F_{CAP}(d)$ function of d . This function has been expressed in several forms depending upon the type of interaction, the tip condition, relative humidity, etc. A general form of capillary force during retraction can be written as⁹⁹⁻¹⁰¹:

$$F_{CAP}(d) = 4\pi R_{eff}\gamma f(d) \quad d > a_0 \quad \text{Eq. 3-11}$$

and $F_{DMT}(d)$ is the repulsive force upon contact and is given as^{73,101}:

$$F_{DMT}(d) = \frac{4}{3}E^*\sqrt{R_{eff}\delta^3} \quad d \leq a_0 \quad \text{Eq. 3-12}$$

where d is the instantaneous tip-sample distance¹⁰⁵ ($= z + z_c$), a_0 is an intermolecular distance, H is Hamaker constant θ_1, θ_2 is the contact angle between the tip and substrate with water and other parameters that have already been defined in Chapter 2.

Now, substituting F_{ts} from Eq. 3-8 into Eq. 3-7 and solving for z gives the interaction of the tip with the sample and the force applied during the interaction. But from Eq. 3-9-Eq. 3-12, it is evident that Eq. 3-7 cannot be solved analytically. Although Eq. 3-7 have been solved numerically to determine the change in the amplitude and phase of the cantilever as the tip interacts with substrate (APD curve), these numerical solutions require a precise knowledge of $\gamma, f(d), \delta$ etc. that are not known in most cases. Also, it is important to understand the effect of applied force by tip on the substrate during the interaction. Unlike the F-Z curve, the APD curve cannot be interpreted directly i.e., in case of the tapping mode, the applied force cannot be calculated directly. Therefore, there are several solutions proposed to determine the applied peak force¹¹⁹⁻¹²². One of such solutions proposed for a DMT¹²¹ model is given in Eq. 3-13 below:

$$F_{peak}^{rep} \approx 2^{1/8} 3^{-1/4} \pi^{3/4} \left(E^* \sqrt{R_{eff}} \right)^{1/4} \left(\frac{k}{Q} \right)^{3/4} A_0^{9/8} A_{ratio}^{9/8} \times \{(-1 + \Omega^2)Q + \sqrt{\frac{1}{A_{ratio}^2} [\Omega^2 + (1 - \Omega^2)^2 Q^2] - \Omega^2}\}^{3/4} - F_{AD}/2 \quad \text{Eq. 3-13}$$

Here, A_{ratio} is the ratio of A_{sp} with A_0 , Ω is the ratio of drive frequency with resonance frequency (f_0) of the cantilever.

From Eq. 3-13, it is clear that during Tapping mode imaging, applied force can be varied by varying A_0 , A_{ratio} and f . The rest of the parameters do not change during the imaging, except R_{eff} . The change in R_{eff} is hard to determine during imaging and efforts are generally made to keep it constant.

Apart from this, it has been reported that the phase shift of the cantilever can be used to estimate the substrate properties. The force-based and energy-based methods have been used to estimate the properties of the sample. The force-based model is based on Newtonian mechanics and was found to be valid for only certain conditions. To overcome these shortcomings, Cleveland et al. proposed an energy-based model¹²³ and have shown that the dissipated energy is related to the sine of the phase angle and is given as^{105,124}:

$$\sin\phi = \frac{f}{f_0} \frac{A(f)}{A_0} + \frac{Q \langle E_{dis} \rangle}{\pi k A_0 A(f)} \quad \text{Eq. 3-14}$$

where $A(f)$ is the amplitude when the cantilever is driven at f , ϕ is the phase shift of the cantilever w.r.t to the transducer, $\langle E_{dis} \rangle$ is the energy dissipated due to inelastic scattering from tip-sample interaction per cycle. The first part of Eq. 3-14 is related to the losses from viscous damping of the oscillator in the medium and second part to the tip-sample interaction¹²³. In Eq. 3-14, every term can be experimentally determined and by determining the average dissipated energy, the sample property can be easily identified. It is interesting to note that $\langle E_{dis} \rangle$ is dependent on $\sin\phi$ which is symmetric at 90° . Therefore, the attractive regime (AR) or repulsive regime (RR) will not affect the power dissipated during the interaction. The AR and RR in tapping mode AFM will be

discussed in detail in Section 3.4.3. It should also be noted that Eq. 3-14, does not specify where the power is getting dissipated, however, the power dissipated due to tip sample interaction has been shown to be related to materials property such as surface energy (γ), viscoelastic co-efficient (η), adhesion hysteresis, etc.^{100,124–127}. Apart from this, it has been reported that the topography and slope of the sample can also influence the phase imaging. Hence, determining the materials property from phase imaging can still be challenging. Therefore, often numerical simulations are used to estimate various properties from phase imaging¹²⁴ or force based model is employed if the assumptions are satisfied for the specific cases¹²⁸.

3.4.2 Phase Imaging Studies

During tapping mode imaging, it was noticed that at high amplitude (A_0), phase difference ($\Delta\phi$) between charged region and uncharged region were significant. The result of tapping mode imaging is seen in Fig. 3-2. From the topographic images (Fig. 3-2a-c), it is clear that there was no observable material transfer during the charge generation process. The KPFM images (Fig. 3-2d-f) indicate where the charges and the potential of the charges were created. It should be noted that positive surface charges were produced at all relative humidity. At low amplitude, i.e., $A_0 = 22 \text{ nm}$ (Fig. 3-2g-i), there was no significant change in the phase between the charged and uncharged region. With increase in amplitude ($A_0 = 110 \text{ nm}$) (Fig. 3-2j-l), a drastic change in the phase was observed between charged and uncharged region. It should be pointed out that the maximum amplitude range for the Lock-In during tapping mode imaging was kept at 2 V. Hence, considering the cantilever sensitivity, the maximum amplitude (A_0) that could be set was 110 nm. It should also be noted that the scale bar for Fig. 3-2a-i is 2 μm , whereas for Fig. 3-2j-l, it is 4 μm . From Fig. 3-2d-f and j-l, we noticed that the area covered by a higher phase is different from the area covered by the surface potential. Therefore, the region where the phase shift was near 0° was referred to as a High Phase (HP) region and the other region as a Low Phase (LP) region.

The phase contrast at RH 20 and 50% was quite significant and the coverage area of HP for RH 50% was more than that of RH 20%. At RH 80%, only a slight change in phase contrast was observed. As already discussed, the phase shift between the hydrophilic and the hydrophobic region could be different^{103,104}. Since the substrate is PMMA, the observed phase difference was hypothesized to be due to the change in the amount of interfacial water between the two regions. As mentioned earlier, the amount of interfacial water increases with the increasing RH. It has been

reported that up to RH 40%, the time required for a capillary bridge to form is around few milliseconds¹²⁹ and decreases with the increasing RH^{100,130}. Since the imaging was performed near the resonance frequency of the cantilever ($f_0 = 93.17 \text{ kHz}$), the contact time would be in the range of few micro-seconds. Also, it has been shown that with the increasing RH, the critical amplitude (A_C) required for transitioning from AR to RR increases^{99,131}. The change in A_C depends on the wetting property of tip and substrate and the capillary bridge formation. Therefore, the observed phase contrast at RH 20 and 50% could be due to increased interfacial water around the charged region. Also, AR to RR transition dependent on RH might result in lower A_C . Tip condition will also influence A_C ¹⁰¹. However at RH 80%, the A_C might have increased significantly due to the formation of capillary bridge. This indicates that the dynamics of the cantilever might have changed with the increasing RH and could result in some commonly known artifacts. Hence, it is necessary to verify whether the observed phase contrast is due to some commonly known artifacts.

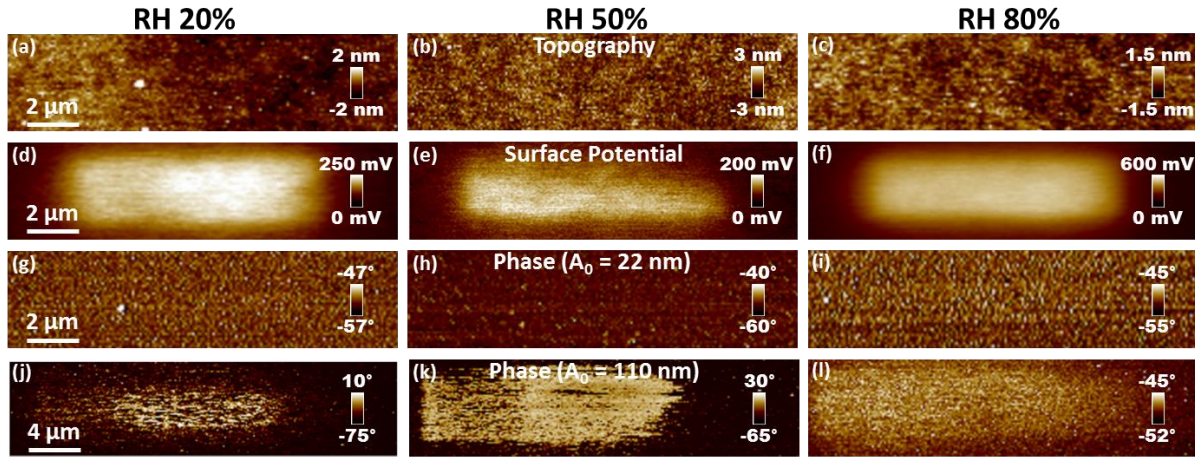


Fig. 3-2: (a)-(c) Topography of the area where charges were generated for different relative humidity, (d)-(f) Respective surface potential of the same area for the given RH's, (g)-(i) phase shift observed during tapping mode at an drive amplitude of 22 nm and amplitude setpoint of 14 nm, (j)-(l) phase shift observed during tapping mode imaging for drive amplitude of 110 nm and amplitude setpoint of 60 nm.

3.4.3 Checking for Artifacts

One of the reasons for the origin of the artifact is scanning the surface at small A_0 ¹³². When the amplitude of the AFM tip is small, the tip might scan the surface in AR. At small A_0 and in the presence of the surface charges, the attractive force between conducting tip and the sample will increase. While imaging over the charged region, the tip will retract to maintain the amplitude at a setpoint A_{sp} . This could lead to an artifact which can be easily observed in the topography. This effect is enhanced if the spring constant of the cantilever is small or even by applying a tip bias, as shown in Fig. 3-3. In this case A_0 was ~ 22 nm and RH was 50%. It is clear from KPFM image (Fig. 3-2d-f), that the produced surface charge was positive. Hence, when a negative bias was applied to the tip, the attractive force between the tip and sample increased. Due to an increased attractive force, Z-piezo moved away from the sample to maintain A_{sp} and an increase in height was observed in Fig. 3-3a. Similarly, when the positive bias was applied to the tip, the repulsive force increased, which results in the tip moving closer to the substrate and the height decreased (Fig. 3-3c). Although an artifact in topography was observed, the observed phase shift in phase image between biased (Fig. 3-3b, f) and ground (Fig. 3-3d) was found to be around only 8° . Also, the change in the phase contrast between charged and uncharged regions were found to be between $1^\circ - 2.5^\circ$, which could be due to an increased attractive or repulsive force. However, $\Delta\phi$ at high A_0 (Fig. 3-2j-l) was around 60° , indicating the observed phase contrast might not have occurred due to the increased attractive or repulsive force from the surface charge.

Another possibility for the observed phase contrast may not be due to the Tapping Mode but could be due to the change in the properties of PMMA between charged and uncharged regions. As noted in Chapter 2, the applied compressive stress can be significantly higher than the flexural strength of the PMMA. Therefore, the observed phase contrast may result from the failure of PMMA at the charged region. Since the applied force at all 3 RH was the same, the stress should be nearly the same. However, from Fig. 3-2 j,k, it was noted that the phase contrast distribution was different between RH 20% and 50%. Also, the increased coverage area of HP compared to the surface charge generated area (Fig. 3-2d, j, and e, k) cannot be explained by the failure in PMMA during charge generation process. Hence, the observed phase contrast might not have occurred due to the failure of PMMA.

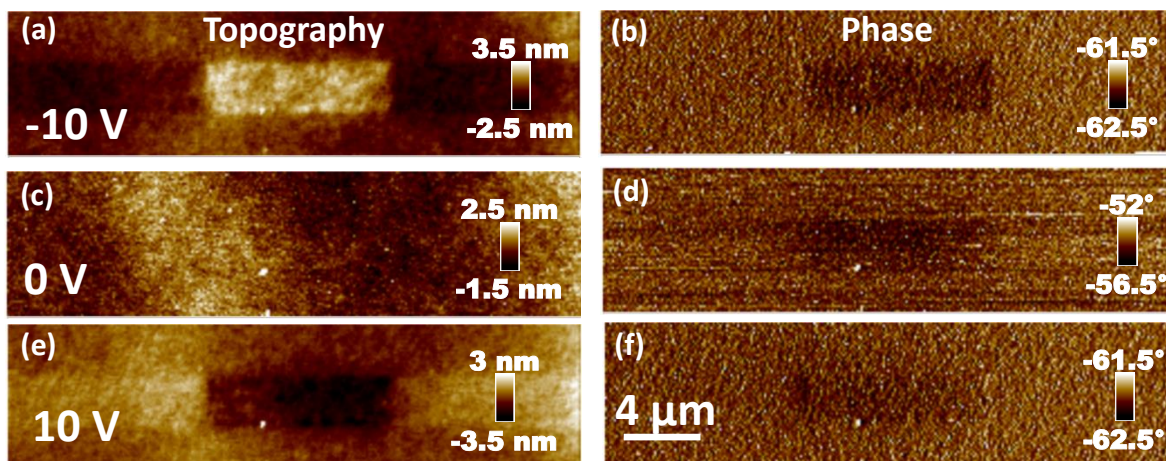


Fig. 3-3: Artifact which can be observed during tapping mode imaging. (a), (b) is the tapping mode image with a tip bias of -10 V, (c),(d) for 0V and (e), (f) for 10V. The artifact in the topography can be easily identified, whereas in the phase the shift between charged and uncharged region is not significant.

3.4.4 Amplitude Phase Displacement analysis

Another reason for the artifact may be the selection of A_{sp} in the bi-stable region^{105,133}, which could arise due to transition from AR to RR. This could be the most probable reason for the observed phase contrast in Fig. 3-2j-l. The origin of this artifact can be identified from the Amplitude-Phase-Displacement (APD) curve. Before discussing APD curve, it is important to clarify the phase conventions, as they might vary from one study to another. For Nanoscope V controller, during Tapping mode imaging the phase shift of $<0^\circ$ means the cantilever is in AR, whereas $>0^\circ$ means RR¹³⁴. All the phase images in this study follow this convention. However, for the APD curve and $\langle E_{dis} \rangle$ calculation, the followed phase convention was given by Garcia et al¹³⁵ i.e., when the tip is in AR, the phase lag increases ($>90^\circ$), while in RR the phase lag decreases ($<90^\circ$).

When the tip approaches the substrate, there are long-range attractive forces acting on the tip. This causes the resonance frequency of the cantilever to decrease while the amplitude and the phase of the cantilever change accordingly. As the tip makes contact with the substrate, the repulsive forces

start to act and cause the resonance frequency to increase. During the transition from AR to RR, a jump in the amplitude and phase shift of the cantilever can be observed^{105,135}. The jump in amplitude causes two dynamic equilibrium states to co-exist. These two states are referred to as bi-stable states (attractive or repulsive state). If a bi-stable state exists, for a certain A_{sp} , a jump in phase imaging can also be observed and a contrast similar to Fig. 3-2j-1 can be expected. During imaging, APD curves were obtained for HP and LP at RH 20%, Fig. 3-4a, d show the amplitude and phase vs frequency of the cantilever at RH 20%. The drive frequency at which APD curves were obtained is also shown. The amplitude vs Z-piezo displacement for the approach and retract at HP and LP were found to be nearly similar (Fig. 3-4b, c). It should be noted that the cantilever was driven at an amplitude of ~ 96 nm, whereas A_{sp} was kept at 8 nm. This was done to prevent the tip from getting trapped in the surface. It was observed from the previous experiments where A_{sp} was kept low, the tip damaged the sample and got contaminated. It is clearly seen from Fig. 3-4e-f, that the phase shift increases as the tip approaches the sample, indicating that the imaging was done predominantly in the AR. The phase shift vs Z-piezo displacement, during approach, clearly shows $\Delta\phi$ of 34.2° between HP and LP region (Fig. 3-4e) indicating the presence of a bi-stable state which was not observed in amplitude vs Z curve. But during retraction, the phase difference, $\Delta\phi$ at the same Z-position was found to be 2.4° (Fig. 3-4f), making evident the presence of hysteresis between the approach and retract for HP. The hysteresis between the approach and retract in phase has been predicted during the capillary bridge formation and rupture¹⁰¹. But there are few key differences between the present observation and the reported observation by Barcons et al.¹⁰¹ Their prediction and study suggested that the formation of a capillary bridge and its rupture happens when the AFM tip is close to the substrate. Thus, at a low Z-piezo displacement, a hysteresis in the APD curve was expected. From Fig. 3-4 we observed hysteresis at a higher Z-piezo displacement. In Chapter 2, it has been shown that the tip became blunt due to repeated imaging. We argued that when the tip is blunt, multiple asperities can occur and, hence, several capillary necks can form, which can drastically change the APD curve. Second reported observation for the blunt tip is that the hysteresis originates from the trapping of the tip during retraction. The phase shift vs Z curve suggests, however, that the tip might have been trapped during the approach itself. It has been pointed out that, depending upon the number and geometry of asperities, the behavior of APD curve can significantly change. Therefore, trapping of the tip during approach could be due to the blunt nature of the tip. It is evident from Fig. 3-4b, e that the

observed phase contrast in Fig. 3-2j-1 could have occurred due to the phase switching in bi-stable region present between approach and retract curve. However, the magnitude of $\Delta\phi$ for several APD curve were observed to be in the range of 20-40°, which is smaller than the observed $\Delta\phi$ in the image. These results suggest that, apart from the existence of the bi-stable state, there might be other reasons (discussed next) for the observed phase contrast.

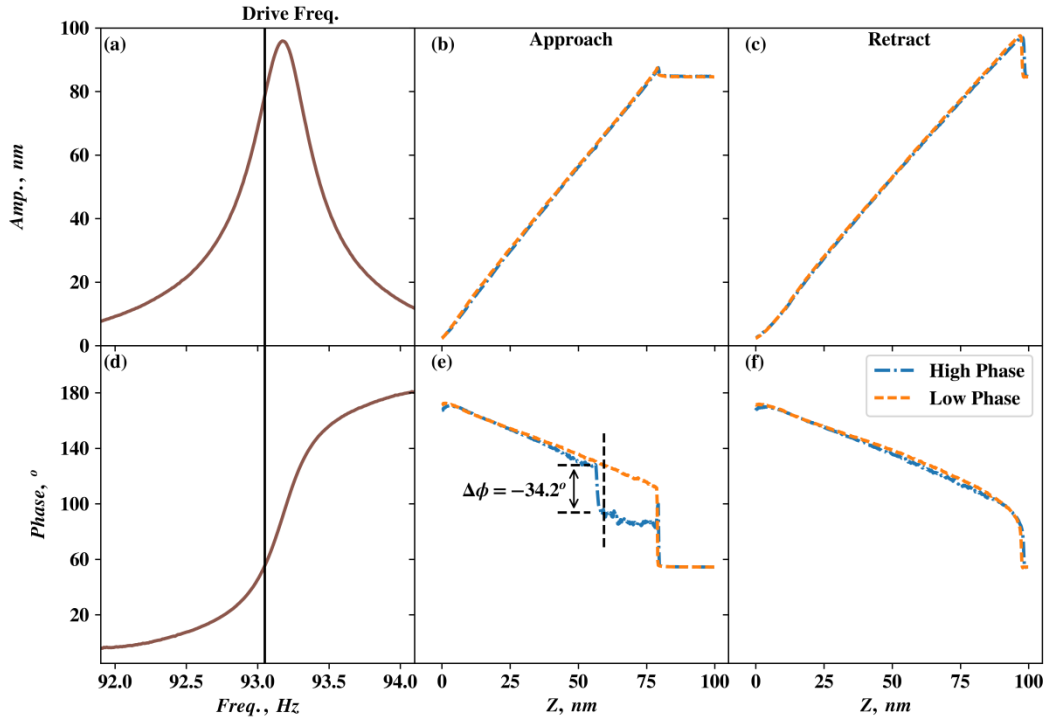


Fig. 3-4: (a) Amplitude and (b) phase of the cantilever oscillation at 200 nm from the surface. (c), (e) is the amplitude vs z plot for the approach and the retract of the cantilever to the surface, (d), (f) is the phase shift of the cantilever as the cantilever approaches or retract from the surface.

Another source of artifact could be the history of the system during imaging^{105,131,136}. From APD curve, it is evident that a bi-stable region exists for the given A_0 . Depending upon the initial condition i.e., $z, \dot{z}, \omega t$ etc., and chosen condition (such as A_{sp}), the tip can reach either of the two states. During imaging, these conditions might change and may result in switching of states. Phase

space projection or Poincaré sections are drawn to understand which state will be more stable and under what condition the switching might occur. It has been reported that intrinsic perturbations are mainly responsible for the switching between the states. These intrinsic perturbations are also one of the reasons for the enhanced $\Delta\phi$. The average roughness of (R_a) the substrate was found to be between 0.4-0.6 nm. Hence, due to R_a of the surface, the initial conditions will change continuously and may assist in switching between states. During switching, z_C might move towards or away from the sample before the feedback loop takes over, resulting in topographic variations. It should be noted that every feedback loop has a certain response time. If the scanning parameters are selected in such a way that the feedback loop cannot respond to the change in cantilever dynamics, the topography gets affected^{137,138}. Topographic variations were observed at only RH 20%,. However, at small A_0 , no topographic variations were observed. Hence, topographic variations observed at high A_0 can only be attributed switching of states.

The topographic variation could also arise due to the slope of the sample which can change the initial condition for the tip during imaging^{134,139}. In the present study, we noticed that there was a slope in the sample as shown in Fig. 3-5a. A cross-section along x and y direction is shown in Fig. 3-5b. The presence of the slope suggests that there might have been a sliding component in the tapping mode imaging. While capturing APD curve, the tip takes the reading at one point. Therefore, the forward velocity of the tip can be assumed to be zero. During scanning, the tip has certain forward velocity (lateral tip-sample displacement), which depends on the scan length and the scan frequency. From Fig. 3-2j, it can easily be noticed that most of the phase shift is oriented along the x -axis, which is the fast scan axis of the AFM. This suggests that the forward velocity plays an important role in the observed phase contrast. In the present case, the scan length was varied from 25-40 μm and the scan speed was 1 Hz. Therefore, the forward velocity of the tip was around 25-40 $\mu\text{m/s}$. Hence, there might be some friction between tip and the substrate, which could result in the observed phase contrast. Apart from this, hysteresis between advancing and receding angle of water on PMMA from dynamic contact angle has also been reported¹⁴⁰.

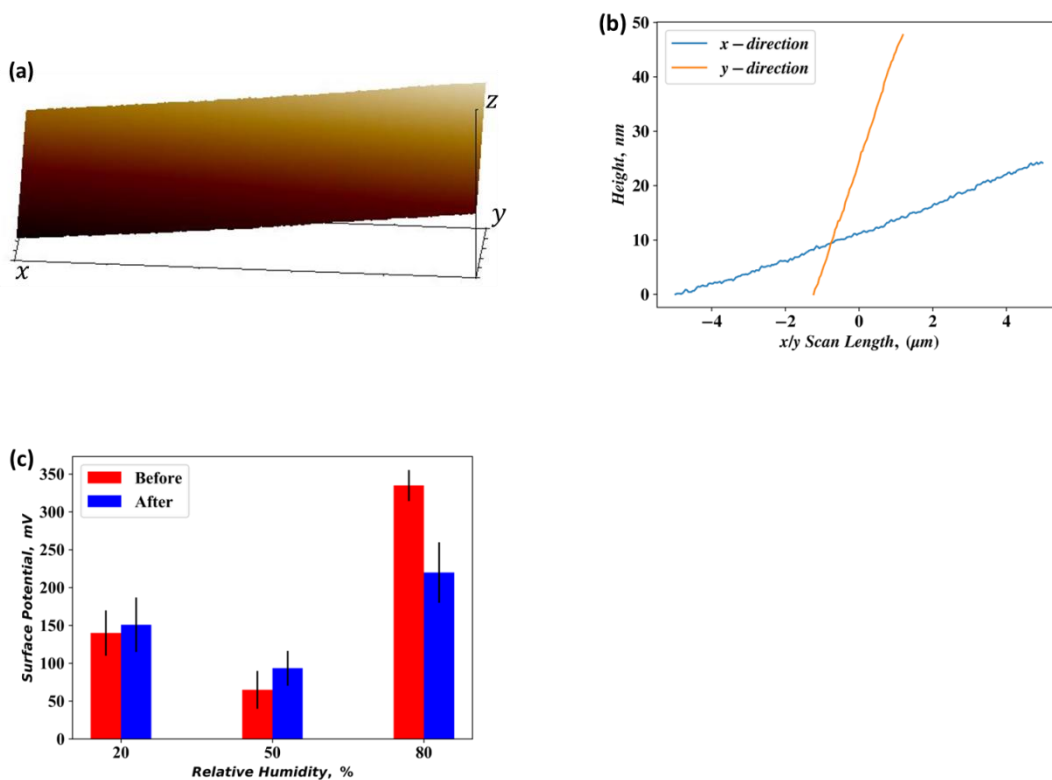


Fig. 3-5: (a) The topography image captured during the charge generation, (b) a cross-section profile and x and y direction, (c) change in the surface potential before and after tapping mode imaging.

Also, out of 6 Pt-coated tips, these observations could be made only for 2 tips and no phase contrast was observed for the plain Si tips. It has been reported that the observed phase shift in tapping mode might depend on the tip condition¹⁰¹. This could be one of the reasons why the phase shift was not observed with the other tips. Another reason could be that the coefficient of friction between a Pt-coated tip and PMMA might be different than a Si tip and PMMA.

Finally, the surface potentials before and after tapping mode imaging were compared (Fig. 3-5c). Except for RH 80%, the surface potential has increased for all other relative humidity. The decrease in surface potential at RH 80% could be due to the charge dissipation. It is well known that at higher humidity, due to increased mobility of H_3O^+ and OH^- , ion charges may dissipate faster. The increase in the surface potential for RH 20 and 50% after tapping mode imaging could

be due to an occasional change in the tip state from AR to RR. It has been reported that during tapping mode imaging, surface charges are produced in repulsive regime⁵⁰. From VEDA simulation, we also observed that the peak force was repulsive for A_0 and A_{sp} chosen during this study. The generation of these surface charges has been hypothesized due to phonon generation from the energy dissipated during the contact which results in the phonon generation. However, we noticed that the energy dissipation between the tip and sample occurred even during AR. This indicates that the charge generation due to phonons seems unlikely. Here we suggested that friction might have appeared during tapping mode imaging. The bond breaking and ionic process seemed to be involved during tapping mode imaging as well.

3.5 Conclusion

In this chapter, we investigated the role of interfacial water during triboelectric charging. Since water has higher dielectric constant than the PMMA substrate, EFM study was done to identify whether the amount of interfacial water between charged and uncharged region has changed. Although there was an evidence of increased water content in the charged region, it was statistically not significant. The phase imaging from tapping mode revealed a phase contrast between the charged and uncharged region during imaging. The origin and evolution of phase contrast were discussed in detail. It was shown that apart from the bi-stable region in APD curve, the viscous force arising due to the presence of interfacial water, friction, etc. led to a higher phase shift during imaging.

4 Physics of Contact Mode Triboelectric Nano-generator

4.1 Introduction

To harvest energy from TENG devices several types of designs have been proposed^{3,5}. Based on the operating principle they can be categorized into four different types: contact mode, sliding mode, free-standing, and single electrode based TENG^{3,141}. Their operating principle varies in a sense that the capacitance of TENG changes in case of contact mode and sliding mode, whereas it remains constant for free-standing and single electrode TENGs¹⁴². The working principle of TENG devices is very simple and is based on triboelectric charge generation and electrostatic induction^{68,143}. Due to a simple structure and a relative ease of fabrication, contact mode TENG devices were studied. The devices consist of at least one insulator layer and two metal electrodes. To explain the basic principle, we will assume that there are two insulators with metal electrodes at the back connected to an external load (Fig. 4-1a). When two insulators are brought in contact with each other, depending upon triboelectric series, charges are generated on both of them. One insulator becomes positively charged and the other one, negatively charged. Since the rate of dissipation of the charges on insulator is very slow, these charges stay on the surface for a very long time. When the two materials start to separate, due to electrostatic induction, opposite charges are induced on the metal electrodes. These induced charges (Q) flow through the external load creating voltage and current in the circuit. Hence, TENG devices are capacitive in nature^{142,144}. Since the amount of charge remains constant for each cycle, the energy is harvested due to the change in capacitance. Therefore, the basic characteristics of TENG devices are best understood from the $V - Q - x$ relationship, where x represents the change in the capacitance during a TENG operation. There have been several studies done exploring $V - Q - x$ relationship for all types of TENG devices¹⁴⁵⁻¹⁴⁸. These studies were mostly focussed on the device characteristics with a resistive load^{145,149} or energy storage in a capacitor or battery^{150,151}, etc. However, relatively less attention has been paid to address the issue of parasitic capacitance (C_p) associated with TENG devices and how they influence the performance of TENG devices. To the best of our knowledge, only one study has extensively discussed C_p but it has mostly focused on the theoretical treatment

of the problem¹⁶. Here we discuss how C_p influences TENG performance and compare it to the experiments.

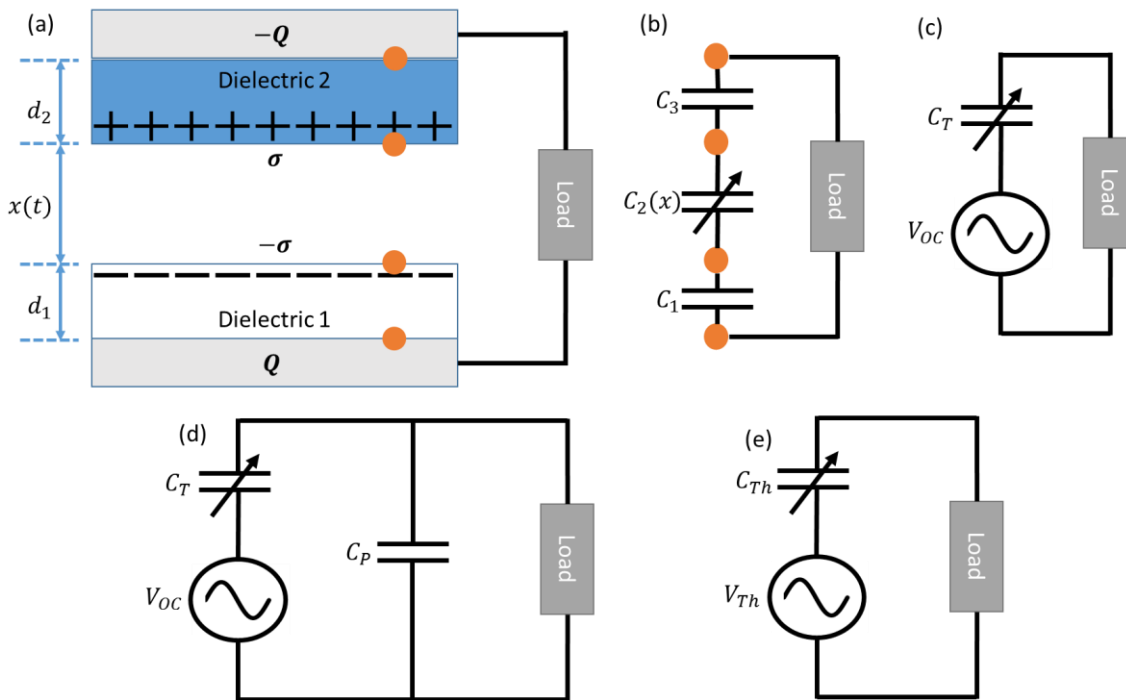


Fig. 4-1: (a) The schematic of a contact mode TENG device operation, (b) The electrical elements associated with (a), (c) Equivalent Circuit for a TENG device, (d) a TENG device with C_p , (e) Equivalent circuit for a TENG device with C_p

4.1.1 Equivalent Circuit of a TENG device

Since TENG is a capacitive device, it can be easily understood by the concept of electrical nodes¹⁵². An electrical node is defined as a point where two or more electrical circuit elements meet. Let us assume that σ is the triboelectric charge density generated on each insulator as shown in Fig. 4-1a. In Fig. 4-1a, four orange dots represent four electrical nodes. Based on these nodes, an equivalent electrical circuit is shown in Fig. 4-1b. The capacitance of a TENG device varies due to $C_2(x)$. Since x varies with t , the equivalent capacitance of a TENG device becomes

$$\frac{1}{C_T(x)} = \frac{1}{C_1} + \frac{1}{C_2(x)} + \frac{1}{C_3} \quad \text{Eq. 4-1}$$

where C_1 and C_3 arise due to the dielectric materials. For contact mode TENG, the area of the dielectric is the same; therefore C_T becomes:

$$C_T(x) = \frac{\varepsilon_0 S}{(d_0 + x(t))} \quad \text{Eq. 4-2}$$

where d_0 is given as:

$$d_0 = \frac{d_1}{\varepsilon_{r1}} + \frac{d_2}{\varepsilon_{r2}} \quad \text{Eq. 4-3}$$

ε_0 is the permittivity of free space, d_i, ε_{r_i} is the dielectric thickness and dielectric constant of dielectric $i = 1, 2$ and S is the area.

If the charge on Node 1 is assumed to be Q (Q is the induced charge, from the triboelectric charge on dielectric surface, on the metal plate)¹⁵³, then the charge on C_1 is Q . Now, $-S\sigma$ charge is present on Node 2, of which Q charge is compensated on C_1 , from Gauss Law, the charge on C_2 is $Q - S\sigma$ and on C_3 is $Q - S\sigma + S\sigma = Q$. Therefore, the voltage across three capacitors is given as:

$$V_1 = \frac{Q}{C_1} \quad \text{Eq. 4-4}$$

$$V_2 = \frac{Q - S\sigma}{C_2} \quad \text{Eq. 4-5}$$

$$V_3 = \frac{Q}{C_3} \quad \text{Eq. 4-6}$$

The voltage (V) drop across the external load can be determined with the help of Kirchhoff's Voltage Law (KVL)¹⁵².

$$V + V_1 + V_2 + V_3 = 0 \quad \text{Eq. 4-7}$$

Substituting Eq. 4-4 - Eq. 4-6, in Eq. 4-7:

$$V = -Q \left(\frac{1}{C_1} + \frac{1}{C_2} + \frac{1}{C_3} \right) + \frac{S\sigma}{C_2} \quad \text{Eq. 4-8}$$

Using Eq. 4-1 and Eq. 4-2 in Eq. 4-8, we get:

$$V = -\frac{Q}{\epsilon_0 S} (d_0 + x(t)) + \frac{\sigma x(t)}{\epsilon_0} = -\frac{Q}{C_T(t)} + \frac{\sigma x(t)}{\epsilon_0} \quad \text{Eq. 4-9}$$

Eq. 4-9 constitutes the basic working equation for a TENG device. Based on Eq. 4-9, the device characteristics of short circuit and open circuit can be easily determined.

For the short circuit condition, the potential difference generated across the load is 0 i.e., $V = 0$. Hence, Eq. 4-9 gives:

$$Q_{sc}(x) = \frac{S\sigma x(t)}{(d_0 + x(t))} \quad \text{Eq. 4-10}$$

where Q_{sc} is the charge transfer under the short circuit condition.

For the open circuit, no charge will be transferred across the load, i.e., $Q = 0$. Again from Eq. 4-9, we get:

$$V_{oc}(x) = \frac{\sigma x(t)}{\epsilon_0} \quad \text{Eq. 4-11}$$

Now, substituting Eq. 4-11, in Eq. 4-9, we get:

$$V(t) = -\frac{Q}{C_T(t)} + V_{OC}(t) \quad \text{Eq. 4-12}$$

From Eq. 4-12, it is evident that the voltage generated by TENG across the load can be represented in terms of a capacitor and a voltage source which are varying periodically. The electrical representation of TENG is given in Fig. 4-1c. Although the above equation is derived for the contact mode TENG, it has been shown that this equation is valid for all other types of TENG devices as well^{142,145}.

4.1.2 Role of Parasitic Capacitance

Eq. 4-12 has been derived considering an ideal situation. In practice, there are several sources of parasitic capacitance which might present during a device operation. This parasitic capacitance (C_p) can drastically influence the performance of a TENG device. C_p can be modelled as another capacitor in parallel to a TENG device as shown in Fig. 4-1d. Since C_p is always present with the circuit, the equivalent circuit of TENG can be modified to include C_p . For this purpose, Thévenin's theorem can be used¹⁵². At first, Thévenin equivalent voltage (V_{Th}) is determined under an open circuit condition where all the charges are transferred only to C_p and none to the external load. If Q_1 charge is transferred to C_p , then Thévenin equivalent voltage, as viewed from a load terminal, is given as:

$$V_{Th}(t) = \frac{Q_1}{C_p} \quad \text{Eq. 4-13}$$

But from Eq. 4-12, we have:

$$\frac{Q_1}{C_p} = -\frac{Q_1}{C_T(t)} + V_{OC}(t) \quad \text{Eq. 4-14}$$

Solving for Q_1 and substituting in Eq. 4-13, we get:

$$V_{Th}(t) = \frac{V_{OC}(t) \cdot C_T(t)}{(C_T(t) + C_P)} \quad \text{Eq. 4-15}$$

Next, we determined the Thévenin equivalent impedance of the circuit. To determine the equivalent impedance, the voltage source is short-circuited. Therefore, the two capacitors are parallel to each other, which gives Thévenin impedance (C_{Th}) as:

$$C_{Th}(t) = C_T(t) + C_P \quad \text{Eq. 4-16}$$

From Eq. 4-15 and Eq. 4-16, it is evident that the voltage source and impedance of the device change due to C_P . Hence, for the external load, Eq. 4-12 modifies to:

$$V = -\frac{Q}{C_{Th}(t)} + V_{Th}(t) \quad \text{Eq. 4-17}$$

Since TENG is a capacitive device coupled with C_P , the governing equation (Eq. 4-17) is similar to Eq. 4-12. Therefore, the equivalent circuit of TENG is also similar, except that the voltage source and impedance of the device have changed due to C_P (Fig. 4-1e). Again, the above equations have been derived for contact mode TENG devices, but these equations hold true for other types of TENG devices as well¹⁶.

The performance of TENG devices can be predicted from the above equations. To understand how parasitic capacitance influences the performance of a TENG device, we undertook numerical calculation considering the factors given in Table 4-1.

Based on the parameters assumed in Table 4-1, C_T and Q_{SC} was calculated based on Eq. 4-2 and Eq. 4-10. Fig. 4-2a shows how C_T and Q_{SC} changes with displacement (x). It can be clearly seen that C_T and Q_{SC} varies inversely with x . From Eq. 4-17, it can be easily seen that under short circuit condition the charge transfer is not affected by C_P . Therefore, Q_{SC} has been calculated for

$C_p = 0$ only. However, from Eq. 4-15, V_{Th} is affected by the parasitic capacitance. Hence, V_{Th} for different C_p were calculated and shown in Fig. 4-2b. It can be seen that V_{Th} is maximum (and = V_{OC}) when $C_p = 0$. It should be noted that $V_{Th,max}$ starts to drop as C_p increases and saturates after certain x .

These results were compared with the experimental results. The details of the experiments are discussed in the experimental section below. The time-varying short-circuit current (i_{sc}) and open circuit voltage (V_{OC}) of TENG is shown in Fig. 4-2c, d. From Fig. 4-2c, Q_{SC} was calculated, by integrating the current over time i.e., $Q_{SC} = \int_0^t i_{sc} dt$ and was found to be 60 ± 2 nC. Similar values have been used for the numerical calculation (Table 4-1). However, from voltage measurement V_{max} was 180 ± 7 V only. This value was significantly smaller than the one calculated considering Eq. 4-11 and shown in Fig. 4-2b (for $C_p = 0$). These results clearly suggest the presence of C_p with the devices. Therefore, the distance dependence of V_{Th} and Q_{SC} was measured and is shown in Fig. 4-2e. A hysteresis can be observed for both Q_{SC} and V_{Th} suggesting that the movement of the plates may not be parallel. Indeed, during experiments, it was observed that there was a slight wobbling in the upper electrode. Comparing Fig. 4-2b and e, it was found that C_p was around 300 pF. The observed C_p was almost equivalent to C_T . The origin of such a high C_p may be as a result of the coupling between stepper motor and TENG electrodes.

Table 4-1: Parameters used for the model.

Dielectric 1	Metal ($\epsilon_{r_1} = \infty, d_1 = 0$)
Dielectric 2	($\epsilon_{r_2} = 3.4, d_1 = 125 \mu m$)
Surface Charge Density	$30 \mu C/m^2$
Displacement	$2.4 mm$
Velocity	$1.5 - 2.4 mm/s$
Area	$20 cm^2$

These results clearly indicate that the performance of a TENG device will be significantly affected by C_p . Hence, it is important to understand the performance figure of merits (FOM_p) of these TENG devices¹⁵⁴. Before discussing FOM_p , the assumptions used in deriving the above equations and their implications need to be addressed.

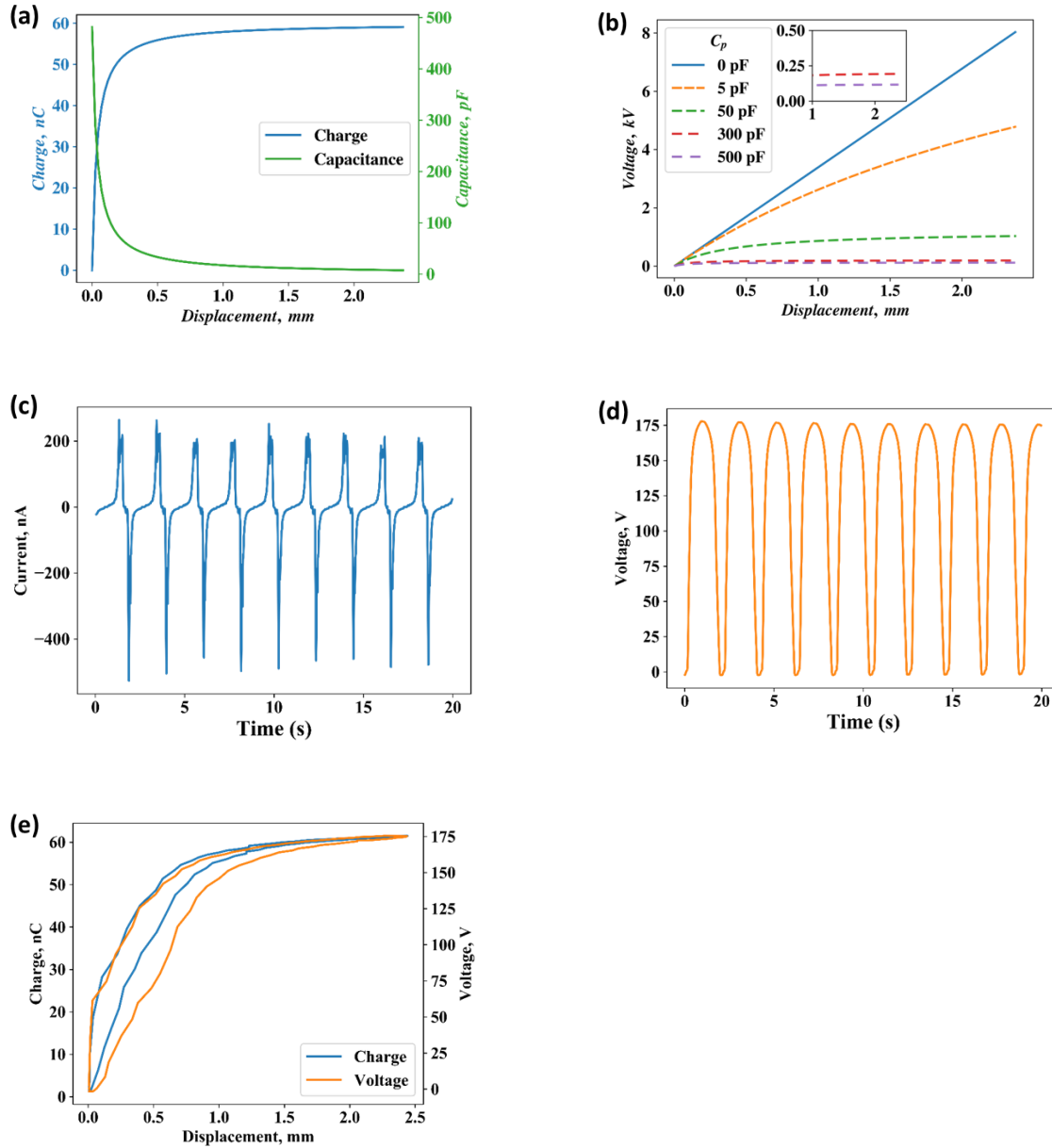


Fig. 4-2: (a) Charge and Capacitance, (b) Open circuit voltage of a TENG device as a function of displacement, (c) time-varying current and (d) voltage of a TENG device. (e) Charge and Voltage as a function of displacement.

4.1.3 Minimum Achievable Charge Reference State (MACRS)

From Eq. 4-10 and Eq. 4-11, one can see that the electrical output of TENG devices depends significantly on σ i.e., amount of charge generated on the dielectric. For any electrostatic system, a frame of reference needs to be defined where potential, $V = 0$ is assumed. From Eq. 4-11 and Eq. 4-15, it can be seen that when $x = 0$, $V = 0$. Therefore, the above equations have been derived under the assumption that the reference plane is at $x = 0$. It should be noted that Q is also 0. Comparing Eq. 4-2, Eq. 4-10 and Eq. 4-11, we see that:

$$V_{Th}(x) = \frac{Q_{SC}(x)}{C_{Th}(x)} \quad \text{Eq. 4-18}$$

Now, if due to some reason Q is not 0 at $x = 0$, then V_{Th} will be non-zero, implying that the reference plane has been shifted at some other x . This reference plane can be shifted by short circuiting TENG at another value of x . Therefore, experimentally, it is possible to change the reference plane of a TENG device. Let us assume that the new reference plane is \bar{x} . When the device is short circuited at \bar{x} , the charge from the two electrodes will neutralize each other making $Q_{SC}(x = \bar{x}) = 0$. Since maximum displacement (x_{max}) is constant, from Eq. 4-10 we see that the total Q_{SC} will be constant, is observed experimentally (Fig. 4-3a) but its magnitude will change with \bar{x} . In Fig. 4-3a Q_{SC} has been calculated by subtracting $Q_{SC,\bar{x},min}$ with $Q_{SC,\bar{x}}$ and x_{max} was 1.2 mm. Therefore, the relationship between Q_{SC} at $x = 0$ and Q_{SC} at \bar{x} can be written as:

$$Q_{SC,\bar{x}}(x) = Q_{SC}(x = 0) - Q_{SC}(x = \bar{x}) \quad \text{Eq. 4-19}$$

However, it was noticed that $V_{Th,\bar{x}}$ changes significantly with \bar{x} as shown in Fig. 4-3b. Here again the magnitude of $V_{Th,\bar{x}}$ has been reported. Since the reference plane of charges has been changed, the V_{Th} will also change following Eq. 4-18.

$$\begin{aligned}
V_{Th,\bar{x}}(x) &= \frac{Q_{SC,\bar{x}}(x)}{C_{Th}(x)} && \text{Eq. 4-20} \\
&= V_{Th}(x=0) - \frac{Q_{SC}(x=\bar{x})}{C_{Th}(x)}
\end{aligned}$$

From Eq. 4-20, it is evident that V_{Th} changes because $C_{Th}(x)$ is not constant. The $C_{Th}(x)$ changes because C_T is not constant. The variation in $V_{Th,\bar{x}}$ for different \bar{x} and C_p was calculated using Eq. 4-20 and is shown in Fig. 4-3c. It can be readily seen that $V_{Th,\bar{x}}$ decreases rapidly with \bar{x} irrespective of C_p . Since we have already determined that during these observations C_p was 300 pF, $V_{Th,\bar{x}}$ for three different displacements were calculated and compared to experiments (Fig. 4-3d). The calculated and experimental value of $V_{Th,\bar{x}}$ were found to be completely different. This huge difference in $V_{Th,\bar{x}}$ cannot be explained by the small angle between the top and bottom electrode as discussed above. One of the reasons could be that C_p was comparable to $C_T(x_{min})$. Therefore, some higher order term might need to be considered. However, both theory and experiments predict that $V_{Th,\bar{x}}$ will decrease as \bar{x} shifts away from $x = 0$.

From the above discussion, it is clear that the choice of \bar{x} can significantly influence the magnitude of V_{Th} . Therefore \bar{x} , should be chosen in a way that gives maximum V_{Th} . However, from Eq. 4-20, it is possible only when $Q_{SC}(x = \bar{x})$ should be zero i.e., when $\bar{x} = 0$. When $\bar{x} = 0$, two charged surfaces share the same plane. Hence, theoretically no charges should be induced on the electrode. Thus, at $\bar{x} = 0$ the charges on the electrode are at their minimum achievable state. Therefore, the reference plane for contact mode TENG at $\bar{x} = 0$ is generally chosen and is referred to as minimum achievable charge reference state (MACRS)^{142,148}.

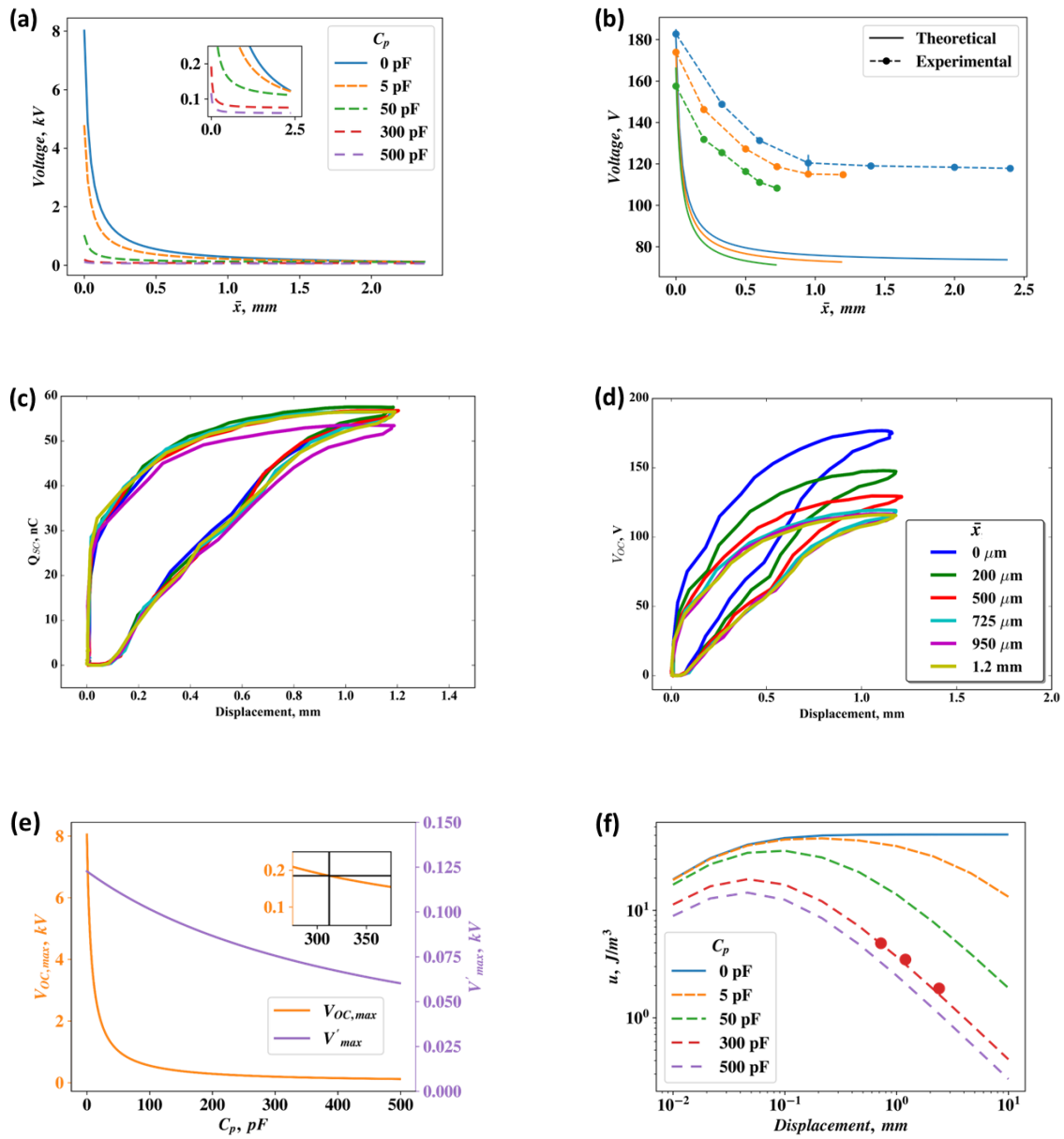


Fig. 4-3: (a) V_{OC} as a function of different reference plane (\bar{x}) and C_p , (b) Computed and experimental V_{OC} for $C_p = 300$ pF but different x_{max} . Experimental (c) Charge, (d) V_{OC} as a function of different \bar{x} . (e) Voltage as a function of C_p for $x = 0$ and x_{max} and (f) energy density as a function of displacement for different C_p .

4.1.4 Performance Figure of Merits (FOM_P)

The parasitic capacitance associated with TENG devices can significantly influence the performance of the device. Therefore, FOM_P of contact mode TENG has been compared for different C_P and x . FOM_P of TENG devices is given as¹⁵⁴:

$$FOM_P = 2\varepsilon_0 \frac{E_m}{Ax_{max}} \quad \text{Eq. 4-21}$$

Where, E_m is the maximum energy output from a TENG device and is given as^{16,154}:

$$\begin{aligned} E_m &= \frac{1}{2} Q_{SC,max} (V_{Th,max} + V'_{max}) \\ &= \frac{1}{2} Q_{SC,max}^2 \left(\frac{1}{C_{T,max} + C_P} + \frac{1}{C_{T,min} + C_P} \right) \end{aligned} \quad \text{Eq. 4-22}$$

V'_{max} in the above equation is the maximum voltage when $\bar{x} = x_{max}$.

It has been shown that with few modifications in TENG electrode configuration, the maximum energy from the device can be harvested. However, those modifications can be tricky and unnecessary if only device performance needs to be evaluated. Therefore, in the present study, V'_{max} was obtained experimentally by defining \bar{x} at x_{max} . It should be noted that E_m can be calculated without determining $V_{Th,max}$ or V'_{max} but C_P needs to be determined for the calculation. However, determining C_P could also be tricky as well. Also, as noted in Fig. 4-3d, the experimental value of V'_{max} can be different from one determined using C_P . Therefore, determining $V_{Th,max}$ and V'_{max} individually is significantly simple compared to changing electrode configuration or determining C_P for evaluating device performance. The computed value of $V_{Th,max}$ and V'_{max} for $x = 2.4 \text{ mm}$ has been shown in Fig. 4-3e. As the C_P increases $V_{Th,max}$ decreases more rapidly than V'_{max} . Hence, FOM_P will be significantly affected by $V_{Th,max}$.

FOM_P by itself does not give any particular perception about the device but $FOM_P/2\varepsilon_0$ which is the energy density (u) provides insight into the energy which can be harvested. Hence, instead of calculating FOM_P , u of the device was calculated and is shown in Fig. 4-3f.

$$u = \frac{FOM_p}{2\varepsilon_0} = \frac{E_m}{Ax_{max}} \quad \text{Eq. 4-23}$$

From Fig. 4-3f, it is evident that u is maximum when $C_p = 0$ which saturates around 51 J/m^3 at $x \approx 2 \text{ mm}$. It should be noted that for the considered parameters this is the maximum electrostatic energy ($u = \frac{1}{2} \varepsilon_0 \varepsilon_r \vec{E}^2$, where \vec{E} is the electric field) which can be harvested. However, due to the presence of C_p , some amount of energy will be dissipated to it. Hence, as the C_p increases both u and x_{opt} (x_{opt} = displacement required for u_{max}) decreases. The change in x_{opt} suggest that after certain x the energy generated from TENG is mostly lost to C_p . For instance, when $C_p = 50 \text{ pF}$, u_{max} decreases by 30% and x_{opt} is only $100 \text{ }\mu\text{m}$. In our study, C_p was around 300 pF because of which u_{max} decreased by 62%. u for 3 different displacements were determined and is shown as maroon dots in Fig. 4-3f. The calculated value of u matches closely with the $u_{C_p=300 \text{ pF}}$. This observation suggests that calculation of u is not affected by the discrepancy observed in Fig. 4-3d. Moreover, compared to $C_p = 0$, u drops to approx. 10% for $x = 0.72 \text{ mm}$ and approx. 4% for $x = 2.4 \text{ mm}$. These results clearly suggest that a design guideline for TENG that addresses the concerns of C_p and helps in optimizing x_{max} should be established. This is particularly important considering the fact that the frequencies of ambient resources are generally less than 10 Hz. Hence, the power generated will be more significantly affected by high C_p and x_{max} .

4.2 Conclusion

The working principle of contact mode TENG devices has been discussed. The governing equation of TENG devices can be written as time-varying voltage source and capacitor. For deriving the equivalent circuit, the reference plane was assumed to be at $x = 0$. The role of parasitic capacitance has also been discussed. It was shown that the maximum energy harvested from TENG devices are significantly affected by the parasitic capacitance. Although these results were discussed in the context of contact mode TENG, similar behavior can be observed for different type of TENG devices. Therefore, addressing the parasitic capacitance and optimizing the displacement of TENG will be crucial for an efficient TENG device operation.

4.3 Experimental Setup

To understand the basic physics and evaluate the performance of TENG devices controlled mechanical motion i.e., controlled force, speed etc. is required. Therefore, an in-house stepper motor based linear actuator was developed. The detail of the setup is given in Appendix C. The total applied force on TENG devices, during the operation was approx. 19.5 N (~ 2 kgf).

For electrical characterization, Keithley 6514 electrometer was used. For open circuit voltage (V_{OC}) and short circuit current (i_{sc}) was taken from Keithley 6514 electrometer. The displacement was measured using a variable resistor. The reading from electrometer and variable resistor from Arduino were taken by a home written python code. Further analysis was also performed using a code written in python. Data analysis from the recorded data is also discussed in Appendix C.

To understand the physics of a TENG device operation, Kapton® film and copper clad PCB board were used. Kapton® was purchased from McMaster Carr and copper clad PCB board was purchased from Digikey. The thickness of Kapton® film was 125 μm . The dielectric constant of Kapton® is 3.4¹⁵⁵. On one side of Kapton® film, the copper tape was attached. The area of Kapton® film was 20 cm^2 . Before and after placing copper tape, Kapton® film was rinsed with water, acetone, and ethanol to remove organic contaminants and surface charges that might have generated during the process. A similar procedure was repeated for copper clad PCB board. Before starting the experiments, Kapton® film was rubbed against copper clad PCB which gave consistent surface charge density of 30 $\mu\text{C}/\text{m}^2$.

5 Radicals and Triboelectric Nano-generators

5.1 Introduction

While investigating triboelectric effect, one of the major focuses is to understand the amount of charge generated and the polarity of charges^{9,17,29,39}. The triboelectric charges generated have a significant effect on the performance of TENG devices¹⁵⁴. Therefore, to increase the charge density one generally refers to triboelectric series^{9,17}. Triboelectric series is an empirical series compiled based on several reported literature values. Since the series is empirical, engineering materials for TENG applications based on this series are limited. As shown in Chapter 2, the chemical reaction taking place at the interface plays an important role during charge generation. An understanding of these chemical reactions will not only help control and manipulate the surface charge generated but also give insight into several potential applications. For instance, in Chapter 2, we noticed that the amount of charge generated does not correlate with the energy dissipation at the interface. Those results indicated that a part of the dissipated energy is lost to some other processes such as phonons²⁴, radical generation^{35,36} etc. Therefore, if the interfacial phenomenon is controlled, energy loss from these mechanisms can be minimized and the maximum amount of dissipation energy could be utilized for generating charges. Another important area of TENG devices is chemical sensing. Chemical sensing based on TENG principle has been demonstrated^{91,92,156,157} but they are not based on interfacial chemistry. The chemical reactions between the reactants were well established and TENG was used for probing the chemical reaction. However, during triboelectric effect, it has been shown that radicals are generated at the interface^{34-37,158-160}. These radicals have been utilized for depositing nanoparticles; changing pH of the solution, changing the electrical properties of aniline etc^{34,62,88,89,161}. Also, triboluminescence effect¹⁶² has been demonstrated with TENG devices and was proposed for sterilization purposes¹⁶³. These examples clearly illustrate by engineering the interfacial chemistry, happening during TENG operation, several technologically important applications can be derived.

For this purpose, we need to understand the effect of molecular design and chemical characteristics of triboelectric materials during the triboelectric effect. One way is to understand the role of radicals generated during triboelectric charging. A radical is an atom or a molecule with an

unpaired electron(s) i.e., their octet is not complete¹⁶⁴. In other words, their highest occupied molecular orbitals (HOMO levels) are half filled which is commonly referred to as singly occupied molecular orbital (SOMO). A radical can undergo reaction with ion which can give or take away electron(s) from them, making the radical an ion while the reactant ion becomes a radical ($R\cdot + R'^+ \rightarrow R^+ + R'\cdot$ or $R\cdot + R'^- \rightarrow R^- + R'\cdot$, where R and R' could be two different or similar reactants). This is generally referred as the propagation step of radical. On the other hand, radical might react with another radical and neutralize themselves ($R\cdot + R\cdot \rightarrow R-R$) resulting in termination of radicals. Generally, radicals are produced as an intermediate product of the reaction and get annihilated as the reaction proceeds or stops. However, in case of triboelectric charging, it has been shown that the radicals are generated from homogeneous scission of C-C bond from the main polymer due to mechanical action³⁷.

The radicals generated during triboelectric effect have been termed as mechano-radicals^{34,36}. It has been proposed that the stability of triboelectric charges in ambient condition could be due to the interaction of SOMO of radicals with HOMO or LUMO (Lowest Unoccupied Molecular Orbital) of ions which lowers their potential energy^{35,165}. Similar observations were reported by Sakaguchi et. al. but they also reported that higher amount of charges assist in generating more radicals³⁶. Most of their understanding about mechano-radicals and associated chemistry was from reactions under liquid nitrogen atmosphere^{36,37}. It is well known that triboelectric effect has a significant dependence on the ambient conditions. This could be understood by the fact that they reported generation of peroxy radicals due to dissolved oxygen in liquid nitrogen^{36,37}. It has been shown that the generated mechano-radicals can stay on the surface longer than triboelectric charges³⁵. In order to generate the maximum charge, the amount of energy dissipated at the surface should be optimized so that more ions are generated together with sufficient mechano-radicals to stabilize the produced charges. In order to achieve this, the chemical nature of radicals and charges needs to be understood in detail. In Chapter 2 and 3 we discussed few of the chemical and interfacial phenomenon associated with the charge generation. However, the nature and role of radicals during triboelectric charging under atmospheric conditions were not explored. For instance, how long these radicals stay on the surface and their relationship with the surface charge generation. Therefore, we studied the stability and interaction between generated triboelectric charges and radicals.

In the second study, we introduced radicals in TENG devices and evaluated the performance of the device against a TENG device without radicals. For this study, the material needed should have a stable radical molecule. Some of the stable radical molecules reported in the literature are NO centered nitroxides, *N*-centered triarylamminium cation radicals, and diphenylpicrylhydrazyl derivatives, *O*- centered phenoxyls and galvinoxyls and *C* centered trityls and phenalenyls¹⁶⁶. These radicals are stabilized by carefully designing the chemical structure of the pendant group which can suppress the chemical bond formation by utilizing electron resonance effect and steric hindrance¹⁶⁶⁻¹⁶⁸. Steric hindrance is generally achieved by using bulky substituent groups such as a methyl group. This pendant group is attached to the polymer, which acts as a backbone, by replacing a side chain. The polymer synthesized from these radicals has been reportedly used for battery application and are generally referred as Organic Radical Batteries (ORBs)¹⁶⁸⁻¹⁷⁰. The radicals in the polymer are isolated moieties which act as a redox sites. The charge transfer takes place in between radicals only via a self-exchange reaction. This transfer of charge from one radical to the other can be viewed as a propagation step as described above and is referred as a self-exchange reaction. This self-exchange reaction happens due to electric field gradient which causes the diffusion of charge via hopping mechanism¹⁶⁶. Therefore, to get a higher charge storage capacity, these polymers are densely populated with radicals and the molar mass of the repeating unit is minimized. Also, the charge transfer rate increases by populating radicals in polymers. Therefore, here we hypothesized that self-exchange reaction in these radical polymers might participate during triboelectrification and can provide a better understanding of materials chemistry to fabricate TENG devices with higher charge density.

Poly (2,2,6,6-Tetramethyl-4-piperidnyloxy methacrylate) (PTMA) radical polymer was used for this study. The chemical structure of PTMA is similar to PMMA except that the methyl group attached with carbonyl bond is replaced with the TEMPO ((2,2,6,6-Tetramethylpiperidin-1-yl)oxyl)group. It has been demonstrated that depending upon the type of reaction site at the interface, the charges generated will vary¹⁷¹. However, the side chain attached to the reaction site can also influence the triboelectric charging. Since the chemical structure of PTMA and PMMA are similar, we also studied how molecular design of the polymer affects triboelectric charging. In particular, we investigated how the reaction center is influenced by the size of the adjacent molecules attached to the polymer chain.

5.2 Experimental details

5.2.1 MFM study of Mechano-radical:

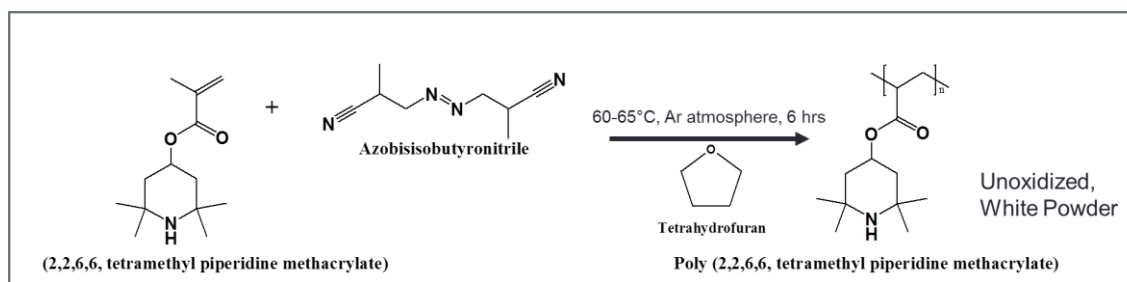
For MFM study, PMMA substrate was used. The details of substrate preparation and handling have already been discussed in Chapter 2. MFM study was carried out on Bruker's Dimension FastScan with Nanoscope V controller. MAGT-HM tip was procured from AppNano. MAGT-HM tip was used for MFM study because of the high magnetic moment of the tip ($>3e-13$ emu). Due to the high magnetic moment, the reported tip radius was very large (~ 75 nm). The charges were created in an area of $10 \times 10 \mu\text{m}^2$, using SCM-PIT with an applied force of 25 nN and scan frequency of 1Hz and tip oscillation frequency of 2kHz. A total of 10 scans was done to generate charges. AM-KPFM results from SCM-PIT and MAGT-HM results were compared. The potential generated due to surface charges were found to be similar with both the tips. Hence, AM-KPFM was also performed with MAGT-HM probe. For AM-KPFM, the lift height was 100 nm, whereas for MFM the lift height was not fixed. To magnetize the tip, it was placed over a magnet with a magnetic strength of 200 mT. For MFM in the magnetic field, the sample was placed in the magnetic field of 100 mT. The sample was placed on top of the magnet with a double-sided Kapton tape. The relative humidity during these experiments was varied between 15-30%.

5.2.2 Radical Polymer Synthesis

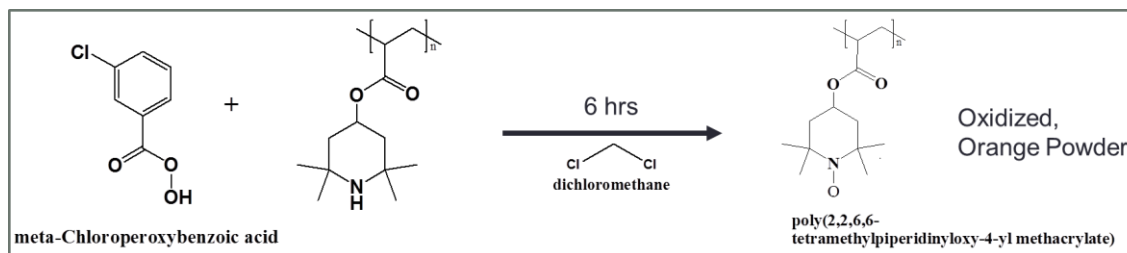
For the synthesis of PTMA procedure described by Nakahara et al was followed¹⁶⁹. Monomer 2,2,6,6-Tetramethyl-4-piperidyl methacrylate (TMA, purity $> 98\%$) was purchased from TCI America and was used without any further purification. Azobisisobutyronitrile (AIBN, purity $> 98\%$), dry Tetrahydrofuran (THF, purity $\geq 99.9\%$), meta-Chloroperoxybenzoic acid (mCPBA, purity $\leq 77\%$), dry hexane, dry dichloromethane (DCM, purity $\geq 99.8\%$), diethyl carbonate (DEC, purity = 99%) were purchased from Sigma Aldrich and used without further purification. Sodium Carbonate was purchased from Fisher Scientific. Ultrahigh purity Argon gas was purchased from Praxair. 5 g of monomer in 20 ml THF was prepared in a 3 necked round bottom flask. The inert atmosphere was maintained by slowly purging Ar gas. This was done to get rid of dissolved oxygen in THF which might scavenge the free radical during polymerization. To this solution, 4.4mM AIBN (monomer:AIBN = 4.5:1 mol:mol) was added. The solution was heated to 60-65°C and continuously stirred for 6h in an inert atmosphere, which initiated the radical polymerization reaction as shown in Scheme 1 given below. After the reaction was over, it was cooled to room

temperature and Ar gas flow was stopped. The resulting unoxidized polymer (poly (2,2,6,6-Tetramethyl-4-piperidanyl methacrylate) (PTMPM) was precipitated in hexane and filtered. This filtered polymer was then dried under vacuum for overnight and then grounded giving the yield of around 50%.

Scheme 1: Polymerization of TMA



Scheme 2: Oxidation of PTMPM to PTMA



2 g of PTMPM was dissolved in 20 ml dry DCM in a 100 ml round bottom flask. Simultaneously, 20 ml of 0.88M mCPBA solution was prepared in a beaker. This 0.88M m-CPBA solution was added dropwise to the 2 g polymer solution. This solution was continuously stirred for 6h. As soon as m-CPBA was added to the solution, the color of the solution became orange and oxidation started following Scheme 2. After the reaction, m-CPBA that had been precipitated was filtered out. The orange color DCM solution was collected. To this orange solution, supersaturated sodium carbonate solution was added and separated twice with the help of separating funnel. Cleaned DCM solution was dried in air. The resulting polymer (PTMA) was grounded and then washed twice again in DEC followed by drying in vacuum for overnight giving an overall yield of 20-25%.

5.2.3 Characterization of Radical Polymer

FTIR spectra of polymers were taken from Thermoscientific spectrometer. The module used for this study was Smart Diffuse Reflectance setup. FTIR grade KBr was procured from Sigma Aldrich. Before taking FTIR spectra of the polymer, background signal was collected from KBr pellet. Then a small amount of polymer was mixed with KBr and a pellet was prepared from this mixture. This pellet was used to obtain FTIR spectra.

The molecular weight and polydispersity of the polymer were determined by gel permeation chromatography (GPC) with two Waters Ultrahydrogel I-MBHMW-3078 columns and Viscotek model 250 dual detector. 10 mM LiBr DMF was used as eluent through a flow rate of 0.5 mL/min. MW was determined to be 53.3 kDa with polydispersity of 1.06.

Cyclic voltammetry (CV) was performed in two different ways. For one case, the electrode materials were prepared either by mixing the active material with carbon black in chloroform to form a homogeneous slurry. The slurry was then spread onto stainless steel spacer and dried at 60°C overnight in a vacuum oven. The active electrodes, along with a polyethylene separator, the electrolytes, and Li counter electrodes were assembled in an argon-filled glovebox into CR2032-type coin cells. The electrolyte employed was 1M LiPF₆ in ethylene carbonate/dimethyl carbonate (1:1). The CV is recorded on a multichannel-current static system (Arbin Instruments BT 2000, USA) at a sweep rate of 10 mV/s.

For the second case, a thin film of polymer was deposited on a stainless steel spacer and dried at room temperature in vacuum overnight. The coin cell was prepared in a similar manner as described above. The sweep rate for this battery was 1 mV/s.

Electron Paramagnetic Resonance studies were performed by Elexsys E-500 CW-EPR instrument. Before characterizing the radical polymer, TEMPOL (4-hydroxy-2,2,6,6-tetramethylpiperidin-1-oxyl) radical was characterized. Both TEMPOL and PTMA were dissolved in dichloromethane. Scanning was done at X-band frequency of 9.71 GHz for PTMA and 9.81 GHz for TEMPOL and the microwave power was 2 mW.

XPS was performed by Kratos AXIS 165 instrument with Al gun. A thin film of PTMA and PTMPM were coated on the copper substrate. The high-resolution spectrum of the N1s peak was collected. The XPS data was analyzed from CASA XPS software. For fitting N1s peak, linear

background fitting was performed. The peaks were fitted Marquardt-Levenberg optimization algorithm.

For TENG characterization, all three polymers (PTMA, PTMPM, and PMMA) were spin coated on a copper substrate and dried in vacuum for overnight. 20mg/ml of the polymer was dissolved in CHCl_3 . The spin-coated samples were kept in a vacuum for overnight. The thickness of these films was determined by cross-sectional SEM. For cross-sectional SEM, films were deposited on Si substrate. The substrate was then cleaved from the center and SEM was performed from the cleaved side. The thickness of the film was determined to be 450 ± 50 nm. The topography of PTMA and PTMPM was also done on Bruker's Dimension FastScan with Nanoscope V controller. ScanAsyst tip was used for topographic imaging. Imaging was done with ScanAsyst Mode. The second material was FEP. One side of FEP film was sputter coated with 200 nm thick Cu film to make back electrode contact.

The detail of TENG setup and experimental procedure has already been discussed in Chapter 4. In short, for voltage and current measurements, Keithley electrometer 6514 was used. Before, TENG evaluation, FEP was cleaned with water and ethanol. However, for PTMA, PTMPM, and PMMA, two different cleaning procedures were used. In the 1st case, they were cleaned only with water. In the 2nd case, films were cleaned with water and ethanol. During TENG characterization, the net applied load was kept between 17.5-20 N. The total displacement was 2.4 mm. It should be noted that smaller displacement results in higher performance of TENG devices. However, it was noticed that with smaller displacement abrasion in lead screw nut increases drastically. Therefore, higher displacements were used during the study.

5.3 Mechano-radicals and triboelectric charges

Radicals have a lone pair of electrons because of which they exhibit paramagnetic properties¹⁷²⁻¹⁷⁴. Therefore, Magnetic Force Microscopy (MFM) can be utilized for determining the presence of radicals on the surface. The advantage of implementing MFM for this study is that both the surface charge and radicals can be studied simultaneously³⁵ with the help of AM-KPFM and MFM respectively. This gives a direct correlation between the amount of charges and mechano-radicals which will be helpful for understanding the process more precisely.

The theory of surface charge detection has already been discussed extensively in Chapter 2 and 3. Therefore, only the theory of magnetic force detection is discussed here. For detecting magnetic forces, the magnetic tip is brought near to the magnetic sample, which interacts with the stray magnetic field emanating from the sample. The magneto-static interaction of the magnetic tip with the magnetic sample depends upon the geometry of the tip, the magnetic domains in the tip and sample. To understand MFM signal considering all the above parameters will be quite complex. Therefore, the simplest way proposed to understand the magnetic interaction is to model the tip as a point probe¹⁷⁵. The working principle of MFM is similar to that of electrical characterization measurement. Like EFM, the cantilever oscillates near to its resonance frequency. The magnetic interaction between the tip and sample will lead to the change in amplitude, phase, and frequency of the cantilever. In contrast to electrostatic forces, magnetostatic forces can be attractive or repulsive¹⁷⁵. In the present study, the phase shift ($\Delta\phi$) of the cantilever was monitored. It has been shown that $\Delta\phi$ is given as:

$$\Delta\phi = -\frac{Q}{k} \frac{\partial F_z}{\partial z} \quad \text{Eq. 5-1}$$

where $\partial F_z/\partial z$ is the force gradient along the z -direction. It should be noted that unlike in Chapter 3, the force gradient has not been designated as F_{mag} , where F_{mag} is the magnetic force. This is due to the fact that in the case of MFM, tip is metallic. Therefore, apart from the magnetostatic force, electrostatic forces also acts on the tip:

$$F_z \approx F_{elec} + F_{mag} \quad \text{Eq. 5-2}$$

Hence, the force gradient along z -direction from Eq. 5-2 can be written as:

$$\frac{\partial F_z}{\partial z} \approx \frac{\partial F_{mag}}{\partial z} + \frac{\partial F_{elec}}{\partial z} \quad \text{Eq. 5-3}$$

In the present case, both mechano-radical and triboelectric charges were present in the same location. Therefore a contribution from both electrostatic and magnetostatic forces was expected¹⁷⁶. That is why observed $\Delta\phi$ was denoted to be due to $\partial F_z/\partial z$. Hence, interpretation of radical generation during triboelectric charging needs to be done carefully. Baytekin et al concluded the presence of mechano-radicals by performing MFM study in presence and absence of the charges³⁵. The $\Delta\phi$ observed with MFM tip, in absence of the charges clearly indicated the presence of mechano-radicals. However, as we will see that the triboelectric charges can stay on the surface for considerably long periods. Therefore, a procedure needs to be established by which conclusive evidence of presence of radicals can be demonstrated.

The magnetostatic force gradient acting on a tip is given as¹⁷⁷:

$$\frac{\partial F_{mag}}{\partial z} = \frac{6m_z M_z}{\pi\mu_0 z^5} \quad \text{Eq. 5-4}$$

where m_z is the magnetic moment of the tip, M_z is the magnetic moment of the sample, μ_0 is the magnetic permeability in air.

The electrostatic force acting between the tip and sample has already been discussed in Chapter 3. Therefore, the $\Delta\phi$ (Eq. 5-1) observed between tip and sample from Eq. 5-4 and Eq. 3-5¹¹⁵, is given as:

$$\Delta\phi \approx -\frac{Q}{k} \left\{ \frac{6m_z M_z}{\pi\mu_0 z^5} + \frac{1}{2} \frac{\partial^2 C}{\partial z^2} (V_{tip} - V_S)^2 + \frac{\partial C}{\partial z} \frac{\sigma_s}{\epsilon_0} g_t (V_{tip} - V_S) \right\} \quad \text{Eq. 5-5}$$

It should be noted that electrostatic forces are function of the bias between tip and substrate whereas magnetostatic forces are the function of the tip and sample magnetic moment. Therefore, by varying the magnetic field of either the tip or the sample, the magnetic force between tip and sample can be changed^{172,175}. For Bruker AFM instrument, positive $\Delta\phi$ indicates attractive forces whereas negative $\Delta\phi$ indicate repulsive forces.

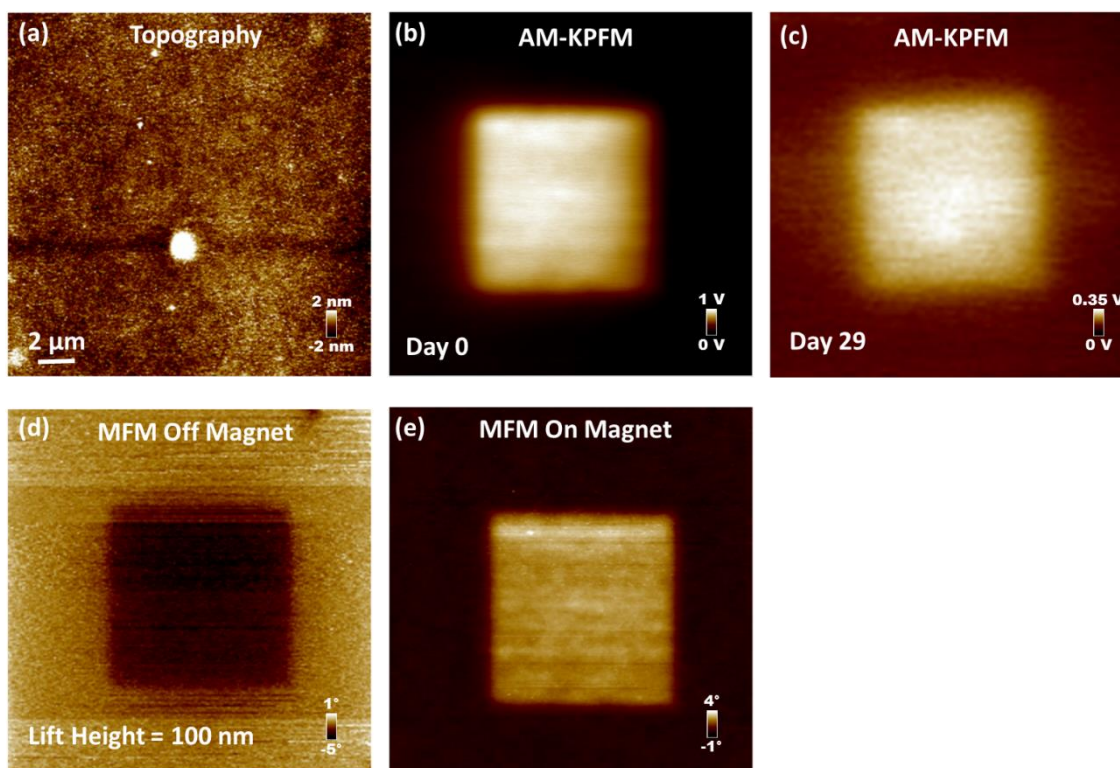


Fig. 5-1: Triboelectric study done on PMMA, (a) the topography of the region after the charges have been generated, AM-KPFM results (b) after generating charges and (c) after 29 days of charge generation. The MFM results of the charged area (d) without magnetic field and (e) with a magnetic field after generating charges. Both AM-KPFM and MFM images were captured at a lift height of 100 nm.

Fig. 5-1a shows the topography of the region after the charges have been created. It should be noted that there were no signs of material transfer. KPFM and MFM study was conducted for several days. The charge generation can be clearly seen from KPFM image (Fig. 5-1b). As mentioned in Chapter 2 and 3, positive charges were generated during triboelectric charging. Since radicals were supposed to be paramagnetic, MFM study was conducted under two different conditions: in the absence and presence of magnetic field as shown in Fig. 5-1d-e. The shift in the phase clearly suggests the presence of radicals on the surface. Interestingly, it was observed that in absence of magnetic field the interaction was repulsive. Thus, suggesting that even at room

temperature, M_z of radicals were oriented in opposite direction to that of MFM tip. As stated earlier, both mechano-radicals and charges were observed in the same region³⁵.

It should be noted from Eq. 5-5 that both electrostatic and magneto-static forces are the function of the z position of the cantilever from the surface. It was observed that the interaction force decreases as z increases (Fig. 5-2a). It was interesting to note that when no magnetic field was applied, $\Delta\phi$ had lot of wiggles and the noise in $\Delta\phi$ was very high. It has been reported that noise and wiggles can be observed due to electrostatic interaction¹⁷⁶. When the sample was placed in a magnetic field, the noise reduced and the $\Delta\phi$ as a function of z was found to decrease smoothly.

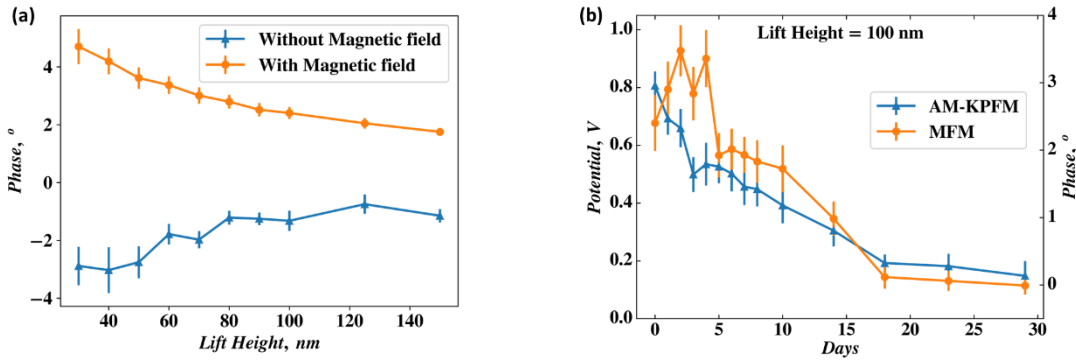


Fig. 5-2: (a) MFM signal as a function of different lift height in presence and absence of an external magnetic field, (b) Evolution of surface potential and MFM signal as a function of time. MFM results were taken in presence of magnetic field.

The stability of mechano-radicals was also examined (Fig. 5-2b). It was found that the generated mechano-radicals are stable for an extremely long period of time. Interestingly, for initial few days, it was found that $\Delta\phi$ increased whereas the surface potential decreased. The decrease in surface potential will lead to decrease in $\partial F_{elec}/\partial z$. Therefore the increase in $\Delta\phi$ can only be attributed to increase in radical density. The radicals and charges might generate during topographic imaging done with KPFM and MFM⁵⁰. However, A_0 during topographic imaging was between 22-25 nm and $A_{setpoint}$ was around 17-20 nm. It was noted that surface potential and MFM signal of the uncharged region does not change. The increase in radicals' density may be due to the combination of the excess electrical charges³⁶. The generation of mechano-radicals is an endothermic process.

In case of triboelectric charging, this energy could be supplied from the neutralization of the triboelectric charges. For initial few days, surface charges were observed to decay faster. Hence, the rate of radical generation could be higher compared to their recombination rate. The source of negative charges for neutralizing triboelectric charge is assumed to come from atmospheric ions⁹. These observations indicate that the total number of radicals observed from MFM might not have generated during contact and dissipation of triboelectric charges could leave the radicals behind. These newly generated radicals cannot be termed as mechano-radicals since their origin is not associated with homolytic scission of the polymer chain.

However, after 5 days $\Delta\phi$ decreased drastically. One possible reason for such a steep decrease could be the recombination of the radicals. It is well known that stability of radicals depend upon its concentration¹⁶⁴. From Fig. 5-2b, one can see that a dip in $\Delta\phi$ is there on day 3 for similar value of $\Delta\phi$ on day 2. Therefore, after certain concentration of radicals, they might tend to recombine with each other. Also, after 5 days, both surface potential and $\Delta\phi$ decay in a similar manner suggesting that the rate of radical generation and recombination could be equal. The decrease in radical generation rate can again be attributed to the decreasing rate of charge dissipation. These observations clearly suggest that more radicals are generated as triboelectric charges are dissipated. The decrease in charge dissipation rate may be due to stabilization of the charges with the radicals³⁵. Therefore, when excessive radicals are generated during triboelectric charging they recombine leaving charges to dissipate faster whereas when they are present in optimum amount, they stabilize the charges. It has been demonstrated that by introducing radical scavengers static charges from electronic circuits can be eliminated³⁵. Interestingly, the phase shift of the cantilever was also found to be near 0° after 18 days i.e., there were no interaction force between tip and sample. From KPFM results, it is evident that surface charges were present. Hence, F_{elec} exist between tip and sample which is always attractive. Therefore, from Eq. 5-5, for $\Delta\phi = 0$, the magnetic interaction should be repulsive. The above discussion suggests that for higher performance of TENG devices, optimum amount of mechano-radicals should be generated and their further generation due to charge recombination should be prohibited. In Chapter 2, it was noticed that the amount of charge generated decreased for 0.25 kHz compared to 0.5 and 1 kHz. One of the reason could be the generation of more mechano-radicals at longer contact times. This hypothesis is further supported by the fact that total energy dissipated at 0.25 kHz was way higher

than 0.5 and 1 kHz. These observations are significant as they provide another way to control the generation of mechano-radicals.

One of the mechanisms proposed for the charge dissipation during triboelectric effect is the diffusion of charges on the surface²³. However, in the present study no diffusion of surface charges was observed (Fig. 1 b,c). One reason could be lower RH during the experiment (RH = 15-30%). Similar observations were made at higher RH. Therefore, RH might not be the reason for low diffusivity of charges. From the above discussion, it should be noticed that charge dissipation resulted in radical generation. The chemical characteristics of these radicals are suggested to be similar to C-C bond scission of main polymer chain³⁶. The probability of finding broken C-C bond will be much higher in the charged region. Hence, these radicals might prevent triboelectric charges to diffuse away.

5.4 Radical Polymer and TENG characterization

5.4.1 Characterization of Radical Polymer

FTIR spectra of PTMPM and PTMA are given in Fig. 3a. FTIR spectra were collected by making a pellet of the polymer and KBr. The absence of C=C peak at 1634 cm^{-1} suggest the completion of polymerization reaction from Scheme 1. Also, the absorption peak at 1705 and 3400 cm^{-1} is due to C=O and N-H bonds respectively¹⁷⁸. Due to some unknown reason N-O· at 1362 cm^{-1} was observed with PTMPM. However, after oxidation, 3400 cm^{-1} peaks disappear and only 1362 cm^{-1} peak was present^{178,179}. Hence, the oxidation reaction, Scheme 2, is also complete.

In order to confirm that the resulting polymer has N-O· radical, cyclic voltammetry and electron paramagnetic resonance (EPR) studies were performed. The redox potential of PTMA is reported to be around $3.58\text{ V vs. Li/Li}^+$ ¹⁶⁹. As seen from cyclic voltammetry result, Fig. 5-3b, the redox potential is very near to the reported value.

EPR spectra of TEMPOL and PTMA are given in Fig. 5-3c, d respectively. From EPR spectra, it is clear that the polymer contains N-O·¹⁶⁹. Also, the EPR spectrum of the polymer is broad and only one peak appears compared to three peaks in TEMPOL. This might be due to the dipole-dipole interaction between polymer bound radical sites¹⁸⁰.

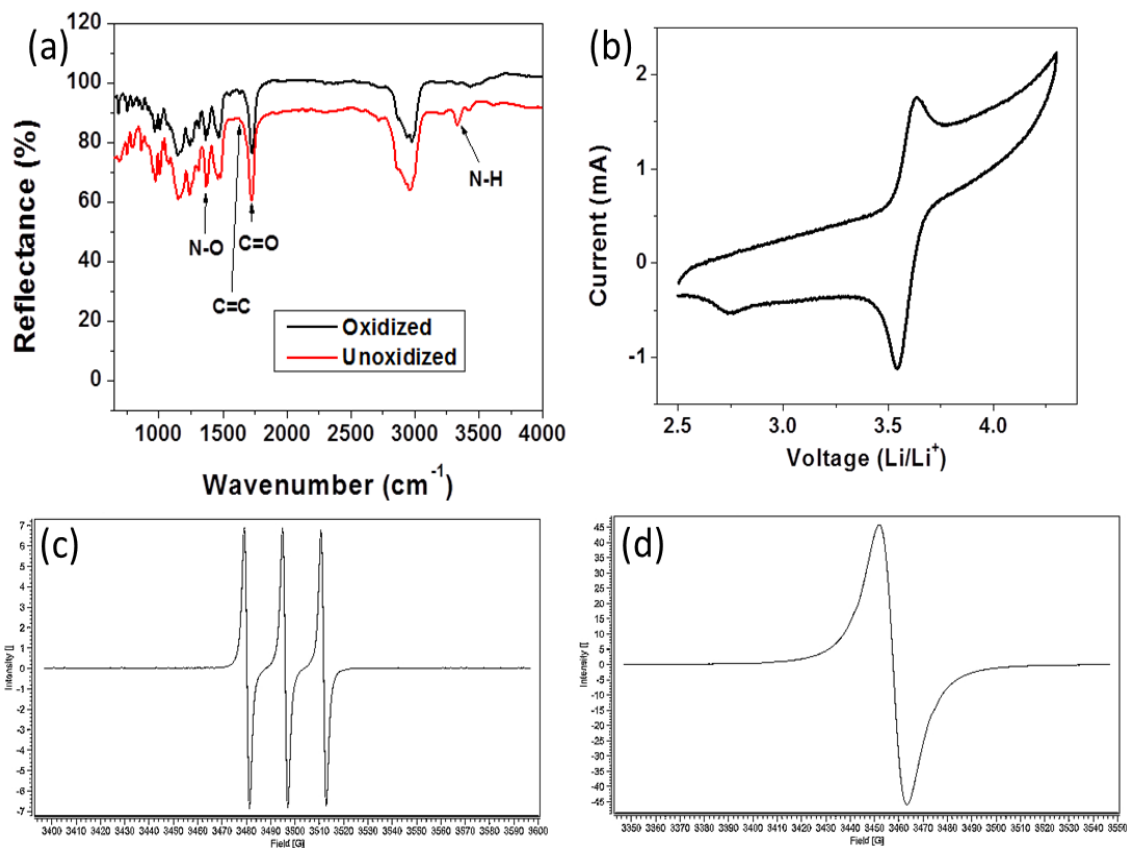


Fig. 5-3: Characterization of radical polymer (a) FTIR spectra of PTMA and PTMPM polymer, (b) Cyclic Voltammetry of radical polymer, (c) EPR spectra of TEMPOL, (D) EPR spectra of radical polymer, PTMA

5.4.2 TENG Study

The chemical structure of PTMA and PTMPM has Nitrogen based functional group. It has been reported that these functional groups mostly generates positive charges¹⁷. During the initial sets of reading, it was also noted that the positive side of triboelectric series does not produce significant charges. Therefore, from triboelectric series, FEP was selected as another dielectric which develops negative charges¹⁸¹. The negative lead of the electrometer was connected to the FEP film. Before starting the experiment, extraneous charges from the polymers were removed by cleaning the films. It was noticed that cleaning procedure had a huge influence on triboelectric charge

generation. Therefore, TENG study was conducted with two different cleaning procedures as described in experimental section. Open circuit voltage (V_{OC}) and short circuit current (I_{SC}) of PTMA film cleaned with water and ethanol is shown in Fig. 5-4a,b. From Fig. 5-4a, more than threefold increase in V_{OC} can be noticed with different cleaning procedures. The charge density (σ_{SC}) was calculated by integrating current over time i.e., $\sigma_{SC} = \int_{t=t_0}^t I_{SC} dt / S$, where S is the area of a TENG device. V_{OC} and σ_{SC} for PTMA, PTMPM and PMMA is shown in Fig. 5-4c,d. It is expected that during ethanol cleaning, some organic contaminants would have been washed away. Hence, slight increase in V_{OC} and σ_{SC} was observed for PTMPM and PMMA sample. However, more than threefold increase in V_{OC} and σ_{SC} for PTMA film cannot be explained by washing away of organic contaminant. As already pointed out, PTMA contains N-O \cdot radicals which can store and transfer charges via self-exchange reaction. It has been suggested that since PTMA is not hydrophilic, its functionality in aqueous system might be limited¹⁸². Interestingly, it was observed that V_{OC} and σ_{SC} for water cleaned PTMA were similar to PTMPM results. Hence, further experiments were conducted to understand the difference in charging mechanism between PTMA and PTMPM.

XPS studies were done for both water and ethanol cleaned PTMA and PTMPM (Fig. 5-5). The binding energy of N-H, N-O \cdot and +N=O has been reported to be around 399.8, 401.3 and 405.6 eV¹⁸³. The peaks from XPS were found to be around similar values. From XPS result, it was noticed that few N-H bonds were present even in PTMA. Together with N-O \cdot and N-H, +N=O bonds were also observed in PTMA. As discussed during polymer synthesis, oxidation was done for 6 hrs. For this oxidation time, increase in the +N=O bond has been reported¹⁸³. An increase in N-O \cdot density was observed for ethanol cleaned PTMA and PTMPM samples. Although these results might suggest that increase in N-O \cdot density resulted in increased charge generation. However, the increase in σ_{SC} for ethanol cleaned PTMPM samples were not as significant as ethanol cleaned PTMA. It should be noted that depth resolution of XPS is reported to be maximum of 10 nm¹⁸⁴ whereas the both films were 450 ± 50 nm thick. Therefore, in case PTMPM, N-O \cdot might be present on the surface. Since N-O \cdot can store charges, ethanol cleaned PTMA might have higher charge storage density compared to PTMPM.

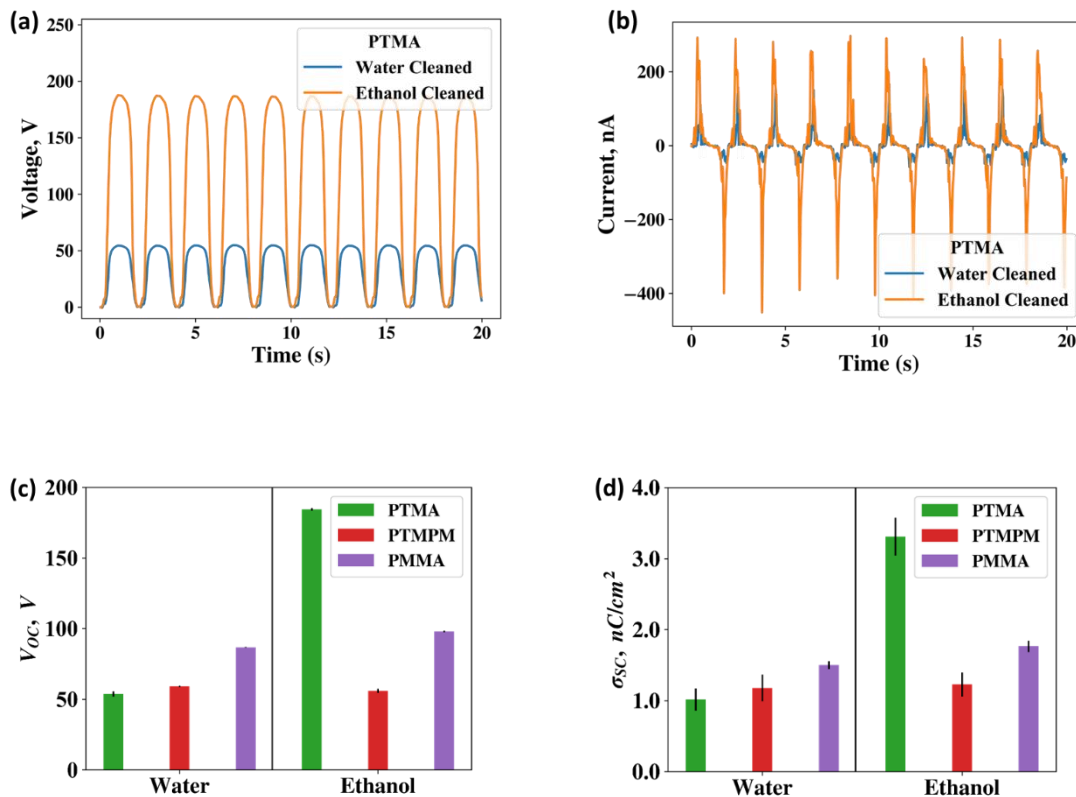


Fig. 5-4: TENG characterization of PTMA, (a) Voltage, (b) current as a function of time for water and ethanol cleaned sample. The compiled result of (c) V_{OC} , and (d) σ_{SC} for PTMA, PTMPM and PMMA for different cleaning procedure.

CV was performed (Fig. 5-6) to understand the charge storage and reaction kinetics in these films. For PTMA, CV was found to be significantly different compared to Fig. 5-3a. No cathodic peak potential could be observed for both water and ethanol cleaned PTMA samples. The anodic peak potential was found to be different for these samples. The current density for both the films appears to be similar. These observations suggest that the overall N-O \cdot density is similar for both the film but their reaction rate were slow and had a different magnitude. The probable reason may be change in the topography of PTMA during cleaning which will be discussed later. Electrochemical reactions were also observed for ethanol cleaned PTMPM. Again, like PTMA the cathodic and anodic reaction peak potential was not clear due to slow reaction rate. However, no electrochemical activity was observed for water cleaned PTMPM despite the small amount of N-O \cdot . From Fig.

5-4c,d, a negligible increase in σ_{SC} for ethanol cleaned PTMPM was observed. Therefore, the presence of N-O \cdot in PTMPM does not seem to be participating during the triboelectric effect. This implies that the increased charge density for ethanol cleaned PTMA may not be due to increased N-O \cdot density.

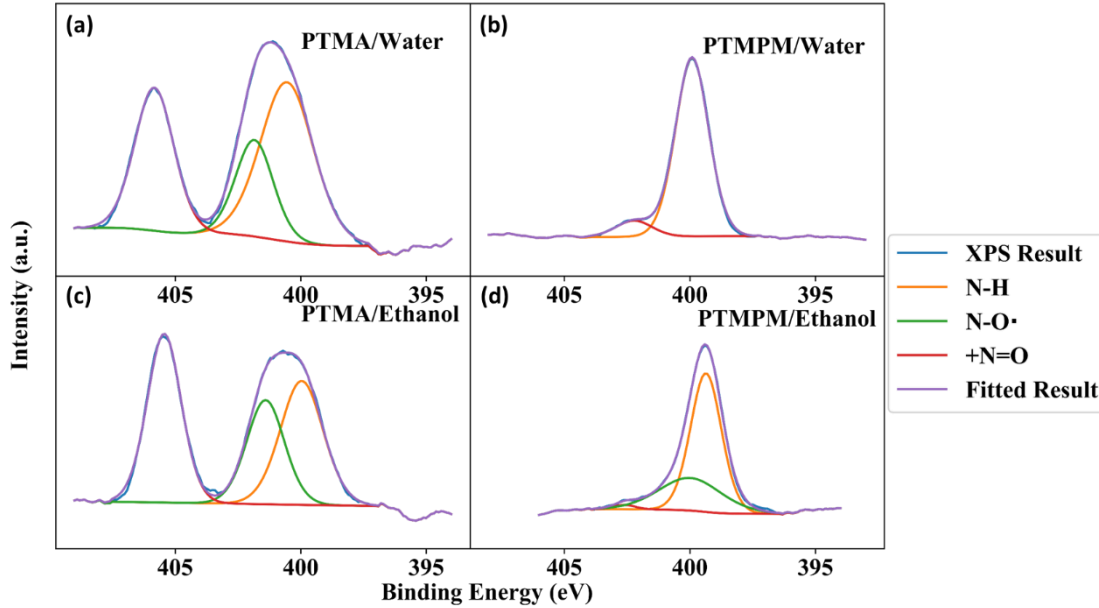


Fig. 5-5: XPS spectra of N1s for (a) PTMA, (b) PTMPM cleaned with water. (c) PTMA, (d) PTMPM cleaned with ethanol. The peak fitting for different chemical bonds and the fitted results are given in the legend.

During CV experiment the weight of the polymer was decreased after cleaning with ethanol. Therefore, the solubility of both polymers in ethanol was checked. It was found that PTMPM dissolved slightly more than PTMA. However, ethanol cleaning did not dissolve the films completely. Therefore, the topography of these films was also examined from AFM. It was noticed that both water cleaned films had similar topography (Fig. 5-7a,b). However, after ethanol cleaning, the topography changes. In case of PTMPM, even though topography did not change significantly, few nano-structures developed (Fig. 5-7c). However, for ethanol cleaned PTMA film topography changed completely (Fig. 5-7d). The roughness of these films was drastically increased. For water cleaned PTMA sample, calculated average roughness (R_a) was 0.3-0.4 nm,

whereas ethanol cleaned PTMA had R_a of 10-14 nm. It has been reported that PTMA and ethanol has Upper Critical Solution Temperature (UCST)¹⁸⁵ behavior where PTMA dissolves in ethanol at high temperature. Similar observations were made when temperature of PTMA and ethanol was raised to 30-35°C. Therefore, the increased surface roughness could be due to UCST behavior of PTMA and ethanol at room temperature. It has been reported that surface roughness or nanostructure increases the triboelectric surface charge density¹⁸⁶. The increased V_{OC} and σ_{SC} of ethanol cleaned PTMA may be a result of the increased roughness rather than an increase in N-O· density.

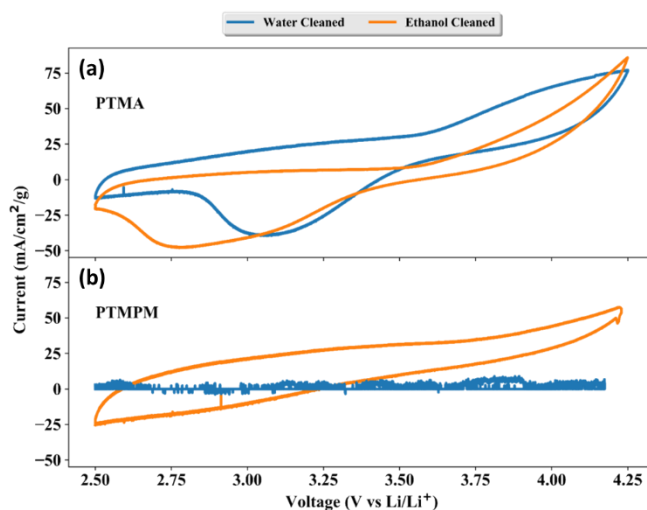


Fig. 5-6: CV of PTMA and PTMPM cleaned with water and ethanol. The blue color indicates the result obtained by water cleaning and orange color for ethanol cleaned samples.

From the above discussion, it is evident that N-O· might not be participating during triboelectric charging. However, positive charges were generated on both PTMA and PTMPM and their origin is still not clear. Therefore, to understand the origin of the charges, DFT calculations were performed for monomer (TMA and TPM) using Gaussian 09 software. The computation was performed using hybrid B3LYP and 6-31+G* basis set¹⁸⁷. For the computation, the double bond of the methacrylate was replaced by H bond. To understand the reaction sites, electrostatic potential of TPM and TMA are shown in Fig. 5-8. The red indicates negative potential i.e., electron density in this area is higher. Blue regions indicate positive charges or areas with less

electron density. Green is nearly neutral potential. As expected, N-O· molecules have very high electron density whereas N-H has very small electron density. Therefore, higher charge density was expected for PTMA. However, no such observations were noticed in Fig. 5-4c,d. One possible reason could be the steric hindrance due to methyl group surrounding N-O·.

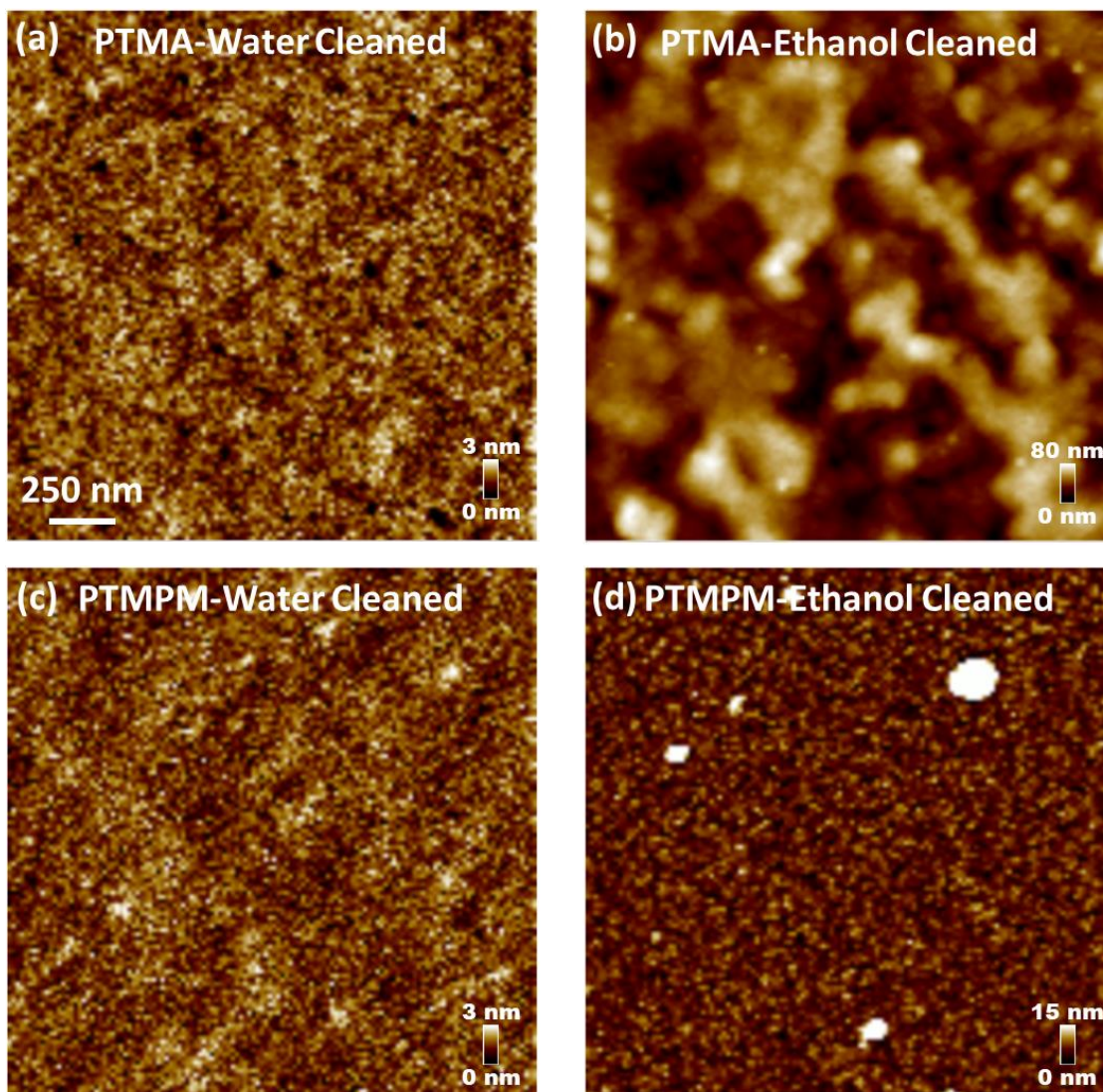


Fig. 5-7: Topography of PTMA after cleaning with (a) water and (b) ethanol. Similarly, the topography of PTMPM after cleaning with (c) water and (d) ethanol.

Another region which has a very high concentration of electrons in both molecules is associated with ester group ($\text{O}-\text{C}=\text{O}$). In fact, it can be noticed that there is resonance associated with an ester

group, suggesting that it might participate in triboelectrification. Considering the results shown in Fig. 5-4c,d, it seems very likely that these charges originated from this functional group. This is again supported by the fact that PMMA also develops more positive charge (Fig. 5-4c,d). The reason for more positive charge on PMMA will be discussed later. The origin of triboelectric charges from ester group of PMMA has been reported¹⁸⁸. Also, due to the steric hindrance, charges from the ester group might not be transferred to N-O· and, hence, the activity of N-O· could not be observed. Also, the charge generation mechanism during triboelectric charging is quite complex. Here we have only considered the electrostatic potential of monomer and ignored interactions with other molecules and charges such as H_3O^+ and OH^- ions in the calculation.

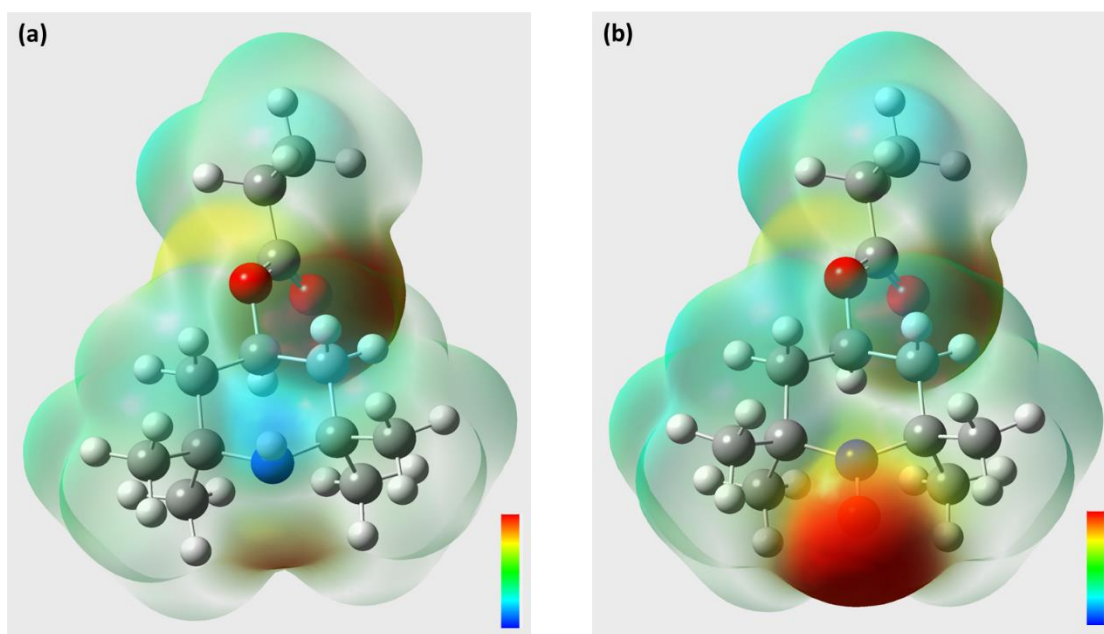


Fig. 5-8: Electrostatic potential map of (a) TPM and (c) TMA determined from DFT calculation.

It was implied from the above discussion that the bulky molecules surrounding N-O· decreased its reactivity and, hence, prevented ester group from participating in triboelectric effect. It should be noted that for ester group, one side is also surrounded by bulky TEMPO or its derivative group. Therefore, the reactivity at ester center might also decrease. The CH_3 group together with ester group in PMMA is significantly smaller in size than TEMPO and its derivative group in PTMA

and PTMPM. It was found that the amount of the produced charge increased for PMMA (Fig. 5-4c,d). These observations clearly suggest that ester group is mainly responsible for triboelectric charging and its reactivity also depends upon the adjacent groups. The dependence of RH on the triboelectric charging of PMMA was discussed in Chapter 2, the interaction of H₂O molecule with ester can alter their reactivity. Hence, more understanding is required for the processes happening at the interface together with the first principle calculations. Therefore, the TENG material should be designed in such a way that the functional group participating during triboelectric effect is bonded with smaller groups so that they are easily accessible during the triboelectric interaction.

5.5 Conclusion

In this chapter, we discussed the role of mechano-radical generation during triboelectric charging. A co-dependence between radicals and charges were noticed. We found that the rate of radical generation after triboelectric charging depends on their concentration and triboelectric charge dissipation rate. Also, radicals seem to prevent diffusion of triboelectric charges by interacting with them and lowering their potential.

We evaluated the TENG performance of radical containing films. It was noticed that the radicals do not participate during triboelectric charging due to steric hindrance. The importance of structural and molecular design was discussed. It was shown that triboelectric charge generation depends upon the availability of the reaction site and how easily they are accessible during the process. Also, how the performance of TENG can be enhanced by introducing nano-structures was demonstrated.

6 Summary and Future Work

6.1 Summary:

In this thesis, we studied in detail the triboelectric charging mechanism on PMMA substrate. There are several factors which can influence the triboelectric charge generation. With the help of Taguchi Design, we minimized the influence of external factors, which were not taken into account. It was found that all the parameters except number of contacts had a significant influence on triboelectric charge generation. We noticed that the amount of the generated charge increased with RH. Also, the kinetics of the charge transfer across the interface suggested consecutive reactions. The first reaction seems to generate ions, whereas the second reaction might have started after the ions have been generated as it leads to decrease in charge density. Due to the competing nature of the reactions, a time constant was observed where the maximum amount of charges could be generated. The decrease in charge density at longer contact time was proposed, due to the diffusion of counter-ions at the interface. Interestingly, it was found that the observed time constant coincides with Debye relaxation of ice that occurs due to recombination of H_3O^+ ions and OH^- ions. Since positive surface charges were produced during triboelectric charging, it was assumed that diffusion of OH^- ions might result in a decrease in the surface charge. This assumption was further supported by the fact that the diffusion rate of both H_3O^+ ions and OH^- ions differ by a factor of 2. Since water molecules seem to be playing an important role, we investigated their presence during triboelectric charging. We noticed from the phase imaging that water molecules were present near the charged region. Also, their amount increases with an increasing RH. As it has been well established that the first few layers of water at an interface have an ice-like property, it was concluded that the ice-like stern layer might be playing an important role during triboelectric charging.

Although the observed trend in charge transfer kinetics could be explained by the presence of water molecule, the energy dissipated across the interface had anomalous behavior. There was no specific trend observed between energy dissipation and contact time but at longer contact time energy dissipation was significantly higher whereas charge generation decreased. It is reported that radicals are generated during triboelectric charging. Therefore, the anomaly in the energy

dissipation could be due to the generation of acoustic phonon at longer contact time or other chemical processes, such as radical generation at the interface. When the generation and stability of radicals were studied, it was noticed that as the charges dissipate, more radicals are produced. This observation led us to propose that charges might dissipate with longer contact time leaving behind more radicals which might consume more energy.

Since the generation of radicals consumes more energy during contact, we studied the influence of pre-existing radicals during triboelectric charging. If radicals are present beforehand, we expected that most of the energy will be consumed in generating charges rather than radicals. However, it was found that there was no difference if the polymer had pre-existing radicals (PTMA) or not (PTMPM). We proposed that the radicals do not participate in triboelectric charging due to steric hindrance. The DFT calculation shows that these polymers have another reaction center (O-C=O bond) where the charges were assumed to be created. The backbone of PTMA, PTMPM, and PMMA are similar and only the side chain is different. In case of PTMA and PTMPM, the assumed reaction center was surrounded by a bigger molecule which can act as steric hindrance and, thus, reduce its reactivity. Therefore, TENG studies were also done on PMMA, in which reaction center is surrounded by smaller molecules and, thus, reduces the steric hindrance. We found that the amount of triboelectric charge increased for PMMA, suggesting that the molecular design of polymer should be considered to achieve higher performance of TENG devices. Specifically, it was proposed that easy accessibility of the reaction center could give higher charge density. Interestingly, the assumed reaction center has hydrophilic property. Therefore, the observed dependence of RH on the triboelectric charge could be due to the interaction between carbonyl and water molecule.

6.2 Future Work:

We now have a clear understanding of the involvement of ions and radicals in the charge generation process but the type of ions and radicals were not specified. The future work will be dedicated to understanding the chemical characteristics to highlight the ion and radical generation mechanisms and energies involved in the reaction. Although there are several techniques such as XPS that can probe the surface chemistry, most of these techniques are based on Ultrahigh Vacuum. It is important to note that the chemical composition of several materials can be probed by Infra-red (IR) spectroscopy. Since the surface charges are created during triboelectric charging,

the dipole moment and polarizability of the molecule will change due to the electric field created by the surface charges. Therefore, vibrational stark spectroscopy (VSS) can be employed to understand various chemical aspects of triboelectric charges. To ascertain the applicability of the VSS, experiments were conducted on Kapton film. We were able to create opposite charges using Teflon and Al film. The shift in the vibrational energy of various chemical bonds was monitored by Thermo Scientific FTIR instrument (using PIKE Variable Angle setup). The experimental results are shown in Fig. 1. It should be noted that most of the signal was from the bulk of the Kapton film. However, the shift in chemical bonds vibration energy is supposed to arise only from a space charge region. The thickness of the space charge region is supposed to be very small compared to the thickness of Kapton film. Therefore, the difference in absorbance for uncharged and charged Kapton film was very small. Also, since the majority of the signal arose from the bulk of the film, the ions/radicals generated at the interface could not be probed. However, the above result suggests that these charges can be monitored by FTIR, which can also provide the chemical information. This kind of approach can be used as a characterization tool for investigating triboelectric charging in ambient conditions. The resolution and depth of penetration for VSS study can be improved by employing near-field scanning optical microscopy (NSOM) based AFM-IR technique. In case of AFM-IR, a very high resolution can be achieved with a very small penetration depth (~50 – 100 nm). This might enhance the signal from the space charge region, and the ions/radicals generated on the surface could be probed.

Also, it should be noted that we discussed the steric hindrance and the interaction with water molecule, etc. in the thesis. It is also suggested that the reaction energy changes due to these different aspect. Therefore, if the understanding from AFM-IR could be combined with the results discussed in this thesis, it can provide insight into various chemical reactions and energy and the favorable conditions required for those reactions.

Once the chemical reactions and the required energy are understood, different polymers can be explored to further probe the mechanisms for charge generation occurring at the interface. These mechanisms will provide a better insight into various processes that can occur during triboelectric effect, and help in the material selection that can result in far better and reliable TENG devices for practical application. Also, several other applications might be discovered from these studies.

Finally, as noticed before, the parasitic capacitance can significantly decrease the performance of TENG devices. Hence, ways to reduce parasitic capacitance need to be explored.

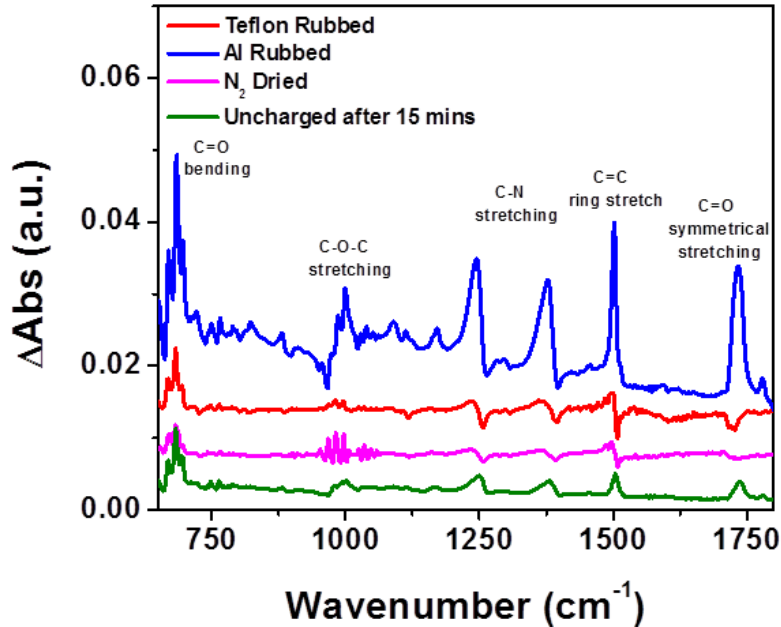


Fig. 6-1: Vibrational Stark Spectroscopy (VSS) of Kapton film. The controlled experiment was done without creating charges in two different ways. In the 1st case, FTIR spectra of the uncharged film were taken at an interval of 15 mins. A very small change in Absorbance values was observed. In the 2nd case, FTIR spectra were collected before and after N₂ drying. Again, very small changes were observed in absorbance value. When the charges were deposited on Kapton by rubbing with Al and Teflon film, more change in absorbance was noticed. Also from single electrode TENG study (result not shown), it was found that Al produced fewer charges compared to Teflon. Therefore, the higher shift in absorbance of Kapton film after rubbing with Teflon suggest that space charge region can be probed by FTIR spectroscopy.

Reference

1. IEA. *Energy Technology Perspectives 2016*. (Organisation for Economic Co-operation and Development, 2016).
2. OECD. *The Internet of Things*. (Organisation for Economic Co-operation and Development, 2016).
3. Wang, Z. L., Chen, J. & Lin, L. Progress in triboelectric nanogenerators as a new energy technology and self-powered sensors. *Energy Environ. Sci.* **8**, 2250–2282 (2015).
4. Boisseau, S., Despesse, G. & Seddik, B. A. Electrostatic Conversion for Vibration Energy Harvesting. (2012). doi:10.5772/51360
5. Wang, Z. L. On Maxwell's displacement current for energy and sensors: the origin of nanogenerators. *Mater. Today* **20**, 74–82 (2017).
6. Trimmer, W. S. N. Microrobots and micromechanical systems. *Sens. Actuators* **19**, 267–287 (1989).
7. Zi, Y. *et al.* Harvesting Low-Frequency (<5 Hz) Irregular Mechanical Energy: A Possible Killer Application of Triboelectric Nanogenerator. *ACS Nano* **10**, 4797–4805 (2016).
8. Moore, A. D. *Electrostatics and its applications*. (John Wiley & Sons, Inc., 1973).
9. Harper, W. R. *Contact and frictional electrification*. (Clarendon P., 1967).
10. McCarty, L. S. & Whitesides, G. M. Electrostatic Charging Due to Separation of Ions at Interfaces: Contact Electrification of Ionic Electrets. *Angew. Chem. Int. Ed.* **47**, 2188–2207 (2008).
11. Wang, S. *et al.* Maximum Surface Charge Density for Triboelectric Nanogenerators Achieved by Ionized-Air Injection: Methodology and Theoretical Understanding. *Adv. Mater.* **26**, 6720–6728 (2014).
12. Fan, F.-R., Tian, Z.-Q. & Lin Wang, Z. Flexible triboelectric generator. *Nano Energy* **1**, 328–334 (2012).
13. Wang, Z. L. Triboelectric Nanogenerators as New Energy Technology for Self-Powered Systems and as Active Mechanical and Chemical Sensors. *ACS Nano* **7**, 9533–9557 (2013).
14. Zheng, Q., Shi, B., Li, Z. & Wang, Z. L. Recent Progress on Piezoelectric and Triboelectric Energy Harvesters in Biomedical Systems. *Adv. Sci.* **4**, (2017).
15. Yang, P.-K. *et al.* Paper-Based Origami Triboelectric Nanogenerators and Self-Powered Pressure Sensors. *ACS Nano* **9**, 901–907 (2015).
16. Dai, K. *et al.* Simulation and structure optimization of triboelectric nanogenerators considering the effects of parasitic capacitance. *Nano Res.* **10**, 157–171 (2017).
17. Diaz, A. F. & Felix-Navarro, R. M. A semi-quantitative tribo-electric series for polymeric materials: the influence of chemical structure and properties. *J. Electrostat.* **62**, 277–290 (2004).
18. Lowell, J. Charging of bulk states in semiconductors and insulators in contact with metals. *J. Electrostat.* **8**, 161–169 (1980).
19. Gibson, H. W. Linear free energy relationships. VIII. Ionization potentials of aliphatic compounds. *Can. J. Chem.* **55**, 2637–2641 (1977).
20. Cui, X. D. *et al.* Bias-induced forces in conducting atomic force microscopy and contact charging of organic monolayers. *Ultramicroscopy* **92**, 67–76 (2002).
21. Lambert, J., Saint-Jean, M. & Guthmann, C. Contact electrification of high-K oxides studied by electrostatic force microscopy. *J. Appl. Phys.* **96**, 7361–7369 (2004).

22. Zhou, Y. S. *et al.* Manipulating Nanoscale Contact Electrification by an Applied Electric Field. *Nano Lett.* **14**, 1567–1572 (2014).
23. Zhou, Y. S. *et al.* In Situ Quantitative Study of Nanoscale Triboelectrification and Patterning. *Nano Lett.* **13**, 2771–2776 (2013).
24. Zhou, Y. S., Li, S., Niu, S. & Wang, Z. L. Effect of contact- and sliding-mode electrification on nanoscale charge transfer for energy harvesting. *Nano Res.* **9**, 3705–3713 (2016).
25. Grzybowski, B. A., Fialkowski, M. & Wiles, J. A. Kinetics of Contact Electrification between Metals and Polymers. *J. Phys. Chem. B* **109**, 20511–20515 (2005).
26. Burgo, T. A. L., Silva, C. A., Balestrin, L. B. S. & Galembeck, F. Friction coefficient dependence on electrostatic tribocharging. *Sci. Rep.* **3**, (2013).
27. Waitukaitis, S. R., Lee, V., Pierson, J. M., Forman, S. L. & Jaeger, H. M. Size-Dependent Same-Material Tribocharging in Insulating Grains. *Phys. Rev. Lett.* **112**, 218001 (2014).
28. Williams, M. W. Triboelectric charging of insulating polymers—some new perspectives. *AIP Adv.* **2**, 010701 (2012).
29. Diaz, A. F. Contact Electrification of Materials: The Chemistry of Ions on Polymer Surfaces. *J. Adhes.* **67**, 111–122 (1998).
30. Diaz, A. F. & Fenzel-Alexander, D. An ion transfer model for contact charging. *Langmuir* **9**, 1009–1015 (1993).
31. Diaz, A., Fenzel-Alexander, D., Wollmann, D. & Barker, J. A. Importance of dissociated ions in contact charging. *Langmuir* **8**, 2698–2706 (1992).
32. Baytekin, H. T. *et al.* The Mosaic of Surface Charge in Contact Electrification. *Science* **333**, 308–312 (2011).
33. Galembeck, F. *et al.* Friction, tribochemistry and triboelectricity: recent progress and perspectives. *RSC Adv.* **4**, 64280–64298 (2014).
34. Baytekin, B., Baytekin, H. T. & Grzybowski, B. A. What Really Drives Chemical Reactions on Contact Charged Surfaces? *J. Am. Chem. Soc.* **134**, 7223–7226 (2012).
35. Baytekin, H. T., Baytekin, B., Hermans, T. M., Kowalczyk, B. & Grzybowski, B. A. Control of Surface Charges by Radicals as a Principle of Antistatic Polymers Protecting Electronic Circuitry. *Science* **341**, 1368–1371 (2013).
36. Sakaguchi, M. & Sohma, J. Anomalous Decay Behavior of the Polypropylene Radicals Produced by Mechanical Fracture: Effect of the Excess Charges Due to Triboelectricity. *Polym. J.* **7**, 490–497 (1975).
37. Sakaguchi, M. *et al.* Triboelectricity in polymers: effects of the ionic nature of carbon–carbon bonds in the polymer main chain on charge due to yield of mechano-anions produced by heterogeneous scission of the carbon–carbon bond by mechanical fracture. *J. Electrostat.* **62**, 35–50 (2004).
38. Rezende, C. A., Gouveia, R. F., Silva, M. A. da & Galembeck, F. Detection of charge distributions in insulator surfaces. *J. Phys. Condens. Matter* **21**, 263002 (2009).
39. Wiles, J. A., Fialkowski, M., Radowski, M. R., Whitesides, G. M. & Grzybowski, B. A. Effects of Surface Modification and Moisture on the Rates of Charge Transfer between Metals and Organic Materials. *J. Phys. Chem. B* **108**, 20296–20302 (2004).
40. Wählin, A. & Bäckström, G. Sliding electrification of Teflon by metals. *J. Appl. Phys.* **45**, 2058 (1974).
41. Fan, F.-R., Tian, Z.-Q. & Lin Wang, Z. Flexible triboelectric generator. *Nano Energy* **1**, 328–334 (2012).

42. Wiles, J. A., Grzybowski, B. A., Winkleman, A. & Whitesides, G. M. A Tool for Studying Contact Electrification in Systems Comprising Metals and Insulating Polymers. *Anal. Chem.* **75**, 4859–4867 (2003).
43. Ducati, T. R. D., Simões, L. H. & Galembeck, F. Charge Partitioning at Gas–Solid Interfaces: Humidity Causes Electricity Buildup on Metals. *Langmuir* **26**, 13763–13766 (2010).
44. Shinohara, I., Yamamoto, F., Anzai, H. & Endo, S. Chemical structure and electrostatic properties of polymers. *J. Electrostat.* **2**, 99–110 (1976).
45. Castle, G. S. P. Contact charging between insulators. *J. Electrostat.* **40–41**, 13–20 (1997).
46. Németh, E., Albrecht, V., Schubert, G. & Simon, F. Polymer tribo-electric charging: dependence on thermodynamic surface properties and relative humidity. *J. Electrostat.* **58**, 3–16 (2003).
47. Baytekin, H. T., Baytekin, B., Incorvati, J. T. & Grzybowski, B. A. Material Transfer and Polarity Reversal in Contact Charging. *Angew. Chem. Int. Ed.* **51**, 4843–4847 (2012).
48. HONEGGER, E. & Henry, P. S. H. Generation of Static on Solid Insulators. *J. Text. Inst. Proc.* **48**, P5–P25 (1957).
49. Apodaca, M. M., Wesson, P. J., Bishop, K. J. M., Ratner, M. A. & Grzybowski, B. A. Contact Electrification between Identical Materials. *Angew. Chem. Int. Ed.* **49**, 946–949 (2010).
50. Li, S., Zhou, Y., Zi, Y., Zhang, G. & Wang, Z. L. Excluding Contact Electrification in Surface Potential Measurement Using Kelvin Probe Force Microscopy. *ACS Nano* **10**, 2528–2535 (2016).
51. Medley, J. A. The electrostatic charging of some polymers by mercury. *Br. J. Appl. Phys.* **4**, S28 (1953).
52. Clint, J. H. & Dunstan, T. S. Acid-base components of solid surfaces and the triboelectric series. *Europhys. Lett.* **54**, 320–322 (2001).
53. Gouveia, R. F., Bernardes, J. S., Ducati, T. R. D. & Galembeck, F. Acid–Base Site Detection and Mapping on Solid Surfaces by Kelvin Force Microscopy (KFM). *Anal. Chem.* **84**, 10191–10198 (2012).
54. Baytekin, H. T., Baytekin, B., Soh, S. & Grzybowski, B. A. Is Water Necessary for Contact Electrification? *Angew. Chem. Int. Ed.* **50**, 6766–6770 (2011).
55. Burgo, T. A. de L., Rezende, C. A., Bertazzo, S., Galembeck, A. & Galembeck, F. Electric potential decay on polyethylene: Role of atmospheric water on electric charge build-up and dissipation. *J. Electrostat.* **69**, 401–409 (2011).
56. Santos, L. P., Ducati, T. R. D., Balestrin, L. B. S. & Galembeck, F. Water with Excess Electric Charge. *J. Phys. Chem. C* **115**, 11226–11232 (2011).
57. Bernardes, J. S., Rezende, C. A. & Galembeck, F. Electrostatic Patterns on Surfactant Coatings Change with Ambient Humidity. *J. Phys. Chem. C* **114**, 19016–19023 (2010).
58. Liu, C. & Bard, A. J. Electrostatic electrochemistry at insulators. *Nat. Mater.* **7**, 505–509 (2008).
59. Liu, C. & Bard, A. J. Electrons on dielectrics and contact electrification. *Chem. Phys. Lett.* **480**, 145–156 (2009).
60. Liu, C. & Bard, A. J. Electrostatic electrochemistry: Nylon and polyethylene systems. *Chem. Phys. Lett.* **485**, 231–234 (2010).
61. Liu, C. & Bard, A. J. Chemical Redox Reactions Induced by Cryptoelectrons on a PMMA Surface. *J. Am. Chem. Soc.* **131**, 6397–6401 (2009).
62. Baytekin, H. T., Baytekin, B. & Grzybowski, B. A. Mechanoradicals Created in ‘Polymeric Sponges’ Drive Reactions in Aqueous Media. *Angew. Chem. Int. Ed.* **51**, 3596–3600 (2012).

63. Knorr, N. Squeezing out hydrated protons: low-frictional-energy triboelectric insulator charging on a microscopic scale. *AIP Adv.* **1**, 022119 (2011).
64. Burgo, T. A. L. *et al.* Triboelectricity: Macroscopic Charge Patterns Formed by Self-Arrayed Ions on Polymer Surfaces. *Langmuir* **28**, 7407–7416 (2012).
65. Wiley: Statistics for Experimenters: Design, Innovation, and Discovery, 2nd Edition - George E. P. Box, J. Stuart Hunter, William G. Hunter. Available at: <http://www.wiley.com/WileyCDA/WileyTitle/productCd-0471718130.html>. (Accessed: 26th June 2017)
66. Roy, R. K. *A primer on the Taguchi method.* (Van Nostrand Reinhold, 1990).
67. Franssila, S. *Introduction to microfabrication* /. (John Wiley & Sons, 2010).
68. Zhu, G. *et al.* Triboelectric-Generator-Driven Pulse Electrodeposition for Micropatterning. *Nano Lett.* **12**, 4960–4965 (2012).
69. Jang, S., Kim, H. & Oh, J. H. Simple and rapid fabrication of pencil-on-paper triboelectric nanogenerators with enhanced electrical performance. *Nanoscale* (2017). doi:10.1039/C7NR04610C
70. Zerweck, U., Loppacher, C., Otto, T., Grafström, S. & Eng, L. M. Accuracy and resolution limits of Kelvin probe force microscopy. *Phys. Rev. B* **71**, 125424 (2005).
71. Li, C. *et al.* PeakForce Kelvin Probe Force Microscopy. (2013).
72. Butt, H.-J., Cappella, B. & Kappl, M. Force measurements with the atomic force microscope: Technique, interpretation and applications. *Surf. Sci. Rep.* **59**, 1–152 (2005).
73. Jacobs, T. D. B., Mathew Mate, C., Turner, K. T. & Carpick, R. W. Understanding the Tip–Sample Contact. in *Scanning Probe Microscopy in Industrial Applications* (ed. Yablon, D. G.) 15–48 (John Wiley & Sons, Inc, 2013). doi:10.1002/9781118723111.ch2
74. PMMA. Available at: <http://www.mit.edu/~6.777/matprops/pmma.htm>. (Accessed: 27th June 2017)
75. Wiley: Mechanics of Materials, 3rd Edition - Roy R. Craig. Available at: <http://www.wiley.com/WileyCDA/WileyTitle/productCd-EHEP001802.html>. (Accessed: 27th June 2017)
76. Scovell, D. L., Pinkerton, T. D., Medvedev, V. K. & Stuve, E. M. Phase transitions in vapor-deposited water under the influence of high surface electric fields. *Surf. Sci.* **457**, 365–376 (2000).
77. Ewing, G. E. Ambient Thin Film Water on Insulator Surfaces. *Chem. Rev.* **106**, 1511–1526 (2006).
78. Butt, H.-J. & Kappl, M. Capillary Forces. in *Surface and Interfacial Forces* 127–161 (Wiley-VCH Verlag GmbH & Co. KGaA, 2010). doi:10.1002/9783527629411.ch5
79. Fan, Y., Chen, X., Yang, L., Cremer, P. S. & Gao, Y. Q. On the Structure of Water at the Aqueous/Air Interface. *J. Phys. Chem. B* **113**, 11672–11679 (2009).
80. Lee, S. H. & Rasaiah, J. C. Proton transfer and the diffusion of H⁺ and OH⁻ ions along water wires. *J. Chem. Phys.* **139**, 124507 (2013).
81. Shen, Y. R. & Ostroverkhov, V. Sum-Frequency Vibrational Spectroscopy on Water Interfaces: Polar Orientation of Water Molecules at Interfaces. *Chem. Rev.* **106**, 1140–1154 (2006).
82. Cipcigan, F. S., Sokhan, V. P., Jones, A. P., Crain, J. & Martyna, G. J. Hydrogen bonding and molecular orientation at the liquid–vapour interface of water. *Phys. Chem. Chem. Phys.* **17**, 8660–8669 (2015).

83. Artemov, V. G. & Volkov, A. A. Water and Ice Dielectric Spectra Scaling at 0°C. *Ferroelectrics* **466**, 158–165 (2014).
84. Hippel, A. R. von. The dielectric relaxation spectra of water, ice, and aqueous solutions, and their interpretation. III. Proton organization and proton transfer in ice. *IEEE Trans. Electr. Insul.* **23**, 825–840 (1988).
85. Németh, E., Albrecht, V., Schubert, G. & Simon, F. Polymer tribo-electric charging: dependence on thermodynamic surface properties and relative humidity. *J. Electrostat.* **58**, 3–16 (2003).
86. Butt, H.-J., Graf, K. & Kappl, M. Contact Angle Phenomena and Wetting. in *Physics and Chemistry of Interfaces* 118–144 (Wiley-VCH Verlag GmbH & Co. KGaA, 2003). doi:10.1002/3527602313.ch7
87. Pua, L. S., Sedev, R., Fornasiero, D., Ralston, J. & Blake, T. Influence of Surface Charge on Wetting Kinetics. *Langmuir* **26**, 17218–17224 (2010).
88. Baytekin, B., Baytekin, H. T. & Grzybowski, B. A. Mechanically Driven Activation of Polyaniline into Its Conductive Form. *Angew. Chem. Int. Ed.* **53**, 6946–6950 (2014).
89. Baytekin, H. T., Baytekin, B., Huda, S., Yavuz, Z. & Grzybowski, B. A. Mechanochemical Activation and Patterning of an Adhesive Surface toward Nanoparticle Deposition. *J. Am. Chem. Soc.* **137**, 1726–1729 (2015).
90. Santos, L. P., Ducati, T. R. D., Balestrin, L. B. S. & Galembeck, F. Water with Excess Electric Charge. *J. Phys. Chem. C* **115**, 11226–11232 (2011).
91. Jie, Y. *et al.* Self-Powered Triboelectric Nanosensor with Poly(tetrafluoroethylene) Nanoparticle Arrays for Dopamine Detection. *ACS Nano* **9**, 8376–8383 (2015).
92. Lin, Z.-H. *et al.* A Self-Powered Triboelectric Nanosensor for Mercury Ion Detection. *Angew. Chem. Int. Ed.* **52**, 5065–5069 (2013).
93. Santos, S. & Verdager, A. Imaging Water Thin Films in Ambient Conditions Using Atomic Force Microscopy. *Materials* **9**, 182 (2016).
94. Fukuma, T., Ueda, Y., Yoshioka, S. & Asakawa, H. Atomic-Scale Distribution of Water Molecules at the Mica-Water Interface Visualized by Three-Dimensional Scanning Force Microscopy. *Phys. Rev. Lett.* **104**, 016101 (2010).
95. Cardellach, M., Verdager, A. & Fraxedas, J. Defect-induced wetting on BaF₂(111) and CaF₂(111) at ambient conditions. *Surf. Sci.* **605**, 1929–1933 (2011).
96. Santos, S., Verdager, A., Souier, T., Thomson, N. H. & Chiesa, M. Measuring the true height of water films on surfaces. *Nanotechnology* **22**, 465705 (2011).
97. Xu, K., Cao, P. & Heath, J. R. Graphene Visualizes the First Water Adlayers on Mica at Ambient Conditions. *Science* **329**, 1188–1191 (2010).
98. Verdager, A., Sacha, G. M., Luna, M., Frank Ogletree, D. & Salmeron, M. Initial stages of water adsorption on NaCl (100) studied by scanning polarization force microscopy. *J. Chem. Phys.* **123**, 124703 (2005).
99. Verdager, A. *et al.* Water-mediated height artifacts in dynamic atomic force microscopy. *Phys. Chem. Chem. Phys.* **14**, 16080–16087 (2012).
100. Sahagún, E., García-Mochales, P., Sacha, G. M. & Sáenz, J. J. Energy Dissipation due to Capillary Interactions: Hydrophobicity Maps in Force Microscopy. *Phys. Rev. Lett.* **98**, 176106 (2007).
101. Barcons, V., Verdager, A., Font, J., Chiesa, M. & Santos, S. Nanoscale Capillary Interactions in Dynamic Atomic Force Microscopy. *J. Phys. Chem. C* **116**, 7757–7766 (2012).

102. Schmitz, I., Schreiner, M., Friedbacher, G. & Grasserbauer, M. Phase imaging as an extension to tapping mode AFM for the identification of material properties on humidity-sensitive surfaces. *Appl. Surf. Sci.* **115**, 190–198 (1997).
103. James, P. J. *et al.* Interpretation of Contrast in Tapping Mode AFM and Shear Force Microscopy. A Study of Nafion. *Langmuir* **17**, 349–360 (2001).
104. Brandsch, R., Bar, G. & Whangbo, M.-H. On the Factors Affecting the Contrast of Height and Phase Images in Tapping Mode Atomic Force Microscopy. *Langmuir* **13**, 6349–6353 (1997).
105. García, R. & Pérez, R. Dynamic atomic force microscopy methods. *Surf. Sci. Rep.* **47**, 197–301 (2002).
106. García, R., Magerle, R. & Perez, R. Nanoscale compositional mapping with gentle forces. *Nat. Mater.* **6**, 405–411 (2007).
107. Hu, J., Xiao, X.-D., Ogletree, D. F. & Salmeron, M. Imaging the Condensation and Evaporation of Molecularly Thin Films of Water with Nanometer Resolution. *Science* **268**, 267–269 (1995).
108. Salmeron, M., Xu, L., Hu, J. & Dai, Q. High-Resolution Imaging of Liquid Structures: Wetting and Capillary Phenomena at the Nanometer Scale. *MRS Bull.* **22**, 36–41 (1997).
109. Sommer, A. P. *et al.* Interfacial Water an Exceptional Biolubricant. *Cryst. Growth Des.* **9**, 3852–3854 (2009).
110. Hu, J., Xiao, X. & Salmeron, M. Scanning polarization force microscopy: A technique for imaging liquids and weakly adsorbed layers. *Appl. Phys. Lett.* **67**, 476–478 (1995).
111. Riedel, C. *et al.* Dielectric properties of thin insulating layers measured by Electrostatic Force Microscopy. *Eur. Phys. J. Appl. Phys.* **50**, 10501 (2010).
112. Gramse, G., Gomila, G. & Fumagalli, L. Quantifying the dielectric constant of thick insulators by electrostatic force microscopy: effects of the microscopic parts of the probe. *Nanotechnology* **23**, 205703 (2012).
113. Cadena, M. J., Sung, S. H., Boudouris, B. W., Reifenberger, R. & Raman, A. Nanoscale Mapping of Dielectric Properties of Nanomaterials from Kilohertz to Megahertz Using Ultrasmall Cantilevers. *ACS Nano* **10**, 4062–4071 (2016).
114. Cherniavskaya, O., Chen, L., Weng, V., Yuditsky, L. & Brus, L. E. Quantitative Noncontact Electrostatic Force Imaging of Nanocrystal Polarizability. *J. Phys. Chem. B* **107**, 1525–1531 (2003).
115. Qi, G. *et al.* Quantifying Surface Charge Density by Using an Electric Force Microscope with a Referential Structure. *J. Phys. Chem. C* **113**, 204–207 (2009).
116. Teschke, O., Ceotto, G. & de Souza, E. F. Interfacial water dielectric-permittivity-profile measurements using atomic force microscopy. *Phys. Rev. E* **64**, 011605 (2001).
117. Kiracofe, D. *et al.* VEDA: Virtual Environment for Dynamic AFM. (2014). doi:D32R3NX9S
118. Glatzel, T., Lux-Steiner, M. C., Strassburg, E., Boag, A. & Rosenwaks, Y. Principles of Kelvin Probe Force Microscopy. in *Scanning Probe Microscopy* 113–131 (Springer, New York, NY, 2007). doi:10.1007/978-0-387-28668-6_5
119. Payam, A. F., Martin-Jimenez, D. & Garcia, R. Force reconstruction from tapping mode force microscopy experiments. *Nanotechnology* **26**, 185706 (2015).
120. Hölscher, H. Theory of phase-modulation atomic force microscopy with constant-oscillation amplitude. *J. Appl. Phys.* **103**, 064317 (2008).

121. Hu, S. & Raman, A. Inverting amplitude and phase to reconstruct tip–sample interaction forces in tapping mode atomic force microscopy. *Nanotechnology* **19**, 375704 (2008).
122. Hu, S. & Raman, A. Analytical formulas and scaling laws for peak interaction forces in dynamic atomic force microscopy. *Appl. Phys. Lett.* **91**, 123106 (2007).
123. Cleveland, J. P., Anczykowski, B., Schmid, A. E. & Elings, V. B. Energy dissipation in tapping-mode atomic force microscopy. *Appl. Phys. Lett.* **72**, 2613–2615 (1998).
124. Santos, S., Gadelrab, K. R., Souier, T., Stefancich, M. & Chiesa, M. Quantifying dissipative contributions in nanoscale interactions. *Nanoscale* **4**, 792–800 (2012).
125. Tamayo, J. & García, R. Effects of elastic and inelastic interactions on phase contrast images in tapping-mode scanning force microscopy. *Appl. Phys. Lett.* **71**, 2394–2396 (1997).
126. García, R., Tamayo, J. & Paulo, A. S. Phase contrast and surface energy hysteresis in tapping mode scanning force microscopy. *Surf. Interface Anal.* **27**, 312–316 (1999).
127. Martínez, N. F. & García, R. Measuring phase shifts and energy dissipation with amplitude modulation atomic force microscopy. *Nanotechnology* **17**, S167 (2006).
128. Bar, G., Brandsch, R. & Whangbo, M.-H. Effect of Viscoelastic Properties of Polymers on the Phase Shift in Tapping Mode Atomic Force Microscopy. *Langmuir* **14**, 7343–7347 (1998).
129. Szoszkiewicz, R. & Riedo, E. Nucleation Time of Nanoscale Water Bridges. *Phys. Rev. Lett.* **95**, 135502 (2005).
130. Restagno, F., Bocquet, L. & Biben, T. Metastability and Nucleation in Capillary Condensation. *Phys. Rev. Lett.* **84**, 2433–2436 (2000).
131. Santos, S., Barcons, V., Font, J. & Thomson, N. H. Bi-stability of amplitude modulation AFM in air: deterministic and stochastic outcomes for imaging biomolecular systems. *Nanotechnology* **21**, 225710 (2010).
132. Ziegler, D. Techniques to quantify local electric potentials and eliminate electrostatic artifacts in atomic force microscopy. (2009).
133. García, R. & San Paulo, A. Dynamics of a vibrating tip near or in intermittent contact with a surface. *Phys. Rev. B* **61**, R13381–R13384 (2000).
134. Yablon, D. G. & Haugstad, G. Phase Imaging. in *Scanning Probe Microscopy in Industrial Applications* (ed. Yablon, D. G.) 95–114 (John Wiley & Sons, Inc, 2013). doi:10.1002/9781118723111.ch4
135. García, R. & San Paulo, A. Attractive and repulsive tip-sample interaction regimes in tapping-mode atomic force microscopy. *Phys. Rev. B* **60**, 4961–4967 (1999).
136. Marth, M., Maier, D., Honerkamp, J., Brandsch, R. & Bar, G. A unifying view on some experimental effects in tapping-mode atomic force microscopy. *J. Appl. Phys.* **85**, 7030–7036 (1999).
137. Payton, O., Champneys, A. R., Homer, M. E., Picco, L. & Miles, M. J. Feedback-induced instability in tapping mode atomic force microscopy: theory and experiment. *Proc. R. Soc. Lond. Math. Phys. Eng. Sci.* rspa20100451 (2010). doi:10.1098/rspa.2010.0451
138. Sulchek, T., Yaralioglu, G. G., Quate, C. F. & Minne, S. C. Characterization and optimization of scan speed for tapping-mode atomic force microscopy. *Rev. Sci. Instrum.* **73**, 2928–2936 (2002).
139. D’Amato, M. J., Marcus, M. S., Eriksson, M. A. & Carpick, R. W. Phase imaging and the lever-sample tilt angle in dynamic atomic force microscopy. *Appl. Phys. Lett.* **85**, 4738–4740 (2004).

140. Erbil, H. Y., McHale, G., Rowan, S. M. & Newton, M. I. Determination of the Receding Contact Angle of Sessile Drops on Polymer Surfaces by Evaporation. *Langmuir* **15**, 7378–7385 (1999).
141. Zi, Y. & Wang, Z. L. Nanogenerators: An emerging technology towards nanoenergy. *APL Mater.* **5**, 074103 (2017).
142. Niu, S. & Wang, Z. L. Theoretical systems of triboelectric nanogenerators. *Nano Energy* **14**, 161–192 (2015).
143. Fan, F.-R., Tian, Z.-Q. & Lin Wang, Z. Flexible triboelectric generator. *Nano Energy* **1**, 328–334 (2012).
144. Niu, S. *et al.* Simulation method for optimizing the performance of an integrated triboelectric nanogenerator energy harvesting system. *Nano Energy* **8**, 150–156 (2014).
145. Niu, S. *et al.* Theoretical study of contact-mode triboelectric nanogenerators as an effective power source. *Energy Environ. Sci.* **6**, 3576–3583 (2013).
146. Niu, S. *et al.* Theory of Sliding-Mode Triboelectric Nanogenerators. *Adv. Mater.* **25**, 6184–6193 (2013).
147. Niu, S. *et al.* Theoretical Investigation and Structural Optimization of Single-Electrode Triboelectric Nanogenerators. *Adv. Funct. Mater.* **24**, 3332–3340 (2014).
148. Niu, S. *et al.* Theory of freestanding triboelectric-layer-based nanogenerators. *Nano Energy* **12**, 760–774 (2015).
149. Yang, B. *et al.* A Fully Verified Theoretical Analysis of Contact-Mode Triboelectric Nanogenerators as a Wearable Power Source. *Adv. Energy Mater.* **6**, n/a-n/a (2016).
150. Niu, S. *et al.* Optimization of Triboelectric Nanogenerator Charging Systems for Efficient Energy Harvesting and Storage. *IEEE Trans. Electron Devices* **62**, 641–647 (2015).
151. Zi, Y. *et al.* Effective energy storage from a triboelectric nanogenerator. *Nat. Commun.* **7**, ncomms10987 (2016).
152. Hayt, W. H. *Engineering circuit analysis*. (McGraw-Hill, 2012).
153. Griffiths, D. J. *Introduction to electrodynamics*.
154. Zi, Y. *et al.* Standards and figure-of-merits for quantifying the performance of triboelectric nanogenerators. *Nat. Commun.* **6**, 8376 (2015).
155. DUPONT™ KAPTON®:SUMMARY OF PROPERTIES.
156. Lin, Z.-H., Cheng, G., Wu, W., Pradel, K. C. & Wang, Z. L. Dual-Mode Triboelectric Nanogenerator for Harvesting Water Energy and as a Self-Powered Ethanol Nanosensor. *ACS Nano* **8**, 6440–6448 (2014).
157. Zhang, H. *et al.* Triboelectric nanogenerator as self-powered active sensors for detecting liquid/gaseous water/ethanol. *Nano Energy* **2**, 693–701 (2013).
158. Sakaguchi, M., Shimada, S. & Kashiwabara, H. Mechanoions produced by mechanical fracture of solid polymer. 6. A generation mechanism of triboelectricity due to the reaction of mechanoradicals with mechanoanions on the friction surface. *Macromolecules* **23**, 5038–5040 (1990).
159. Sakaguchi, M. & Kashiwabara, H. A generation mechanism of triboelectricity due to the reaction of mechanoradicals with mechanoions which are produced by mechanical fracture of solid polymer. *Colloid Polym. Sci.* **270**, 621–626 (1992).
160. Sakaguchi, M., Makino, M., Ohura, T. & Iwata, T. Mechanoanions Produced by Mechanical Fracture of Bacterial Cellulose: Ionic Nature of Glycosidic Linkage and Electrostatic Charging. *J. Phys. Chem. A* **116**, 9872–9877 (2012).
161. Sohma, J. Mechanochemistry of polymers. *Prog. Polym. Sci.* **14**, 451–596 (1989).

162. Sweeting, L. M. Triboluminescence with and without Air. *Chem. Mater.* **13**, 854–870 (2001).
163. Han, C. B. *et al.* Triboelectrification induced UV emission from plasmon discharge. *Nano Res.* **8**, 219–226 (2015).
164. Perkins, M. J. *Radical Chemistry: The Fundamentals*. (Oxford University Press, 2000).
165. Mazur, T. & A. Grzybowski, B. Theoretical basis for the stabilization of charges by radicals on electrified polymers. *Chem. Sci.* **8**, 2025–2032 (2017).
166. Oyaizu, K. & Nishide, H. Radical Polymers for Organic Electronic Devices: A Radical Departure from Conjugated Polymers? *Adv. Mater.* **21**, 2339–2344 (2009).
167. Janoschka, T., Hager, M. D. & Schubert, U. S. Powering up the Future: Radical Polymers for Battery Applications. *Adv. Mater.* **24**, 6397–6409 (2012).
168. Nakahara, K., Oyaizu, K. & Nishide, H. Organic Radical Battery Approaching Practical Use. *Chem. Lett.* **40**, 222–227 (2011).
169. Nakahara, K. *et al.* Rechargeable batteries with organic radical cathodes. *Chem. Phys. Lett.* **359**, 351–354 (2002).
170. Nakahara, K. *et al.* Cell properties for modified PTMA cathodes of organic radical batteries. *J. Power Sources* **165**, 398–402 (2007).
171. Song, G. *et al.* Molecularly Engineered Surface Triboelectric Nanogenerator by Self-Assembled Monolayers (METS). *Chem. Mater.* **27**, 4749–4755 (2015).
172. Michinobu, T., Inui, J. & Nishide, H. Magnetic Force Microscopic Images of Nanometer-Sized Polyradical Particles. *Polym. J.* **35**, 71–75 (2003).
173. Nishide, H., Ozawa, T., Miyasaka, M. & Tsuchida, E. A Nanometer-Sized High-Spin Polyradical: Poly(4-phenoxy-1,2-phenylenevinylene) Planarily Extended in a Non-Kekulé Fashion and Its Magnetic Force Microscopic Images. *J. Am. Chem. Soc.* **123**, 5942–5946 (2001).
174. Miyasaka, M., Saito, Y. & Nishide, H. Magnetic Force Microscopy Images of a Nanometer-Sized, Purely Organic High-Spin Polyradical. *Adv. Funct. Mater.* **13**, 113–117 (2003).
175. Hartmann, U. Magnetic Force Microscopy. *Annu. Rev. Mater. Sci.* **29**, 53–87 (1999).
176. Angeloni, L., Passeri, D., Reggente, M., Mantovani, D. & Rossi, M. Removal of electrostatic artifacts in magnetic force microscopy by controlled magnetization of the tip: application to superparamagnetic nanoparticles. *Sci. Rep.* **6**, srep26293 (2016).
177. Tanaka, M., Saito, Y. & Nishide, H. Magnetic Force Microscopy as a New Tool to Evaluate Local Magnetization of Organic Radical Polymers. *Chem. Lett.* **35**, 1414–1415 (2006).
178. Guo, W., Yin, Y.-X., Xin, S., Guo, Y.-G. & Wan, L.-J. Superior radical polymer cathode material with a two-electron process redox reaction promoted by graphene. *Energy Environ. Sci.* **5**, 5221–5225 (2012).
179. Rintoul, L., Micallef, A. S. & Bottle, S. E. The vibrational group frequency of the N–O stretching band of nitroxide stable free radicals. *Spectrochim. Acta. A. Mol. Biomol. Spectrosc.* **70**, 713–717 (2008).
180. Nishide, H. *et al.* Organic radical battery: nitroxide polymers as a cathode-active material. *Electrochimica Acta* **50**, 827–831 (2004).
181. Zhu, G. *et al.* Self-Powered, Ultrasensitive, Flexible Tactile Sensors Based on Contact Electrification. *Nano Lett.* **14**, 3208–3213 (2014).

182. Koshika, K., Sano, N., Oyaizu, K. & Nishide, H. An Aqueous, Electrolyte-Type, Rechargeable Device Utilizing a Hydrophilic Radical Polymer-Cathode. *Macromol. Chem. Phys.* **210**, 1989–1995 (2009).
183. Rostro, L., Wong, S. H. & Boudouris, B. W. Solid State Electrical Conductivity of Radical Polymers as a Function of Pendant Group Oxidation State. *Macromolecules* **47**, 3713–3719 (2014).
184. Watts, J. F. & Wolstenholme, J. Electron Spectroscopy: Some Basic Concepts. in *An Introduction to Surface Analysis by XPS and AES* 1–15 (John Wiley & Sons, Ltd, 2003). doi:10.1002/0470867930.ch1
185. Bertrand, O., Vlad, A., Hoogenboom, R. & Gohy, J.-F. Redox-controlled upper critical solution temperature behaviour of a nitroxide containing polymer in alcohol–water mixtures. *Polym. Chem.* **7**, 1088–1095 (2016).
186. Fan, F.-R. *et al.* Transparent Triboelectric Nanogenerators and Self-Powered Pressure Sensors Based on Micropatterned Plastic Films. *Nano Lett.* **12**, 3109–3114 (2012).
187. Dardenne, N., Blase, X., Hautier, G., Charlier, J.-C. & Rignanese, G.-M. Ab Initio Calculations of Open-Cell Voltage in Li-Ion Organic Radical Batteries. *J. Phys. Chem. C* **119**, 23373–23378 (2015).
188. Yilmaz, E., Sezen, H. & Suzer, S. Probing the Charge Build-Up and Dissipation on Thin PMMA Film Surfaces at the Molecular Level by XPS. *Angew. Chem. Int. Ed.* **51**, 5488–5492 (2012).

Appendix A

Ambient Vibration Measurement

Four different ambient vibrational sources were examined. The vibration measurement was taken from BMA-220 accelerometer, which can provide acceleration measurement for all 3 axes. BMA-220 was interfaced with Arduino Nano. The accelerometer sensitivity was set at 2g and the bandwidth of 500 Hz. The time-varying acceleration readings were collected from Arduino Nano and Python Interface. FFT of the collected readings was performed in Python for each individual axis.

Measurement from the tree

The accelerometer was tied to one of the branches of the tree. Due to the attached mass of the accelerometer and the wire with the branch, a slight decrease in amplitude of vibration was observed compared to the other branches. While the readings were collected, the mild air was flowing.

Measurement from the human walk

The measurement from the human walk was taken by placing the accelerometer on the side of the ankle.

Measurement from the car

The accelerometer was placed in front of the windshield. The speed of the car reached a maximum of 40 km/hr.

Measurement from the bridge

The accelerometer was placed on the top of sidewalk railing.

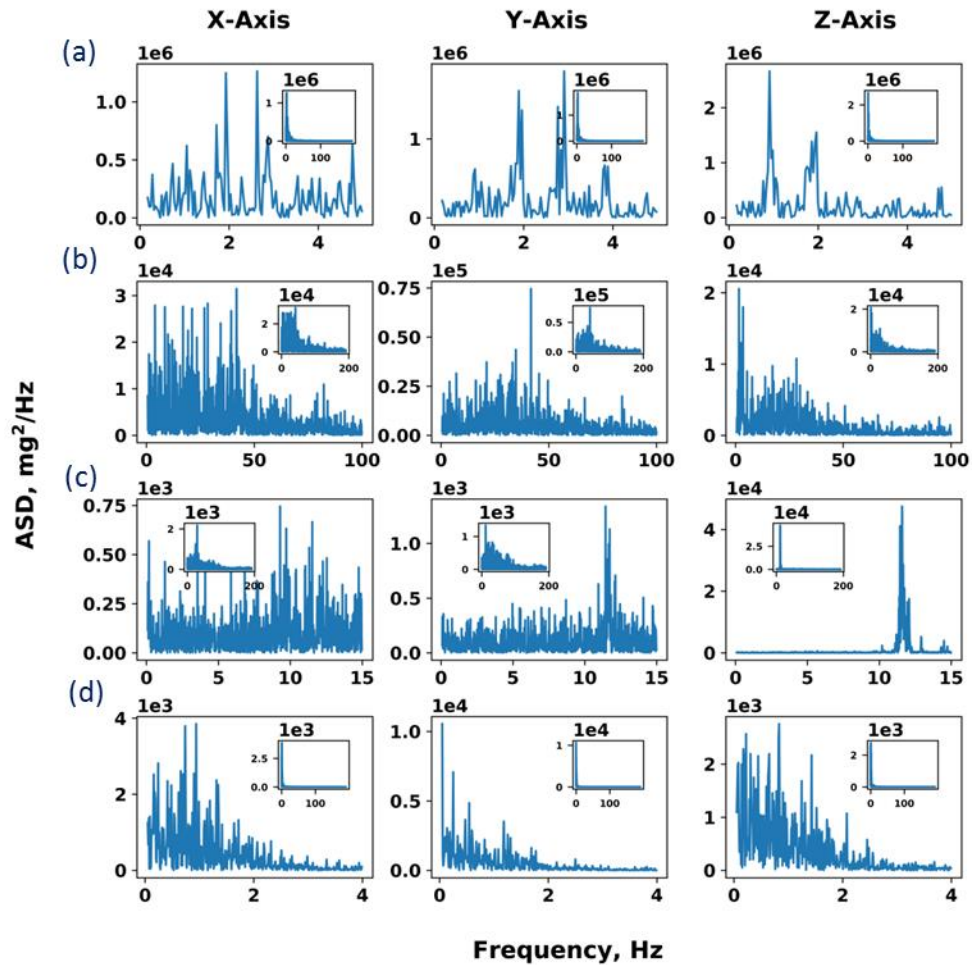


Fig. A1: Acceleration spectral density (ASD) of (a) human walk, (b) a moving car, (c) bridge and (d) a tree. The ASD for all three different axes is shown and labeled at the top of the figure. Also, only the significant portion where the acceleration is significant has been shown. The complete acceleration spectra are shown in the inset in each figure. It can easily be seen that most of the acceleration is at low frequency.

Appendix B



Fig. B1: Electrical connection between tip and the fluid AFM head by soldering a wire for KPFM analysis

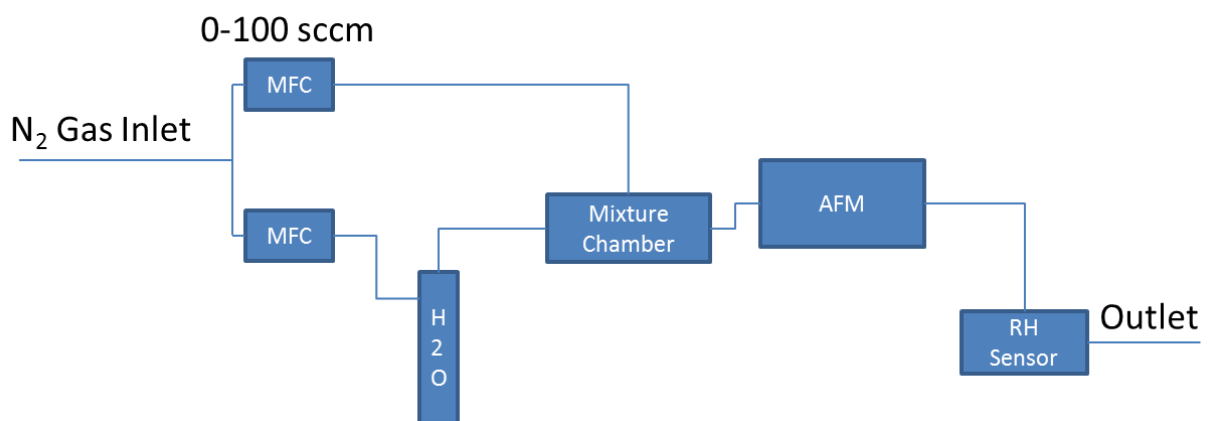


Fig. B2: Schematic of the setup for controlling RH in the AFM.

Appendix C

TENG Setup

An in-house stepper motor based linear actuator was developed as shown in Fig. C1 below. Stepper motor was controlled through a driver (ULN 2003 microprocessor chip) which was controlled by Arduino. The distance traveled and the speed is controlled by assigning no. of steps and the time required for taking each step. For the current stepper motor, the minimum step time was identified to be around 10 ms. Until or unless specified, the step time was kept constant at 10ms. To control the distance travel, lead screw with a pitch of 4 mm was used which gives a linear motion of 40 $\mu\text{m}/\text{step}$. Therefore, if 100 steps are given to stepper motor while TENG operation, instead of 4 mm total travel, ~ 2.5 mm of travel distance was observed. The apparent discrepancy between the actual travel distance and theoretical travel distance is due to the coupler which shrinks when some amount of force is applied to it. Therefore, the travel velocity is also not constant during TENG device operation. The measured distance was taken from a 1 cm variable linear resistor. The variable linear resistor was attached to the TENG setup. The voltage from the resistor was fed to the Op-amp circuit which amplified the signal and consequently, a resolution of 10 μm from the variable resistor was achieved and sent to Arduino microprocessor. TENG devices were placed between two 5 mm acrylic sheet which was separated by four springs with a spring constant of 300 N/m. To measure the applied force, a weighing balance was kept below the TENG device which had a resolution of 0.1 g. Through the experiments conducted it was observed that the stepper motor can apply a maximum load of 2.5 kgf consistently. Any force higher than this results in the drift in stepper motor motion. Until or unless specified, a force of 2.5 kgf (24.5 N) was applied during all the experiments. The weight of the acrylic sheet and the spring was found to be around 0.220 kgf (2.15 N). Since 4 springs were used to separate the two plates, they are in parallel. Therefore, the total force taken by the spring with 2.4 mm travel distance is $4 \times 300 \times 2.4 / 1000 \text{ N} = 2.9 \text{ N}$. Hence, the total applied force on TENG devices, during the operation is $24.5 - 2.15 - 2.9 \approx 19.5 \text{ N}$.

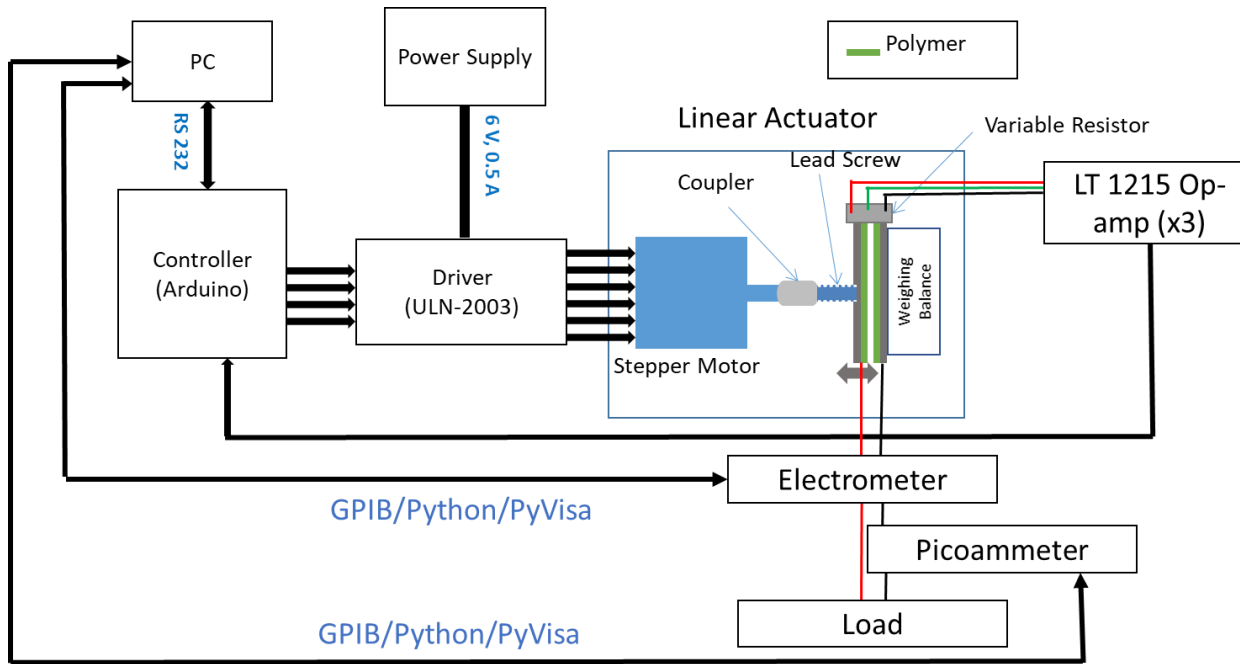


Fig. C1: Schematic of In-house developed TENG setup together with the measurement setup.

Displacement Measurement

The sampling rate of Arduino is 10 kHz maximum. Since a variable resistor has been used for the measurement of displacement at such a high sampling rate the impedance property of variable resistor might change. Hence, the frequency dependent resistance measurement was conducted and is shown in Fig. C3a. It was noticed that the electrical property of variable resistor does not change significantly up to 10 kHz shown as a vertical line in the plot.

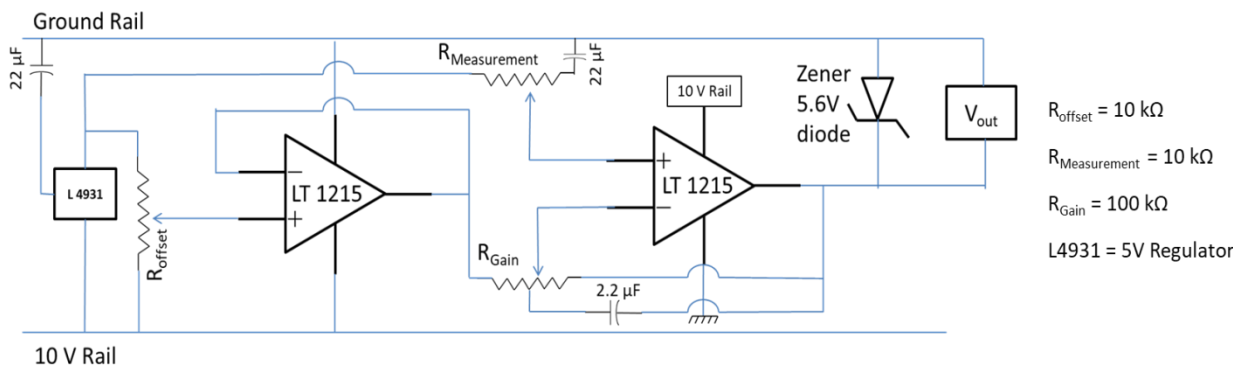


Fig. C2: Amplifier circuit for measuring displacement during TENG operation.

An amplifier circuit was used to increase the resolution of the variable resistor. The Op-Amp used in this study was LT 1215. The maximum voltage which can be supplied to Arduino is 5V and it does not measure negative voltages. However, in the current circuit to drive the amplifier 10 V source was required. Hence, a 5V regulator (L4931) was used to regulate the voltage across the variable resistor. R_{offset} and R_{Gain} were the potentiometers whereas $R_{\text{measurement}}$ was a linear variable resistor whose travel distance was 10 mm. The capacitors were used in the circuit to eliminate high-frequency noise. Since a variable resistor was used to measure the displacement, there was V_{offset} present when $x=0$. Due to the presence of V_{offset} , the measurement bandwidth decreased. Hence, R_{offset} was used which was adjusted in such a way that V_{offset} can be nullified. However, V_{offset} was never allowed go to 0 V as negative voltages could not be measured from Arduino. The voltage from R_{offset} was fed through unity gain Op-amp. The voltage sent to the negative terminal of another LT1215. The positive terminal was connected to the $R_{\text{measurement}}$. On the output side, to control the voltage a Zener diode as a voltage regulator was used as shown in Fig. C2. The V_{out} was sent to the Arduino and from ADC converter measurements were taken. Without the use of amplifier displacement resolution was found to be 30 μm . However, with an amplifier, the displacement resolution increased to 10 μm . The output of $R_{\text{measurement}}$ and Amplifier were compared to determine the gain from Amplifier circuit. The results are shown in Fig. C3b. It can be noticed that the actual values occur at some specific points. This is due to the poor resolution of ADC converter and the electrical noise associated with the wiring. A gain of 3 was measured from these reading as shown in Fig. C3b.

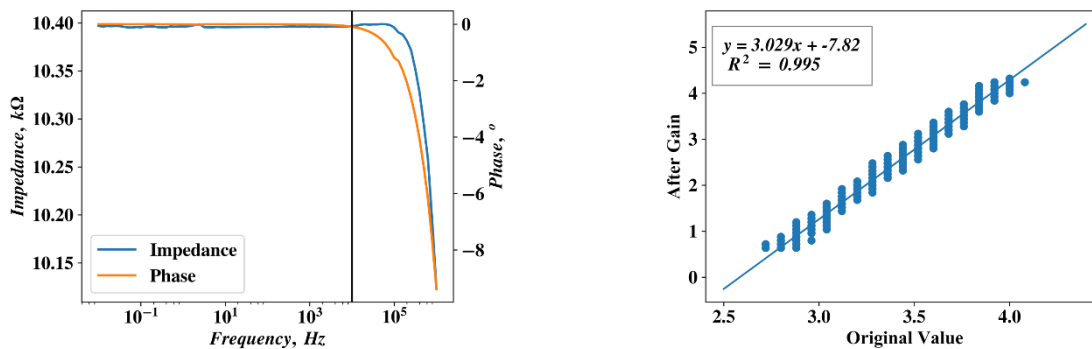


Fig. C3: (a) Frequency-dependent response of $R_{\text{measurement}}$. The vertical line shows the maximum sampling frequency from Arduino. (b) The Op-Amp output compared with the input which gives a gain of 3.

Electrical noise and TENG measurement

Since TENG devices are capacitive in nature, there is a possibility of parasitic capacitance coupling between TENG device and its surrounding. In the lab environment, one of the important parasitic capacitance coupling could arise from the electrical lines. This coupling will result in noise during measurements. For current and voltage measurement, the coupling could affect the results in completely different manner. It was observed that only current is significantly influenced by the electrical noise. Initially, while setting up the TENG and characterizing the performance across different resistors, it was observed that as the resistor value increased from 200 Ω to 400 M Ω , the current remains nearly constant, whereas the voltage kept on increasing. Although it is well known that as resistance increases current should drop. Upon closer inspection, it was noticed that some external noise was super-positioned with the actual signal as shown in Fig. C4a. Therefore, Fast Fourier Transformation (FFT) was performed on the current and the voltage reading. During measurement, it was noticed that each cycle completes nearly in 0.3 seconds. Hence, the frequency of oscillation should be 3.3 Hz (Fig. C4c). The FFT of current and voltage reading gave the same frequency together with the higher harmonics. Higher harmonics arise due to a constant velocity of the stepper motor. Interestingly, it was observed that apart from the 3.3 Hz frequency and higher harmonics, there is a significant contribution coming from a peak around 21 Hz. This frequency was a rather unique as there were no components which had a frequency around 21 Hz. A further look at the result suggested that the data were captured at the rate of around 81.6 S/s, which gives the observable frequency from Nyquist criteria to be around 40.8 Hz. The electrical lines have a frequency of 60 Hz. Hence aliasing frequency of around 21.6 Hz was expected as shown in Fig. C4c with a diamond marker. The aliasing effect was calculated as

$$f_a = |R \cdot n - f_s| \quad \text{Eq. 1}$$

Where, f_a is the aliased frequency, R is the sampling frequency, n is the closest integer multiple of R compared to f_a and f_s is the sampling frequency (= 60Hz).

The observed anomalous frequency in the current measurement was found to be around similar values. Hence electrical noise was the region for the observed anomalous frequency. Therefore, it was necessary to eliminate these noise sources as they will inadvertently affect the TENG

performance. Several ways were tried to eliminate the noise, such as placing the TENG setup in Faraday cup, making a common ground connection to avoid ground loops etc. One of the major sources of electrical noise was stepper motor itself. To decrease the electrical noise, the length of the lead screw was increased and grounding of stepper motor was changed from chassis to earth ground. This resulted in a slightly lower electrical noise but the problem still persisted. However, the electrical noise decreased significantly when the measurements were performed at a lower sampling rate (~ 39 S/s i.e., NPLC = 1). The current measurement acquired with low sampling rate is shown in Fig. C4b. It can be clearly seen that electrical noise was not noticeable in these measurements. The distortion in the shape of current measurement is due to the slanted movement of the upper electrode. Further to ensure that there should be no contributions from 60 Hz frequency on the current data, FFT of all the results were performed and attention was paid to the possible aliasing effect. f_a for this set of experiments were calculated to be at 18.3 Hz. In Fig. C4d, no electrical line frequency aliasing was observed. The inset shows the magnified result around the same area. A small peak can be noticed during the measurement which could arise due to the higher harmonics of the primary peak as seen by the small peak around 18.9 and 19.2 Hz. Even if the peak at 18.35 Hz was due to electrical noise, it was noticed that its magnitude has decreased by 5 times. Hence, effect of electrical line frequency was significantly reduced. Similar observations were made for all the other current measurements.

Instrument Triggering and Measurement:

Although in the present study pico-ammeter was not used, but for characterizing TENG device with a resistive or capacitive load, it was used. It was noticed that data acquisition rate of electrometer, pico-ammeter, and Arduino was completely different. Therefore, electrometer and pico-ammeter a trigger signal was sent from Python program. For displacement reading from Arduino, a communication lag was noticed between the trigger signal and data received. This could be due to Serial communication between Arduino and PC, whereas electrometer and pico-ammeter had Visa communication. Therefore, displacement readings were continuously collected. However, the coding was done in such a way that only one displacement reading was saved after each reading from electrometer and pico-ammeter. However, there were still some lags between each reading. Therefore for each measurement, the results were interpolated for the fixed time interval.

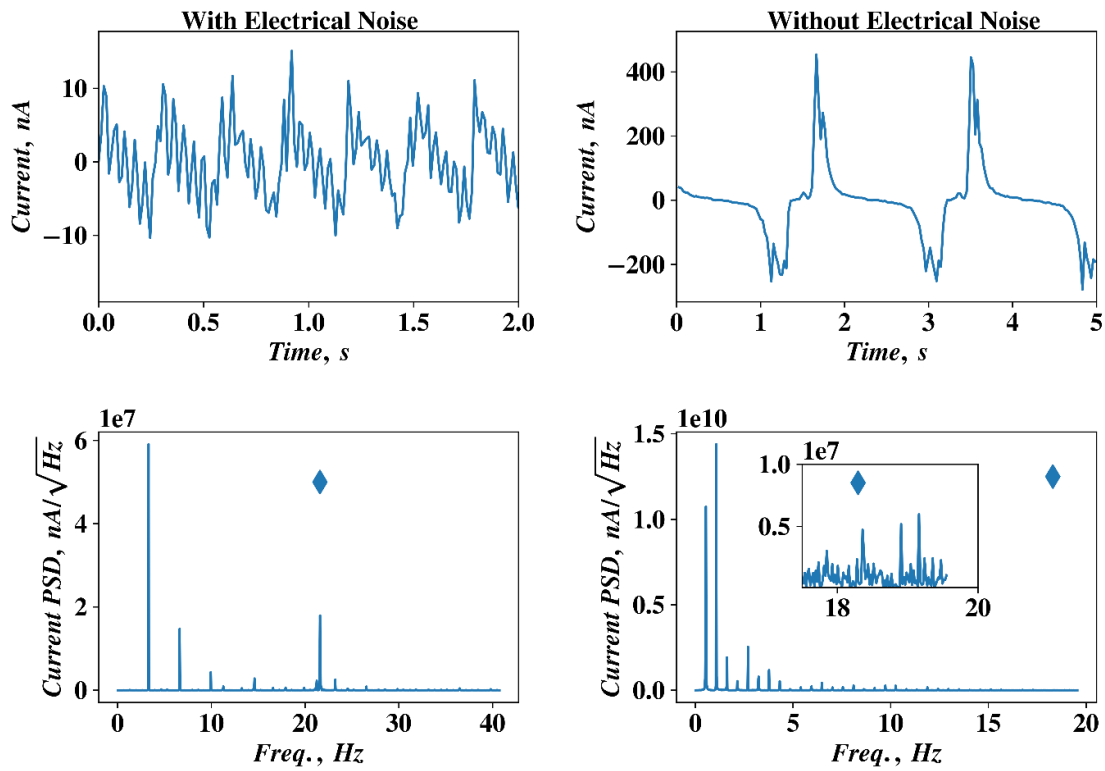


Fig. C4: Short circuit current measurement with (a) electrical noise, (b) without electrical noise. FFT spectra of current measurement taken with (c) electrical noise and (d) without electrical noise. The diamond marker in (c) and (d) indicate the location where electrical noise can arise due to aliasing effect. The inset in (d) shows the magnified region where the electrical noise was expected.